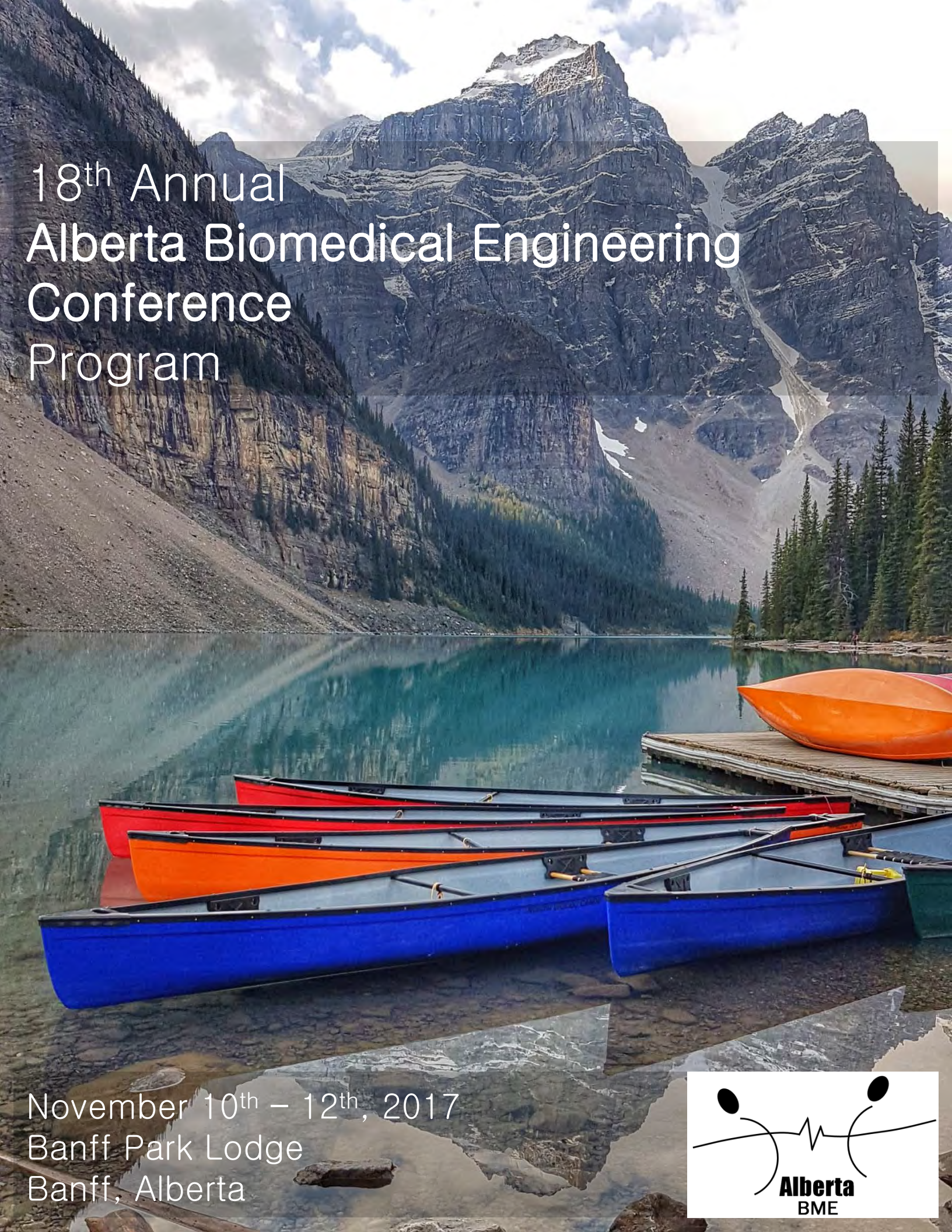

18th Annual Alberta Biomedical Engineering Conference Program

November 10th – 12th, 2017
Banff Park Lodge
Banff, Alberta

Alberta BME

We gratefully acknowledge the support of our sponsors for making this conference a success

UNIVERSITY OF CALGARY
Biomedical Engineering Graduate Program

McCaig Institute
for Bone and Joint Health

Centre for Bioengineering
Research and Education

Schulich Student Activities Fund

The Microsystems Hub

18th Annual Alberta Biomedical Engineering Conference
Banff 2017

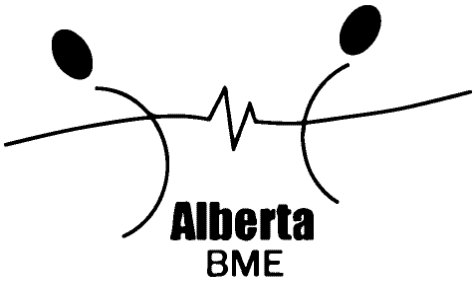

November 10-12, 2017
Banff Park Lodge
Banff, AB

PROGRAM COMMITTEE

CONFERENCE ORGANIZERS

Co-Chairs	University of Calgary	Roman Krawetz Michael S. Kallos
	University of Saskatchewan	James Johnston
	University of Alberta	Hussein Rouhani, Colin Firminger
Student Co-Chairs	University of Calgary	Reza Basiri Sahand Talai

ABSTRACT REVIEWERS

University of Calgary
Elena Di Martino
Steven Boyd
Neil Duncan
David A. Hart
Roman Krawetz
John Matyas
Nigel Shrive
Brent Edwards
Mike Kallos

University of Alberta
Christopher Dennison
Dan Romanyk
Andrew Martin
Larry Unsworth
Albert Vette
Lindsey Westover
Hussein Rouhani
Roman Krawetz

University of Saskatchewan
James Johnston
Emily McWalter
Steve Machtaler

AHS
Doug Hill

POSTER JUDGES

University of Calgary	Sarah Manske Elena Di Martino John Bertram Roman Krawetz	Mark Ungrin Ian Lewis Mike Kallos
University of Saskatchewan	James Johnston	Emily McWalter

PODIUM JUDGES

Dr. Joseph Cafazzo, University Health Network (UHN)
Dr. Gordon E. Sarty, University of Saskatchewan

TRAINEE VOLUNTEERS

University of Calgary Student Volunteers	Colin Firminger Sahand Talai Reza Basiri		Student Co-Chair, student organizer, undergraduate funding, AV organization, volunteer recruitment, registration package assembly, sponsorship
Geoff Michalak Samaneh Sattari Sahand Talai	Anand Masson Julie Aitken Colin Firminger	Reza Basiri Kathryn Ronayne	Package assembly / Registration Pkgs
Jane Maynard Tiffany Dang	Alina Ismaguilova Ibukun Oni	Andres Kroker Anand Masson	Registration – Banff Park Lodge
Danielle Whittier Najratun Pinky Geoff Michalak Sultan Khetani	Scott Sibole Jolene Phelps Alex Wyma Eng Kuan Moo	Lindsay Loundagin Amin Komeili Andres Kroker	Session Chairs - Presentations
Andres Kroker			Photographer

CONFERENCE EVENT COORDINATOR

University of Calgary Elizabeth Mullaney

A BIG THANK YOU TO ALL OF OUR VOLUNTEERS WHO HELPED WITH THE ORGANIZATION AND PLANNING OF OUR CONFERENCE THIS YEAR!

A SPECIAL THANK YOU TO LISA MAYER FOR HER ONGOING SUPPORT OF OUR ANNUAL ALBERTA BME CONFERENCE

PROGRAM

Podium sessions are in the Summit Assiniboine room.
Poster sessions are in the Castle and Alpine Meadows rooms.
You must wear your name badge in order to access all meals and conference events (podium, poster sessions, coffee breaks).

FRIDAY

4:30 - 8:30 pm	**REGISTRATION and CHECK-IN** **Banff Park Lodge Lobby**
7:30 pm	**<u>Opening Reception</u> – Dr. Kallos/Dr. Krawetz** Location: Glacier Salon **3 Minutes Thesis Competition**

SATURDAY

7:00 – 8:00 am			**BREAKFAST – Glacier Chinook**
8:00 – 8:05 am			**Welcoming Remarks – Dr. Kallos/Dr. Krawetz** Location: Summit Assiniboine
8:05 – 8:45 am			**<u>Guest Speaker #1</u>:** Dr. Joseph Cafazzo, University Health Network (UHN) **Session chairs:** Danielle Whittier, Najratun Pinky
8:45 – 9:55 am			**<u>Student Podium Presentation Session #1</u>** **Session Chairs**: Sultan Khetani, Amin Komeili
	Dena Burnett	01	More numerous subchondral cysts are associated with higher lateral tibial subchondral bone mineral density in patients with knee osteoarthritis
	Lindsay Loundagin	02	MECHANICAL FATIGUE OF CORTICAL BONE IN TENSION AND COMPRESSION: EFFECTS OF MICROARCHITECTURE
	Justin Park	03	Automatic Bolus Arrival Time (BAT) Detection for Dynamic Contrast-Enhanced (DCE) Imaging with Under-sampling of k-Space
	Yang Yu	04	Re-engineering Islets for Improved Performance and Graft Function

Luis Souto Maior	05	Magnetic Resonance Image Sequence Classification using Convolutional Neural Networks
Nedaa Aljezani	06	In vitro cell surface markers are insufficient to identify in vivo/in situ multipotent synovial mesenchymal stem cells isolated from normal or osteoarthritic knees

9:55-10:00 **REMEMBRANCE DAY OBSERVATION**

9:55 - 11:10 am

Poster Session #1 (ODD NUMBERED POSTERS)

Sponsored by SSE The Microsystems Hub

Judges: University of Calgary: Drs. Sarah Manske, Elena Di Martino, John Bertram, Mark Ungrin, Ian Lewis, Mike Kallos, Roman Krawetz

University of Saskatchewan: Drs. Emily McWalter, James Johnston

COFFEE/BEVERAGE BREAK - Castle and Alpine Meadows

Christopher Urbinsky	01	The Translamellar Cross Bridge Structures of the Intervertebral Disc
Harsupreet Sidhu	03	Geometric and Strain-Based Analysis of Abdominal Aortic Aneurysms Undergoing Open Repair vs Endovascular Repair
Milad Nazarahari	05	A robust daily activity analysis methodology using a single tri-axial accelerometer mounted on the chest
Jacob George	07	Using HR-pQCT and finite element analysis at the tibia to differentiate vertebral fracture patients from healthy controls
Branden Shin	09	Shear Stress and Nanoparticle Distribution in Zebrafish Blood Vessels
Meredith Stadnyk	11	Quantifying Asymmetry and Performance of Lower Limb Mechanical Muscle Function in Male and Female Varsity Soccer and Hockey Athletes
Fatemeh Rezapoor	13	Dynamic Contrast-enhanced (DCE) MR Imaging: A Promising Approach to Differentiate True Cancer and Pseudo Progression in Glioblastoma Patients
Tiffany Dang	15	Improved Harvest of Equine Cord Blood Mesenchymal Stem Cells from Microcarriers in Stirred Suspension Bioreactors
Robyn Scholz	17	Investigating Sagittal Plane Lower Limb Kinematics in Children and Adolescents with Juvenile Idiopathic Arthritis
James Colter	19	Implementation of Electromechanical Controls for Agitation Rate in a Bioreactor System
Sara Hassanpour-Tamrin	21	Design of a new Dynamic Microfluidic Separation System for Exosome Isolation
Pavey Gill	23	Creating Microfluidic Device for Cell Analysis
Tannis Kemp	25	ANALYSIS OF BONE QUALITY AFTER KNEE INJURY IN AN OVINE MODEL

Clayton Molter	27	Development of an Intraoral Force Measurement Device for Jaw Reconstruction Patients
Mahdi Moezzi	29	Morphological alterations of cultured neurons in response to the mechanical properties of hydrogel
Nikhil Vastarey	31	Towards an Improved Gluten Detection Device
Kar Wey Yong	33	Paracrine effects of mesenchymal stem cells on in vitro cardiac fibrosis model
Anand Masson	35	Investigating the role of cell cycle activation in stem cells on cartilage regeneration in vivo
Salah Alheejawi	37	Automated lymph node segmentation in histopathological images
Luke Goudie	39	Pathological Mitochondrial Fission and its Role in IBD
Mehrdad Hosseini Kalajahi	41	Effect of partial volume correction on QCT-FE predictions of subchondral stiffness
Zahra Hosseinpour	43	Multiple Sclerosis Lesion Segmentation: Comparison of a Connected-Component Labeling Method with an Open Source Software
Syed Jafri	45	Normative: A Research Translation Portal for Generating, Disseminating and Sharing HR-pQCT data
Mohsen Janmaleki	47	Enhanced Cell-Substrate Impedance Sensing for Neuronal Differentiation Monitoring
Jumana Joury	49	Development and Usability Testing of a Surgical Guide for Autologous Breast Reconstruction
Sultan Khetani	51	Miniaturized biosensor for the diagnosis of Central nervous system (CNS) injuries
Emily Kuervers	53	Tuning the Elastic Modulus of Bio-Compatible Hydrogels
Yan Liang	55	Chondrogenic Differentiation of Synovial Fluid Mesenchymal Stem Cells on Human Meniscus-Derived Decellularized Matrix Requires Exogenous Growth Factors
David Garrett	57	Hydration Monitoring with Microwaves: A Feasibility Study"
Maysam Alnajjar	59	Synthesis of Silicate-based Magnetic Nanoparticles for the Removal of Pharmaceutically Active Compounds from Water
Bryce Besler	61	Rapid Semi-Automatic Semantic Segmentation of Full Femur and Pelvis in Computed Tomography
Elebute Ibukunoluwa	63	Reproducibility of a Region-based Method to Assess Knee Joint Mechanics and Meniscus and Cartilage Health under Load in ACL-injured Individuals
Scott Brunet	65	Efficacy of CTA in Diagnosing Non-Traumatic Non-Variceal Gastrointestinal Bleeding Prior to Transarterial Embolization after Endoscopic Failure in Managing Acute Gastrointestinal Bleeding
11:10 – 12:30 pm		**<u>Student Podium Presentation Session #2</u>** **Session Chairs:** Scott Sibole, Alex Wyma
Huiquan Wang	07	Automated Detection of Mesial Temporal Sclerosis Based on Multiple Hippocampal Features in T1-weighted MRI Images

Douglas Kondro	08	SCALING UP MICROTISSUE PRODUCTION USING MICROWELLS
Adrian Teare	09	Validating a new HR-pQCT-based method for predicting failure load of the distal radius
Faranak Heidari	10	Dual regression analysis of resting state fMRI in IBD patients
Samia Rahman	11	Oxygen Tension Modulated In Vitro Chondrogenesis of Infrapatellar Fat Pad-Derived Mesenchymal Stem Cells through Differential Proliferation
Amy Bunyamin	12	Defining monitoring time intervals for high-resolution peripheral quantitative computed tomography-based cortical bone properties in children
Jolene Phelps	13	Effects of Culture Duration and Medium on the Mesenchymal Stem Cell Secretome

12:30 – 1:45 pm **LUNCH – Glacier Chinook**

1:45 – 2:30 pm

INDUSTRY PANEL SPEAKERS:

Dr. Craig Good, President and Senior Consultant of Collision Analysis, Collision Analysis (Calgary) Ltd

Dr. Pierre Lagace, Clinical Research Manager, EOS Imaging

2:30 – 2:35 pm **BREAK – Group Pictures**

Poster Session #2 (EVEN NUMBERED POSTERS)

Sponsored by SSE The Microsystems Hub

COFFEE/BEVERAGE BREAK

2:35 pm – 3:50 pm

Judges: University of Calgary: Drs. Sarah Manske, Elena Di Martino, John Bertram, Mark Ungrin, Ian Lewis, Mike Kallos, Roman Krawetz

University of Saskatchewan: Drs. Emily McWalter, James Johnston

Leanne Young	2	Design overview of an automated running wheel to examine recovery of spinal cord injured (SCI) mice
Kevin Boldt	4	Single Fibre Force Production in the Triceps Surae Following Chronic Exercise Training
Nabangshu Das	6	Altered Synovial Fluid Proteoglycan 4 (PRG4) / Lubricin Concentration and Structure in Rheumatoid and Juvenile Inflammatory Arthritis
Seyedmahdi Hosseinitabatabaei	8	Ex vivo Validation and In vivo Repeatability of HR-pQCT FE-based Distal Radius Bone Strength
Madeline Martel	10	Quantitative magnetic resonance imaging (qMRI) of the meniscus in the knee joint in the unloaded and loaded conditions

	Muhammad Omer	58	Evaluating Strategies of Extracting Prior Information from Acoustic Signals for Microwave based Breast Imaging Techniques
	Erin Roberts	60	Process Development for the Expansion of Equine Cord Blood Derived Mesenchymal Stem Cells in Bioreactors
	Scott Sibole	62	A Method to Measure 3D Micro-scale Deformation of Biological Tissue
	Paria Vakil	64	Addressing challenges in Measuring Stresses on Knee Cartilage using Fiber-optic Sensors
3:50 – 5:10 pm			**Student Podium Presentation Session #4** **Session Chairs:** Jolene Phelps, Eng Kuan Moo
	Guomin Ren	14	Increased serum levels of CCL22 after exercise may be a marker of cartilage degeneration and pain in individuals with a previous joint injury
	Colleen Moore	15	Transforming growth factor and hypoxia signaling regulate meniscus-like extracellular matrix production by human meniscus cells
	Alex Wyma	16	Quantifying the Effect of Shear Stress on Murine Embryonic Stem Cell Aggregates
	Mehdi Shekarforoush	17	Correlation between translational and rotational kinematic instabilities and osteoarthritis development in an in vivo ovine model of ACL injury
	Nikoo Soltan	18	Cortical porosity assessment in the radius through comparison with synchrotron-based measures
	Ashley Johnston	19	Validity of Vertical Oscillation Measures Using a Markerless Motion Capture System
	Kalvin Wu	20	EXPERIMENTAL APPROACH TO THE MECHANICS OF AGONIST MUSCLES
6:00 – 7:00 pm			**DINNER – Glacier Chinook**
7:00 pm			**"THE GREAT CHALLENGE"** Sponsored by priMED Medical Products
8:00 pm			**SOCIAL – ROSE AND CROWN, BANFF AVENUE - MAP AVAILABLE**

SUNDAY

7:15 – 8:15 am	**BREAKFAST – Glacier Chinook**
8:15 – 8:45 am	**Checkout**
8:45 – 9:25 am	**Guest Speaker #2:** **Dr. Gordon Sarty, University of Saskatchewan** **Session Chairs:** Lindsay Loundagin, Colin Firminger

9:25 – 10:20 am

Student Podium Presentation Session #4

Session Chairs: Geoff Michalak, Andres Kroker

Simon Wong	21	Extracellular recordings of rat cortical and hippocampal neurons with high signal resolution using novel multi electrode arrays
Tessa Exley	22	Methods for Gait Event Detection in Running Using Accelerometer Data
Kadin Majcher	23	Repeated use of single-use veterinarian needles
Russell McWhae	24	Intercellular Signaling in the Intervertebral Disc with applied Mechanical Load
Ryan Schroeder	25	Parkour wall climbing: Simple physics of an extreme task

10:20-10:40 am

Poster Session #3 (FINALISTS ONLY)

Judges: University of Calgary: Drs. Sarah Manske, Elena Di Martino, John Bertram, Mark Ungrin, Ian Lewis, Mike Kallos, Roman Krawetz

University of Saskatchewan: Drs. Emily McWalter, James Johnston

COFFEE/BEVERAGE BREAK; Activity from BMEG

10:40 – 11:35 am

Student Podium Presentation Session #5

Session Chairs: Colin Firminger, Eng Kuan Moo

Elnaz Pouranbarani	26	A Novel Approach for Fitting the Parameters in Cardiac Cellular Model through a Linear Least Squares Formulation of Currents
Christopher O'Neill	27	Automated Segmentation of Callus and Cortical Bone in Distal Radius Fractures Using Machine Learning
Bingjie Ma	28	Ultrafast High-Frequency Focused Beam Blood Flow Imaging

11:45 – 12:30 pm

Final Award Presentations

CLOSING REMARKS

REMINDER:
Please return all name tags and judge's clipboards at the end of the conference. We thank you for your cooperation.

SEE YOU IN 2018!

Banff Park Lodge Map and Meeting Location **(star indicates Rose and Crown)**

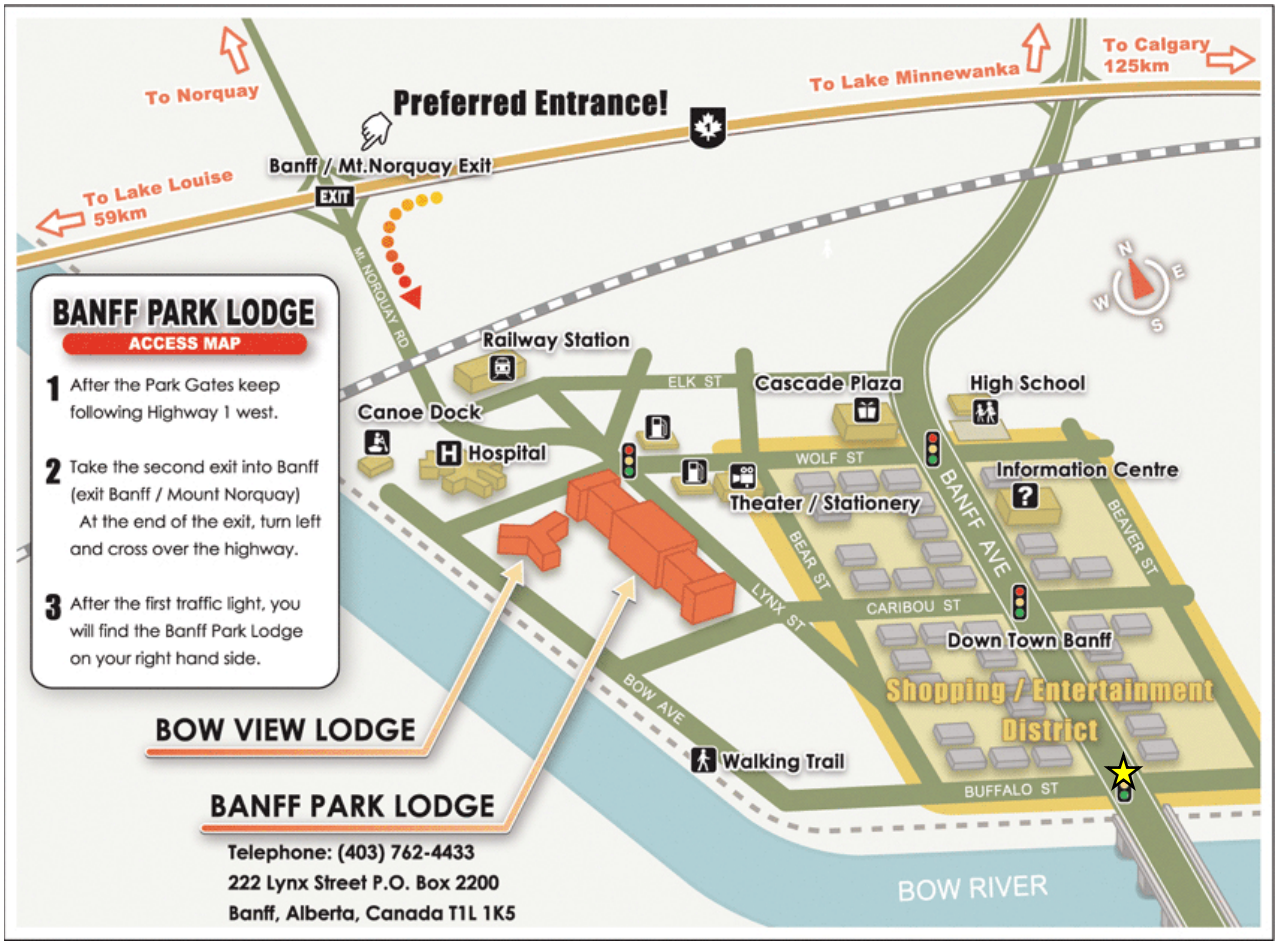

ROSE AND CROWN FOR SATURDAY NIGHT

To get to the Rose & Crown from the Banff Park Lodge, turn right out of the hotel and walk south on Lynx St, turn left and walk along Caribou St until Banff Ave. The Rose & Crown is located on the upper floor the two-story building directly across Banff Ave, on the northeast side of the intersection.

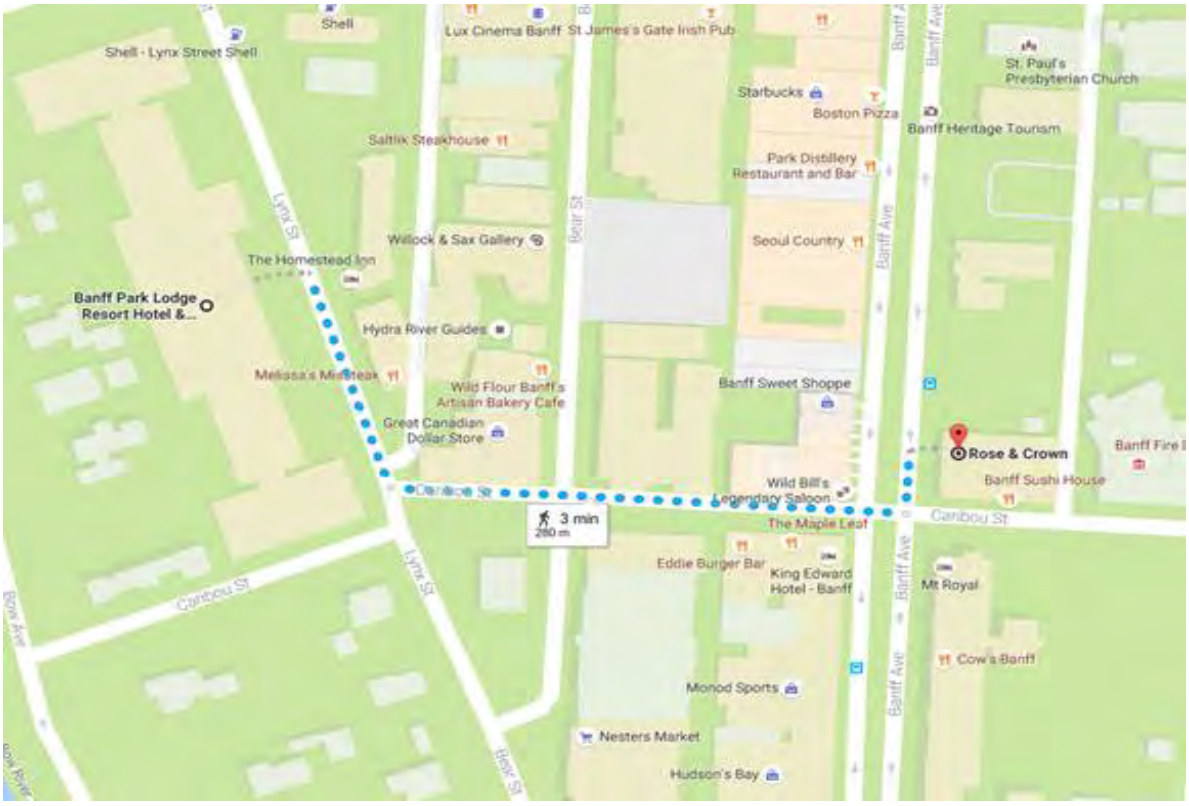

GUEST SPEAKER #1 – Dr. Joseph Cafazzo, University of Toronto

Dr. Joseph Cafazzo is Lead for eHealth Innovation and Executive Director and Founder of Healthcare Human Factors, both located with University Health Network (UHN), a teaching hospital of the University of Toronto. As a biomedical engineer, he has spent his entire career in a hospital setting. By observing healthcare delivery from the inside, he works on ways to keep people out of hospital by creating technologies that allow for self-care at home.

He is an active researcher of the use of technology to facilitate patient self-care of complex chronic conditions such as diabetes, asthma, end-stage renal disease, and congestive heart failure. He has advised and conducted research for public sector policy makers and private sector medical technology companies on the design and safety of technology in healthcare. He has contributed to the development and promotion of the artificial pancreas, critically developing device interoperability standards, analyzing user experience, and examining technical platforms.

He has created numerous award-winning mobile health apps, including bant, an application design for adolescents for the self-management for type 1 diabetes, which received the Stanford 2.0 Award. This work was also recognized by the Canadian Health Informatics Association, with their Excellence in Telehealth Award and the Dr. Mo Watanabe Lecture.

Dr. Cafazzo is an associate professor at the University of Toronto, in the areas of clinical engineering, human factors, and health informatics and is the recipient of the Career Scientist award by the Ontario Ministry of Health and Long Term Care.

GUEST SPEAKER #2 - Dr. Gordon Sarty, University of Saskatchewan

Dr. Gordon Sarty is a mechanical engineer (UNB, 1982) with a PhD mathematics (University of Saskatchewan, 1995). He designed mechanical and thermal systems for space shuttle and sounding rocket experiments with SED Systems in the 1980's. During his postdoctoral time at the Royal University Hospital in Saskatoon he applied MRI to many biomedical problems including fMRI. With some fMRI knowledge and an MRC Scholarship he moved to the Department of Psychology in 2000. Currently he is the Psychology department head and the chair of the Biomedical Engineering Division at the University of Saskatchewan.

Abstract:

The Development of Gradient-Free MRI for Solar System Inhabitants

Gordon E. Sarty, PEng, PhD
University of Saskatchewan

Astronauts on long-term space missions face a variety of physiological challenges including muscle and bone mass loss and neurologic damage from cosmic radiation. MRI studies of astronauts on the International Space Station (ISS) have been limited to mission before and after studies. Imaging during flight is essential for a deeper understanding of the time course of physiological changes in astronauts and this will be especially true once they leave low Earth orbit for lunar and other destinations in the Solar System.

Since 2014 the Canadian Space Agency (CSA) has been funding the development of extremity-sized gradient-free MRIs for eventual deployment on the ISS. The CSA funding, combined with funding from NSERC, has allowed the development of this new MRI technology to proceed from mathematical theory to prototype construction and demonstration. Gradient-free MRI, as we have implemented it, uses a combination of non-uniform magnetic fields and radio frequency (RF) encoding. Currently we are building a third prototype for flight on NRC's Falcon 20 jet in 2018 to see how well the MRI performs in zero-gravity. Ultimately, we aim to develop gradient-free MRI for remote and specialized Earth-bound service as well.

INDUSTRY PANEL Speaker

Pierre-Yves Lagace,
EOS Imaging

I've obtained B.Eng of Mechanical Engineering from McGill University (Montreal, QC), and then an International Joint Ph.D. in Biomedical Engineering from École de Technologie Supérieure (Montreal, QC), and Arts et Métiers Paris Tech (Paris, France). My Ph.D. research focused on shoulder imaging, modeling and motion analysis from biplanar X-rays using the EOS system, with the objective of providing a better understanding of the causes of loss of range-of-motion and pain in patients with rotator-cuff tears. I've spent 2015-2016 in the Bone Imaging Laboratory doing a postdoc with Steve Boyd, and have since moved on to be Clinical Research Manager, North America with EOS imaging.

EOS imaging

EOS imaging is a global medical device company that develops and markets advanced imaging and image-based solutions for musculoskeletal pathologies and orthopedic surgical care, including a full body, low dose medical imaging system, a 2D/3D modeling workstation, and a suite of online, 3D surgical planning solutions for the spine, hip and knee.

INDUSTRY PANEL Speaker

Craig A. Good, Ph.D., P.Eng.
Collision Analysis (Calgary) Ltd.

Craig is the President and Senior Consultant of Collision Analysis. He began at the company as an Engineering Consultant in 2002, and took over operations of the company in 2009. In 2007, Craig received a Ph.D. in Mechanical Engineering specializing in Injury Biomechanics from the University of Calgary. He previously earned his B.A.Sc. and M.A.Sc. in Mechanical Engineering at the University of Waterloo. As a result of work at a Tier 1 automotive seatbelt supplier, Breed Technologies (Sterling Heights, MI), Craig is a co-inventor on a U.S. and a European seat belt patent. He has authored and presented numerous peer reviewed scientific papers. His role as an Adjunct Assistant Professor at the University of Calgary, Schulich School of Engineering has led to recent scientific publications on helmet performance and longevity.

Collision Analysis (Calgary) Ltd.

Collision Analysis was formed in 1979 to serve a recognized need for specialized consulting services in the area of automotive forensics. The company currently provides multi-disciplinary investigations including accident/collision reconstruction, injury biomechanics, human factors, and safety systems with related failures and defects. Collision Analysis is honoured to have again been selected to conduct field investigations of motor vehicle collisions and safety-related defects in the Western Canada region for Transport Canada until 2023.

2017 ALBERTA BME CONFERENCE SPONSORS – THANK YOU!!

GOLD SPONSORS – University of Calgary

Biomedical Engineering Graduate Program
Centre for Bioengineering Research and Education

SILVER SPONSORS – University of Calgary

McCaig Institute
Libin Cardiovascular Institute

BRONZE SPONSORS

Schulich School of Engineering /The Microsystems Hub
Canadian Society for Biomechanics
priMED Medical Products
VWR International Inc.

McCaig Institute for Bone and Joint Health

Silver Level Sponsor

The McCaig Institute for Bone and Joint Health is home to basic scientists, physicians, biomedical engineers, health system experts and researchers in training working together to improve the bone and joint health of Albertans. Through research excellence and regional partnerships with Alberta Health Services' Bone and Joint Health Strategic Clinical Network and the Alberta Bone and Joint Health Institute, the McCaig Institute has become a global leader in musculoskeletal research.

Research in the McCaig Institute focuses on **understanding** the causes of bone and joint conditions, **preventing** long-term damage, **diagnosing** disease earlier, **developing** new treatments and **transforming** research findings into real-world solutions.

Together, we are committed to a future of pain free *Mobility for Life***.**

Libin Cardiovascular Institute of Alberta,
Silver Level Sponsor

The Libin Cardiovascular Institute of Alberta

The Libin Cardiovascular Institute of Alberta coordinates cardiovascular science research, education and patient care as an entity of both Alberta Health Services (Calgary) and the University of Calgary. It provides education and training of health-care professionals and offers world-class treatment using new technologies and access to cardiac services. The Libin Institute includes more than 175 basic research, clinicians and clinical research members who serve two million people in Southern Alberta, Saskatchewan, and Eastern British Columbia. It is committed to enabling cardiovascular health through innovative research and outstanding clinical care. For more information, visit libininstitute.org.

BIOMEDICAL ENGINEERING

Ready to make a difference

Located in the engineering capital of Canada, the University of Calgary's biomedical engineering program is advancing knowledge and solving problems in animal and human biology, medicine and health-care by educating the next generation of leaders.

READY TO CONTRIBUTE

Our undergraduate students have the strengths of a traditional engineering degree at the Schulich School of Engineering, advanced knowledge of biomedical engineering and valuable hands-on work experience.

MULTI-DISCIPLINARY TEAMWORK

Our graduate students participate in teams with researchers in engineering, kinesiology, medicine, nursing, science and veterinary medicine at an institution committed to investing significantly in biomedical research.

PARTNERS IN RESEARCH

Researchers work towards making an impact through scientific discoveries, innovative and market-driven technologies, and solutions to enhance the wellness and well-being of all throughout the lifespan. We look for opportunities to link with industry and international entities to provide market-ready graduates and R&D solutions.

Collaborative, skilled and experienced – the University of Calgary's biomedical engineers are ready to help your team make a difference today.

For inquiries email **bme@ucalgary.ca** | **ucalgary.ca/bme**

UNIVERSITY OF CALGARY

NOTES

NOTES

PODIUM PRESENTATION ABSTRACTS

More numerous subchondral cysts are associated with higher lateral tibial subchondral bone mineral density in patients with knee osteoarthritis

Burnett, WD; Kontulainen, SA; McLennan, CE; Hazel, D; Talmo, C; Wilson, DR; Hunter, DJ; Johnston, JD

Introduction: Osteoarthritis (OA) is a debilitating joint disease marked by altered cartilage and underlying bony tissues [1]. Subchondral cysts are a commonly observed, but poorly understood, feature in knee OA [2,3]. Clinical quantitative computed tomography (QCT) has potential to characterize cysts *in vivo* but it is unclear which specific cyst parameters (e.g., number, size) are associated with clinical signs of OA, such as disease severity or pain. The objective of this study was to use QCT-based image-processing to explore relationships between proximal tibial subchondral cyst parameters and subchondral bone density as well as clinical characteristics of OA (alignment, joint space narrowing, OA severity, pain) in patients with knee OA.

Methods: The preoperative knee of 42 patients (17M:25F, mean age 64 ± 10.2 years) was scanned using QCT, scored for pain using the Western Ontario and McMaster Universities Arthritis Index (WOMAC) [4], and classified for OA severity [5]. We also included medial and lateral joint space narrowing (JSN) and CT-measured joint alignment in our analysis. Serial tibial QCT images were semi-automatically segmented, and cysts were identified and manually segmented using commercial software (Analyze 10.0; Mayo Foundation) with an interactive touch-screen tablet (Cintiq 21UX, Wacom). Cysts were considered as an approximate elliptical or spherical volume of lower greyscale surrounded by higher greyscale through visual inspection and guided by subject-specific half-maximum-height threshold values [6, 7]. Only cysts within the subchondral region at a depth of up to 7.5mm from the subchondral surface [8] were evaluated. We used a custom algorithm (Matlab 2016a, MathWorks) to measure cyst parameters (number of cysts; cyst number and cyst volume fraction per total regional subchondral volume; total, maximum, average, minimum, and standard deviation of cyst volume) and proximal tibial bone mineral density (BMD) with and without cysts [9,10]. Cyst parameters and BMD were evaluated over total, medial, and lateral subchondral regions of distal tibia. Pearson's and Spearman's rank correlation were used to determine associations between cyst parameters and clinical characteristics of OA.

Results: At the lateral region, cyst number was associated with BMD (both excluding and including cysts) (r=0.58, p<0.001) (Figure 1). Alignment and lateral JSN were associated with all cyst parameters at the lateral region (p<0.05). No associations were noted between cyst parameters and OA severity or pain.

Conclusion: At the lateral region, cyst number and volume were associated with various patient characteristics including BMD, alignment, and JSN. This is the first study to use clinical QCT to explore subchondral tibial cysts in patients with knee OA, and provides further evidence of the relationships between subchondral cysts and clinical OA characteristics.

References: [1] Hunter 2006; [2] Javaid 2012; [3] Crema 2010; [4] Bellamy 1998; [5] Kellgren 1957; [6] Chiba 2014; [7] Kontulainen 2007; [8] Burnett 2017; [9] Chen 2015; [10] Burnett 2015.

Figure 1. Scatterplot and Pearson's correlation coefficient (r) of the relationship between lateral BMD (excluding cysts) and lateral cyst number.

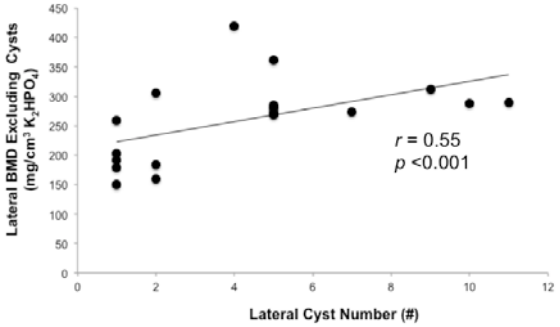

MECHANICAL FATIGUE OF CORTICAL BONE IN TENSION AND COMPRESSION: EFFECTS OF MICROARCHITECTURE

Lindsay L. Loundagin, Annette M. Harvey, W. Brent Edwards
Human Performance Laboratory, Faculty of Kinesiology, University of Calgary
email: lindsay.loundagin@ucalgary.ca

Introduction

Cyclic loading of bone causes the accumulation of microdamage in the form of cracks, which may eventually lead to fatigue fracture. The development of microdamage due to cyclic loading is thought to be influenced by microarchitecture (1). Features, such as Haversian systems, have the potential to dictate microcrack initiation and propagation. However, the role microarchitecture plays in the accumulation of microdamage, and ultimately fatigue failure, under different modes of cyclic loading is largely unknown. The purpose of this study was to quantify the effects of microarchitecture on the fatigue life of bovine cortical bone when cyclically loaded in compression and tension.

Methods

Cortical bone samples were obtained from bovine femora and tibiae and machined into a waisted geometry with a central gauge section 5.25 mm in diameter. All samples were imaged using Scanco microCT 100 (Scanco Medical AG, Switzerland) with a resolution of 5 μm. Microarchitecture was quantified by the median canal diameter (Ca.Dm), median canal separation (Ca.Sp), and porosity.

Mechanical fatigue testing was performed on an Instron Electropuls E3000 test frame (Instron, Norwood, MA). Seventeen samples were cyclically loaded in either zero-compression (n=9) or zero-tension (n=8) at a frequency of 4.35 Hz. The loading magnitude was chosen as 45% of the ultimate strength previously reported (3) for each loading mode, such that the compression and tension groups were tested at 95 and 73 MPa, respectively. Fatigue life was quantified as the number of loading cycles until failure, which corresponded with complete fracture in all cases. Pearson product-moment correlation was used to determine the relationships between microarchitectural features and fatigue life (α=0.05).

Results

When loaded in tension, porosity (r=0.647, p=0.083) demonstrated a strong positive correlation with fatigue life, but no relationship was observed for Ca.Dm (r=0.263, p=0.529) or Ca.Sp (r=-0.128, p=0.763). In compression, porosity (r=-0.639, p=0.064) and Ca.Dm (r=-0.738, p=0.023) illustrated a strong negative correlation with fatigue life, but no relationship was observed for Ca.Sp (r=0.078, p=0.842).

Conclusions

The findings from this study suggest that microarchitecture may influence cortical bone fatigue behaviour in a complex manner that is dependent on loading mode. Porosity was strongly correlated with fatigue life in both compression and tension, however, the two modes of loading illustrated opposing correlations (Fig 1). Similarly, canal diameter was negatively correlated with fatigue life in compression but unrelated to fatigue life in tension. These contrasting relationships may be indicative of different damage mechanisms occurring under each loading mode. For instance, in compression damage may accumulate more readily in the vicinity of larger canals, whereas in tension, damage may be relatively unaffected by these features. Future work will image damage due to cyclic loading to further elucidate the mechanisms of fatigue failure of bone under different loading modes.

References

1.Carter (1977). *Clin Orthop Relat Res*. **127**:265-74.
2.Vashishth. (2001). *J Orthop Res*. **19**: 414-420.

Figures

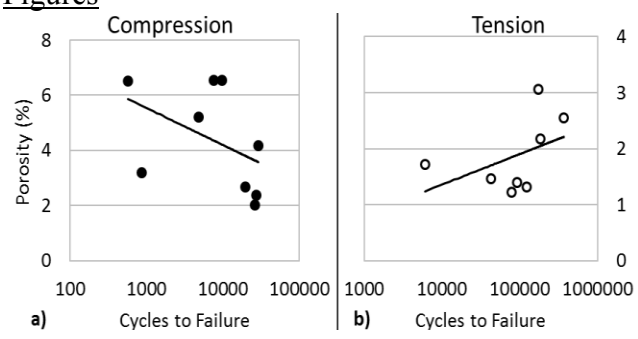

Figure 1: Porosity was negatively correlated with fatigue life in compression (a) but positively correlated in tension (b).

Automatic Bolus Arrival Time (BAT) Detection for Dynamic Contrast-Enhanced (DCE) Imaging with Under-sampling of k-Space

Justin Park,[1,2,4] Fatemeh Rezapoor,[2,4] Linda B. Andersen,[1,4] Richard Frayne,[1-4] R. Marc Lebel[1,2,4,5]

[1]Radiology, [2]Biomedical Engineering, and [3]Clinical Neurosciences, Hotchkiss Brain Institute, University of Calgary; [4]Seaman Family MR Centre, Foothills Medical Centre; and [5]General Electric Healthcare, Calgary, Alberta

Introduction

Dynamic contrast enhancement (DCE) is an important MR technique for angiography and tissue perfusion and wall permeability imaging. DCE collects a set of baseline data before and after the arrival of a contrast agent (CA) in the tissue of interest. The DCE technique is dependent on how MR data are sampled over time, this process helps to define the spatial and temporal resolutions of the final images. We used a strategy to enable reconstruct images with variable temporal frame rates. A key parameter is accurate knowledge of the bolus arrival time (BAT) of the CA in the tissue. We proposed an automatic method to estimate the BAT, enabling automatic selection of temporal frame rates of the images.

Methods

MRI data were acquired on a 3 T scanner (MR750; General Electric) with a 12-channel head/neck coil. A T1-weighted spoiled gradient echo sequence with TR/TE = 5 ms/ 2 ms, 15° flip angle, field-of-view of 24 × 24 × 24 cm^3 and an acquisition matrix of 256 × 240 × 120 was used. The k-space data were under-sampled in the k_y and k_z directions but not the readout direction (k_x), Undersampling enabled us to achieve good temporal resolution with minimal loss of fine details due to poor sampling of the high frequency k-space regions. Using this k-space data, we can automatically estimate the BAT in five steps (Figure 1): 1) Extract the frequently sampled central line of k-space ($k_y = k_z = 0$). 2) Determine the readout position (along k_x) that has the most robust MR signal over time. 3) Filter and take the derivative of the most robust readout position with respect to time. 4) Locate the first inflection point in the slope that corresponds to the first large positive peak of the derivative in time. 5) Use the slope to regress the signal to the baseline. The intersection of the signal regression line and the baseline signal is the estimated BAT. We have evaluated our method in 14 patients with brain tumor.

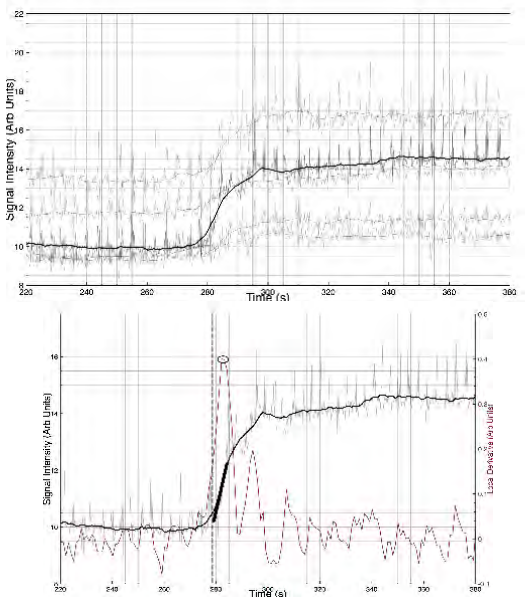

Figure 1. (Top) MR signal intensity over time in a single patient determined from sampling the center of k-space. Readout position has been randomly chosen to illustrate different curves (grey lines). A moving average filter was used to reduce noise and then the most reliable readout location found (bold black line). (Bottom) Derivative of the most reliable readout position was used to obtain local slope as a function of time (red line) and the first inflection point has been denoted by the black circle. Regress the maximum slope fit (bold black line) back to the baseline to estimate BAT (vertical dashed line).

Results

BAT was successfully estimated in all 14 (100%) patients. The estimated BAT had an error ≤2.5 s. The accuracy of this estimate was limited by how fast we acquired each point in k-space (TR = 5 ms). In practice, despite this error, the estimated BAT was able to guide image reconstruction at variable temporal resolutions.

Conclusions

The proposed method correctly estimates the BAT, providing information to automatically define temporal resolution reconstruction windows suitable for time-resolved angiography, perfusion and permeability imaging. Furthermore, errors due to patient-specific timing delays can be eliminated, improving workflow efficiency and reducing acquisition error.

Re-engineering Islets for Improved Performance and Graft Function

Yu Y, Gamble A, Pawlick R, Pepper A, Salama B, Toms D, Razian G, Ellis C, Bruni A, Gala-Lopez B, Lu L, Chiu C, Abdo S, Korbutt G, Shapiro AM, Ungrin M.
Biomedical Engineering Graduate Program, University of Calgary

Introduction

Islet transplantation is a promising approach to the treatment of Type 1 Diabetes(*1*). However, a major clinical limitation for current islet transplantation is the inefficient survival and engraftment in the immediate post-transplant period(*2*). One reason is likely that the size of the native islets is too large for sufficient oxygen and nutrition delivery in avascular condition immediately after transplant(*3*). Quantitative modeling of oxygen delivery within islets shows significant benefits to smaller islets(*4*), and consistent with this concept, smaller human islets have been reported to perform better than larger ones in a clinical setting(*5*). We hypothesize that there exists an optimal aggregate size, at which islet cell aggregates will exhibit significantly improved viability and insulin secretion capacity, due at least in part to improved oxygen transport properties. Subsequently, the optimal outcome from in vitro experiments will be validated in vivo. We hypothesize that in vitro results will be generally predictive of and consistent with in vivo survival and function.

Methods

Aggrewell system is used to re-aggregate the native islets to form pseudoislets. Re-aggregated islet cells were cultured for 3-5d before transplantation. DNA content, Insulin production capacity have been tested in Glucose Stimulated Insulin Secretion (GSIS) assay pre-transplantation. Islets and pseudoislets have then been transplanted into STZ-induced diabetic Rag1 KO mice under the kidney capsule. During the 60-day post-transplant period, Blood glucose has been monitored regularly, with IPGTT tested before nephrectomy. Harvested graft have assayed immunohistochemically for endocrine cell subtype portions and vessel distribution.

Results

We successfully re-aggregated the native islet cells to formed pseudoislets in our microwell system by using human donor islets. The direct comparison showed that the pseudoislets significantly outperformed the native islets, reproducibly exhibiting a 2.9-fold increase in terms of insulin secretion per input cell basis ($p<0.05$). Through in vitro culture we have discovered a better oxygen access and maintained significantly lower apoptosis level among pseudoislets. At 500 IEQ marginal mass transplantation level, the proportion of mice restored euglycemia in pseudoislets group is seemed to be improved over native islets group and with improved glucose clearance profile. Further quantitative analyses of islet graft have suggested interesting similarities and differences in terms of graft composition and vessel distribution.

Conclusions

This novel approach of generating size-controlled pseudoislets have substantially improved over conventional methods. Pseudoislets generated have showed enhanced effectiveness and function both in vitro and in vivo compared to unmodified native islets. By further systematically optimizing this bioprocess, we will continue enhancing pseudoislets that could be rapidly applied to boost the effectiveness of current islet transplantation. The results of this project will yield a substantial improvement in the consistency and efficacy of islet cell preparations for transplantation; and lay a foundation for rapid transition to the clinic, resulting in significant advances in human health through the treatment of insulin-dependent diabetes.

References

1. W.-P. You, M. Henneberg, *BMJ Open Diabetes Res. Care*. **4**, e000161 (2016).
2. A. N. Balamurugan *et al.*, *Am. J. Transplant.* **14**, 2595–2606 (2014).
3. D. Zorzi *et al.*, *Cell Transplant.* **24**, 11–23 (2015).
4. P. Buchwald, *Theor. Biol. Med. Model.* **6**, 5 (2009).
5. R. Lehmann *et al.*, *Diabetes*. **56**, 594–603 (2007).

Magnetic Resonance Image Sequence Classification using Convolutional Neural Networks

Luis Souto Maior,[1,4] Mariana Bento,[2-5] Marina Salluzzi,[5] Richard Frayne[1-4]
[1]Biomedical Engineering, [2]Radiology and [3]Clinical Neurosciences, Hotchkiss Brain Institute, University of Calgary;
[4]Seaman Family MR Centre and [5]Calgary Image Analysis and Processing Centre, Foothills Medical Centre, Calgary, Alberta

Introduction

Deep convolutional neural networks (CNN) have been shown to perform well in different medical imaging tasks. However, very large amounts of labelled data are needed for training supervised models.[1] If data is available but not correctly labelled or identified, it must be discarded unless manually identified, often by an imaging specialist in a time-consuming process especially when dealing with thousands of images. In this work, we approach the problem of unlabeled medical images by proposing a CNN for classifying the type of magnetic resonance (MR) images. Unlabelled data was classified by their acquisition sequence (T1-weighted, T1-w; T2-w; post-contrast T1-w, T1-c; and fluid attenuated inversion recover imaging, FLAIR).

Methods

The dataset used for the MR sequence classification experiments was the MICCAI BRATS 2016 database.[2] This data set is comprised of 220 MR head scans of patients with low-grade glioma and high-grade glioblastoma. It consists of T1-w, T2-2, T1-c, and FLAIR images. 3D scan volumes (240 × 240 × 140) were provided already pre-registered and skull-stripped.[2] The 240 × 240 2D axial slices were obtained from the dataset. For the purpose of reducing the processing time, the images were resized using bi-cubic interpolation to a 60 × 60-matrix. After processing, the dataset contained 30,800 (140 × 220) images (**X**). The class of each image, retrieved from the BRATS dataset, was one-hot encoded, *i.e.*, [1,0,0,0] for T1-w, [0,1,0,0] for T2-w, *etc.*, resulting in each of the images having its respective label (**T**). These labels were used as the targets for the classifier training.

A CNN was trained to classify the data as being T1-w, T2-w, T1-c, or FLAIR images. The architecture of the CNN is described and illustrated (Figure 1). The dataset {**X**, **T**} was normalized and partitioned: 70% of the data for the training, and 30%, for validation set. The network was trained five times, each for 50 epochs, and the validation set overall accuracy was recorded.

Results

The network achieved an overall classification accuracy of 92.8% ± 3.2% (mean ± standard deviation). The average confusion matrix is depicted in Table 1.

Conclusions

This work serves as a proof-of-concept for using CNNs for classification of medical imaging modalities, specifically across the four common MR sequences (T1-w, T2-w, T1-c and FLAIR). Although the results are very good, there are additional opportunities for improvement including 1) classifying between MR and other imaging modalities, 2) using the volumetric data as inputs, 3) implementing a consensus-based system by averaging the outputs of classifications from the same scans, and 4) training a network with different projections of the same scan.

References

[1] Tajbakhsh, N, *et al*. Convolutional Neural Networks for Medical Image Analysis: Full Training or Fine Tuning? *IEEE Trans on Medical Imaging* 2016; **35**: 1299.

[2] Menze, BH *et al*., The Multimodal Brain Tumor Image Segmentation Benchmark (BRATS) *IEEE Trans on Medical Imaging* 2015; **34:** 1993.

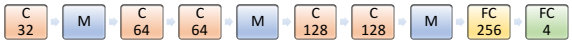

Figure 1:. Convolutional layers (C followed by n° of filters) with rectified linear units and 3 × 3 filters, max-pooling layers (M) with 2 × 2 filters. At the end of the network, two-fully connected layers (FC followed by n° of neurons) serve as the final classifier.

*Table 1: Average confusion matrix. **Y** are the predicted labels and **T**, the correct labels.*

Y \ T	T1-w	T2-w	T1-c	FLAIR	Total
T1-w	**2003**	46	34	47	2130
T2-w	46	**2133**	65	67	2311
T1-c	66	63	**2227**	59	2415
FLAIR	48	64	63	**2209**	2384
Total	2163	2306	2389	2382	**8572**

In vitro cell surface markers are insufficient to identify *in vivo*/*in situ* multipotent synovial mesenchymal stem cells isolated from normal or osteoarthritic knees

Nedaa Al-Jezani[1,4], Pam Railton[2], Jim Powell[2,3], Roman Krawet [1,3,4]
1 Medical Science Graduate Program, University of Calgary, AB, Canada, 2 Department of Surgery, University of Calgary, AB, Canada, 3 McCaig Institute for Bone and Joint Health, AB, Canada, 4 Department of Cell Biology and Anatomy, University of Calgary, AB, Canada.

Introduction

While previous clinical trails have employed mesenchymal stem cells (MSCs) as a therapy for osteoarthritis (OA), only a few have demonstrated positive outcomes. One potential reason behind this, could be the use of inappropriate MSCs as these cell populations can be highly phenotypically heterogeneous. Therefore, it is necessary to establish clear standard protocols that can identify "true" MSCs with the greatest potential to affect repair and/or contribute to a treatment effect. The overarching goal of this project is to determine which currently employed MSC cell surface markers can be utilized to increase the accuracy of isolating MSCs population directly from human tissue with the greatest differentiation capacity and eliminating subpopulation with inferior potential.

Methods

Synovial MSCs were isolated from OA patients undergoing joint replacement and normal cadaveric knees. The biopsies were digested with collagenase type IV and the resultant cells were stained for: CD90, CD44, CD73, CD271 and CD105; the macrophage marker CD68 and viability marker FVS510. CD68+ cells and dead cells were excluded and all other cells were index sorted into 96 well plates. Expanded clones were exposed to adipogenic, chondrogenic and osteogenic differentiated media for 21 days. Differentiation was analyzed via qPCR and histology. A subset of each expanded clonal population before the initiation of differentiation was re-examined for cell surface expression.

Results

Regardless of the *in situ* marker profiles expression, all MSC clones, when cultured *in vitro*, converged to a unified marker profile of: CD90+, CD44+, CD73+ and CD105+. The *in situ* marker profile that was correlated with multipotent differentiation capacity of MSCs was found to be similar between OA and normal clones (CD90+, CD44+, and CD73+) (Table 1 and 2). A second cohort of patients was recruited to validate the *in situ* MSC profile, however, it was found that isolation of CD90+, CD44+, and CD73+ triple positive cells didn't guarantee multipotent differentiation potential as tested by qPCR and histology analysis (Table 3 and 4).

Conclusions

The markers currently used by the field are not capable of distinguishing MSCs with or without differentiation capacity if employed *in vitro*; this strongly suggests that MSC markers used by the field are not only markers of MSCs *in vivo* and most likely artifacts of cell culturing.

Thus, the results of this project raise a potentially larger question regarding the identification of MSCs with these standard markers. Do these markers truly describe MSCs? This question should be thoroughly addressed before MSC therapies are continued to be delivered to patients suffering from OA.

References

Phinney, D. G. Functional heterogeneity of mesenchymal stem cells: implications for cell therapy. J. Cell. Biochem. 113, 2806–12 (2012)

Figures

Table 1: A summary of cell surface marker profiles isolated from OA patients and the number of

In-Situ Profile	Frequency	MSCs	Only chondrocyte	Only Osteoblast	Only Adipocyte	Chondrocyte+ Adipocyte	Chondrocyte+ Osteoblast	Osteoblast+ Adipocyte	No Differentiation
CD90,44,73	16	6	0	1	2	3	1	1	1
CD44,73	9	5	0	1	2	0	0	0	0
CD90,105,44,73	4	0	0	0	2	1	1	0	0
CD44	3	1	0	0	0	0	1	1	0
CD90,73	1	0	1	0	0	0	0	0	0
CD105,271,44,73	1	1	0	0	0	0	0	0	0

Table 2:A summary of cell surface marker profiles isolated from normal individuals and the number of

Profile in vivo	Frequency	MSCs	Only chondrocyte	Only Osteoblast	Only Adipocyte	Chondrocyte+ Adipocyte	Chondrocyte+ Osteoblast	Osteoblast+ Adipocyte	No Differentiation
CD44,73	11	1	1	1	3	2	1	0	2
CD90,44,73	6	2	1	0	1	1	0	1	0
CD44	1	0	0	0	0	0	0	0	1

Table 3: A summary of positive population of sorted cells (CD90+, CD44+, and CD73+).

#	In Situ Profile	Adipocyte PCR/Histology	Chondrocyte PCR/Histology	Osteoblast PCR/Histology	Population Doubling Level
1	CD90,44,73	+/+	-/+	- /+	20.21
2	CD90,44,73	-/+	-/+	+/+	17.1
3	CD90,44,73	-/+	-/+	-/+	21.6

Table 4: A summary of negative mixed population.

#	Adipocyte PCR/Histology	Chondrocyte PCR/Histology	Osteoblast PCR/Histology	Population Doubling Level
1	+/+	-/+	-\-	21.3
2	-/+	-/+	-/+	21.2
3	+/+	-/+	-/-	20.21
4	+/+	+/+	+/+	20.1
5	+/+	-/+	-/+	20.22
6	+/+	-/+	-/+	21.3

Automated Detection of Mesial Temporal Sclerosis Based on Multiple Hippocampal Features in T1-weighted MRI Images

Huiquan Wang[a], Nizam Ahmed[b], Mrinal Mandal[a]
[a]Department of Electrical and Computer Engineering, [b]Department of Medicine, University of Alberta

Introduction

Mesial temporal sclerosis (MTS) is the most common pathological abnormality associated with intractable temporal lobe epilepsy [1]. Magnetic resonance imaging (MRI) is one of the most commonly used examination tools for diagnosing MTS based on characteristics of reduced hippocampal volume, increased T2/FLAIR signal and abnormal hippocampal morphology, as shown in Fig. 1. In cases with mild or bilateral hippocampal malformation, the manual volumetric analysis is widely used. However, it is time-consuming and operator dependent [2]. Therefore, the manual volumetric analysis is impractical for clinical purpose. In this paper, an automated MTS detection method is proposed to improve the efficiency of MTS diagnosis.

Methods

In the proposed technique, the T1-weighted MRI images are sequentially processed by four modules (as shown in Fig. 2): brain and hippocampus segmentation, feature extraction, principal component analysis (PCA) and classification.

First, an MRI image is segmented into three tissue types (GM, WM and CSF) and the left and right hippocampi are extracted. Second, volumetric, shape and CSF-ratio features are calculated based on the segmentation results. After that, the PCA is applied to the feature vector to reduce feature correlations and increase the detection performance. Finally, two support vector machines (LSVM and RSVM) are trained using left and right hippocampal features, respectively. LSVM and RSVM are used separately to detect left- and right-side MTS.

Results

15 left-MTS, 15 right-MTS and 15 normal T1 images are used in experiments based on leave-one-out cross validation. Table 1 shows the confusion matrix of testing. Therefore, the overall sensitivity of MTS detection is 93.3% and the accuracy is 92.2%.

Conclusion

An automated MTS detection technique is proposed based on T1 MRI image analysis and promising performance is obtained.

References

1. Y. Shinnar, Epilepsy Currents, vol. 3, pp. 115-118, Jul. 2003.
2. A. Hammers et al., NeuroImage, vol. 36, no. 1, pp. 38-47, 2007.

Figures

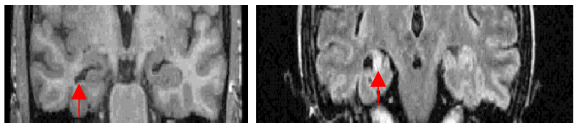

Figure 1 T1 (left) and FLAIR (right) images with MTS.

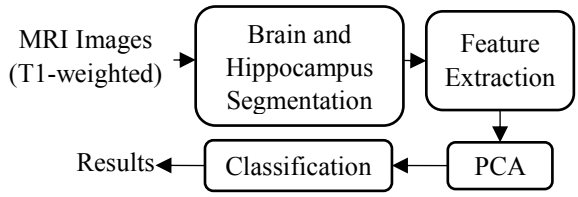

Figure 2 The schematic of the proposed technique.

Table 1 Confusion Matrix

Actual \ Predicted	MTS	NO-MTS
MTS	28	2
NO-MTS	5	55

SCALING UP MICROTISSUE PRODUCTION USING MICROWELLS

Douglas Kondro[1], Derek Toms[2] and Mark Ungrin[2]
[1]Graduate Program of Biomedical Engineering U of C, [2]Comparative Biology & Experimental Medicine, U of C

Introduction

There is a growing recognition that 3D microtissues in the form of cellular aggregates can provide improved physiological relevance over conventional adherent culture conditions [1]. A variety of methods to produce cellular aggregates exist, however scaling these methods from a high throughput study to clinical production is not trivial. The use of centrifugal forced aggregation in the form of microwells is a leading method in producing size controlled aggregates. We hypothesize that aggregation in microwells can be scaled from studies in well plates to a multi-layered static culture bioreactor (Fig 1). A particular focus will be on the device's application to stem cell differentiation protocols and diabetes treatment used in animal trials.

Methods

To maintain growth conditions from a well plate to the bioreactor, oxygen and nutrient supply was investigated. In the bioreactor, oxygen diffuses through microwell-membranes directly to the cell grown above. Diffusion was quantified by measuring transient motion of oxygen through the membranes to a sensor spot [2]. Multiple membrane materials were tested. Nutrient supply was tested in a batch media change of various bioreactor designs. The resident time distribution [3] was evaluated using a pulse input of a tracer, Methlyene Blue. Both experimental tests were simulated in ANSYS Fluent. Aggregation protocols of insulinoma cell lines (INS1) and human embryonic stem cell (hESCs) differentiation were used to confirm the preservation of performance between the well plates and the bioreactor.

Results

The oxygen diffusion was found to be sufficient for cell growth in one polymer tested, which had an oxygen diffusion 2.3 times better than the polystyrene standard. A bioreactor layer design was generated by minimizing the resident time's scaled variance which improved with lower media flow, larger layer height and more inlet/ outlet ports. The scaled variance ranged from 0.50 to 0.22. Aggregation protocols were preserved using INS1 and hESCS by evaluating metabolism and differentiation success respectively.

Conclusions

The use of microwell well-plates provides a high throughput platform to test aggregate performance and generation however scaling up these protocols is a challenge. The microwell bioreactor provides an immediate solution to scaling up microtissue production to clinically relevant number while maintaining existing protocols.

References

1. Yanai et al, Mehtods Mol Biol, 2016, 357-69
2. Markov et al, Biomed Microdevices, 2015, 91-6
3. Egger et al, Bioengineering, 2017, 51

Figures

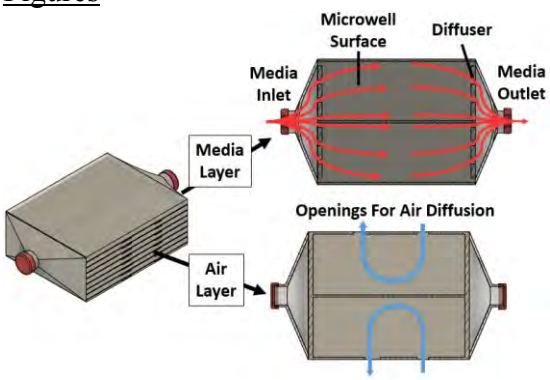

Figure 1: Proposed Microwell Bioreactor Layered Design

Validating a new HR-pQCT-based method for predicting failure load of the distal radius

Adrian K. Teare[1], Seyedmahdi Hosseinitabatabaei[2], Amy T. Bunyamin[1], Saija A. Kontulainen[3], James D. Johnston[1,2]
[1] Department of Mechanical Engineering, [2] Division of Biomedical Engineering,
[3] College of Kinesiology, University of Saskatchewan, Saskatoon, SK, Canada

Introduction

High-resolution peripheral quantitative computed tomography (HR-pQCT) is a non-invasive tool used to image and characterize bone properties of the distal radius, such as cortical and trabecular area and density. HR-pQCT, combined with finite element (FE) modeling, has also been used to estimate failure load of the distal radius. These measures are useful for studying bone's resistance to loading (failure load) in people with osteoporosis, who are prone to fracture.

FE analyses require advanced knowledge and expertise. Given that HR-pQCT provides cortical and trabecular area and density measures, it may be possible to combine these measures with engineering-based composite theory to derive a simple index capable of predicting failure load of the distal radius.

Our objective was to assess variance in failure load predicted by a new HR-pQCT-based index (referred to as F_{HR}) along with FE-estimates and other bone properties.

Methods

Specimens: We evaluated 14 fresh-frozen cadaver forearms, all from female donors (mean age 83.7, SD 8.3 years).

Imaging: We scanned the distal radius using HR-pQCT (Scanco Medical) with the standard clinical protocol (82 μm voxel size).

Mechanical Testing: Forearms were tested in axial compression using a material testing system (MTS Bionix). Testing was performed at 3mm/s onto the palm of the hand until failure. Failure loads were recorded.

Image & FE Analysis: Cortical and trabecular area (A) and bone mineral density (BMD) were analyzed from HR-pQCT images. FE predictions of failure load (F_{FE}) were acquired using the single tissue model. Pistoia's strain-based failure criteria was employed [1].

F_{HR} Analysis: Composite theory was used to account for relative effects of cortical and trabecular bone when resisting load. We assumed that cortical and trabecular bone act as springs-in-parallel and are subjected to the same strain during loading. We also assumed that failure would occur first in trabecular bone. F_{HR} (the force needed for trabecular bone to fail) was calculated using the following equation:

$$F_{HR} = \frac{(S_{trab})[E_{trab}\,A_{trab} + E_{cort}\,A_{cort}]}{E_{trab}}$$

where:

- $S_{trab} = 70.4\rho^{1.60}$ (MPa), defines trabecular ultimate compressive strength [2];
- $E_{trab} = 18.7\rho^{1.83}$ (GPa), defines trabecular bone elastic modulus [3];
- $E_{cort} = 10.3\rho^{2.39}$ (GPa), defines cortical bone elastic modulus [4];
- ρ pertains to trabecular or cortical BMD (g/cm^3) acquired using HR-pQCT (which we regard as being equivalent to ash density [5]).

Statistics: Linear regression was used to assess bone properties, FE predictions, and the new F_{HR} index in predicting variance (coefficient of determination, R^2) in experimental failure load.

Results

Variance in failure load appeared to be best predicted by F_{HR} (76%), F_{FE} (72%), and cortical area (59%) (Table 1).

Table 1: Coefficient of Determination (R^2) Predicting Experimental Failure Load

Predictor	R^2
Trabecular Area (A_{trab})	0.01
Trabecular BMD	0.45
Cortical Area (A_{cort})	0.59
Cortical BMD	0.55
F_{FE}	0.72
F_{HR}	0.76

Conclusions

The simple F_{HR} metric explained similar variance in experimental failure load to the more advanced FE method. F_{HR} may be a valuable tool in evaluating bone failure load at the distal radius and may be used as an alternate tool in predicting fracture risk.

References

[1] Pistoia et al., 2002; [2] Hvid et al., 1989
[3] Morgan et al., 2003 [4] Snyder & Schneider, 1991
[5] Nazarian et al., 2008

Dual regression analysis of resting state fMRI in IBD patients

Faranak Heidari, Gilaad Kaplan, Mark Swain, Bradley Goodyear
Biomedical Engineering Program, Depts of Radiology and Medicine, University of Calgary, AB, Canada

Introduction

Inflammatory bowel disease (IBD) is a painful and chronic immune-mediated inflammatory disease of the gut. IBD patients also experience other symptoms such as fatigue, mood disorders and cognitive deficits [1]. Animal models of IBD have demonstrated changes in the brain, in relation to the inflammatory state [2]. It remains unknown whether IBD leads to the disruption of brain functional networks associated with symptoms commonly experienced by IBD patients. In this study, we used dual regression analysis of resting-state functional magnetic resonance imaging (fMRI) data [3] to identifiy functional brain networks that are altered in IBD patients relative to healthy controls.

Methods

Sixteen newly-diagnosed IBD patients and 16 age and sex matched controls underwent resting-state fMRI. Images were collected using a 3 Tesla MR scanner (Discovery MR750; GE Healthcare, Waukesha, WI) located in Seaman Family MR Centre. All images were processed and analyzed using *FSL* software [4]. After standard pre-processing steps of skull stripping, slice timing correction, motion correction, spatial smoothing and low-pass temporal filtering, images were registered to the MNI standard space brain template. Time-varying fMRI signals caused by artifact were identified by Independent Component Analysis (ICA) and subsequently removed by regression [4]. The first step of dual regression analysis consisted of obtaining the mean time-varying signal from one of 21 known atlas-based functional networks [5]. This signal was used in a General Linear Model (GLM) analysis to determine brain regions synchronized with the mean network signal. A between-group GLM analysis was then performed to determine brain regions that significantly differed between IBD patients and controls in terms of their strength of connection (connectivity) with the functional network. Maps of differential connectivity were thresholded at a corrected p value of 0.05, using the nonparametric permutation tool of FSL. This process was repeated for the remaining 20 networks.

Results

Connectivity was altered in IBD patients in a number of functional networks, including the motor, executive function and default mode networks. As an example, Figure 1 shows the motor network (in red) and regions differentially connected to the motor network in IBD patients relative to controls (in blue). Regions include the cerebellum and regions of the brainstem. Altered connectivity of the motor network may be associated with fatigue commonly experienced by IBD patients; future correlation analyses with symptom scores are planned.

Conclusions

These preliminary results demonstrate that dual regression analysis of resting-state fMRI data can successfully determine the changes in brain functional connections associated with IBD. Futher analyses will lead to a better understanding of brain mechanisms underlying IBD-related symptoms, and will aid in the development of behavior-targeted therapies.

References

1. NA Molodecky et al., *Gastroenterology* 142: 46–54 (2012).
2. P Bercik, *Neurogastroenterology and Motility* 24: 405-413 (2012).
3. C.F. Beckmann, et al., *OHBM*, (2009).
4. M Jenkinson et al., *NeuroImage* 62: 782-90 (2012).
5. S.M. Smith, et al., PNAS 109: 3131-6 (2012).

Figures

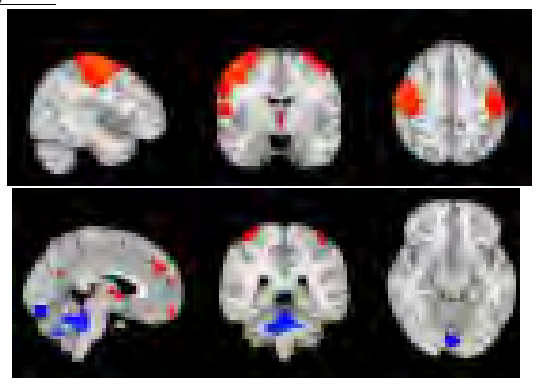

Figure 1. The motor functional network (in red). IBD patients exhibited decreased connectivity between the motor network and the cerebellum and brainstem (in blue), relative to control subjects.

Oxygen Tension Modulated *In Vitro* Chondrogenesis of Infrapatellar Fat Pad-Derived Mesenchymal Stem Cells through Differential Proliferation

Samia Rahman, Alexander Szojka, Colleen Moore, Melanie Kunze, Aillette Mulet-Sierra, Nadr M. Jomha, and Adetola B. Adesida
Department of Surgery, University of Alberta, Edmonton AB

Introduction: Infrapatellar fat pad-derived mesenchymal stem cells (IFP-MSCs) are a promising cell source for cartilaginous tissue engineering. Chondrogenesis of Bone Marrow-derived MSCs (BM-MSCs) through transforming growth factor β3 (TGFβ3) supplementation poses a risk for bone formation through induction of hypertrophic differentiation[1]. Our research has shown that hypoxic chondrogenic culture can suppress hypertrophic differentiation of BM-MSCs induced by TGFβ3[2]. Another study has shown that hypoxic culture of BM-MSCs induced chondrogenesis without the need for TGFβ3[3]. We thus investigated the potential use of hypoxia (HYP) without exogenous TGFβ3 supplementation to drive chondrogenesis of IFP-MSCs.

We hypothesized that HYP (2% O_2) culture of IFP-MSCs in the absence of TGFβ3 may induce chondrogenesis.

Methods: IFP-MSCs from the infrapatellar fat pad of four human donors (age range: 21-55) were expanded to passage 2 with 5 ng/mL fibroblast growth factor-2 under normoxia (NRX, 20% O_2) and were then cultured in a cell aggregate/pellet model for three weeks. During this three-week culture period the conditions were HYP (2% O_2) or NRX, with and without TGFβ3. We characterized the tissue formed in terms of its gross morphology, histologically for proteoglycan distribution in the extracellular matrix (ECM), and biochemically for glycosaminoglycans (GAGs) and DNA content.

Results: Groups supplemented with TGFβ3 showed enhanced proteoglycan staining relative to -TGFβ3 groups under both oxygen tensions. Among -TGFβ3 groups, proteoglycan staining showed indications of IFP-MSC chondro-genesis under HYP, and surprisingly NRX as well. The GAG vs. DNA scatterplot revealed that NRX groups had increased DNA regardless of TGFβ3 supplementation. Among samples with TGFβ3, both oxygen tensions showed similar GAG/DNA ratios; in contrast, this ratio was elevated in HYP relative to NRX without TGFβ3.

Conclusion: Taken together, these findings suggest that oxygen tension may modulate chondrogenesis of IFP-MSCs through a proliferation-related mechanism.

Acknowledgements: Thank you to Brayden D. Lyons and Yan Liang for helping to carry out this study. Thank you to the University of Alberta Department of Surgery Summer Studentship for funding support.

References:

1. Pelttari K *et al.* 2006. *Arthritis Rheum*
2. Adesida A *et al.* 2012. *Stem Cell Res Ther*
3. Marsano A *et al.* 2016. *Stem Cells Transl Med.*

Figure:

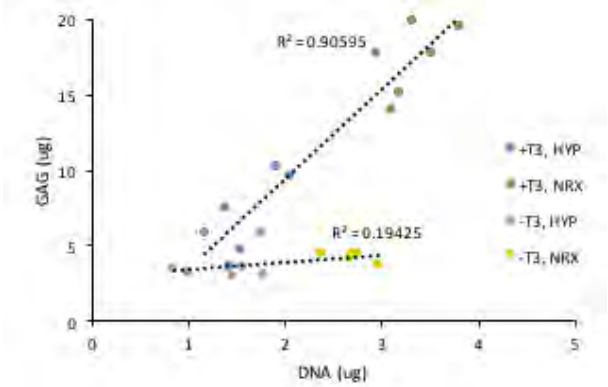

Fig.1: GAG vs. DNA for NRX and pure HYP. 2 replicates per donor, per condition. T3: TGFβ3.

Defining monitoring time intervals for high-resolution peripheral quantitative computed tomography-based cortical bone properties in children

Bunyamin AB[1]; Kawalilak CE[1]; Björkman KM[2]; Johnston JD[1]; Kontulainen SA[2]
[1] Department of Mechanical Engineering, University of Saskatchewan, Saskatoon, SK
[2] College of Kinesiology, University of Saskatchewan, Saskatoon, SK

Introduction:

Cortical bone growth and development during childhood is important because cortical bone properties at distal bone ends (e.g., thickness, density, porosity) are major determinants of fracture risk in childhood, adolescence and later life [1-4]. High-resolution peripheral quantitative computed tomography (HR-pQCT) can non-invasively measure bone micro-architecture in children [5,6]; however, the time needed between HR-pQCT scans for reliable monitoring of growth and development in cortical bone properties is unknown. This time period can be estimated by calculating monitoring time intervals (MTIs), which are based on the ratio between precision errors defined using the least significant change (LSC) and median annual change [7]. LSC is a conservative quantitative metric that ensures measured values are beyond measurement precision errors.

The objective of this study was to estimate MTIs required to reliably capture growth and development in cortical bone properties at the distal radius and tibia of children.

Methods:

To assess median annual change, we obtained baseline and follow-up scans of the distal radius (7% ulnar length site) and tibia (8% site) of 38 children (22 girls). Participant mean age was 10.6 (SD 1.7) years at baseline. Follow-up scans were obtained by the same technician, on average, 1.2 (SD 0.2) years later. We first normalized individual change to 1-year change and then quantified median annual change for each bone outcome. We used previously reported LSC values [5] and divided them by the normalized median annual change to estimate MTIs. We estimated MTIs for the following cortical bone properties: total and cortical area; bone and tissue mineral density; total, bone, and pore volume; apparent thickness, fine-structured thickness, and porosity.

Results:

At the distal radius, MTIs for pediatric cortical bone properties ranged between 0.8-5.7 years. Longer MTIs (>3 years) pertained to total area, cortical area and total volume. Shorter MTIs (~1 year) pertained to bone mineral density, bone volume, fine-structured cortical thickness, and cortical porosity.

At the distal tibia, MTIs ranged between 0.5-2.3 years. Longer MTIs (>2 years) pertained to cortical pore volume and apparent cortical thickness. Shorter MTIs (<1 year) pertained to total area, bone mineral density, tissue mineral density, bone volume, and cortical porosity.

Conclusions:

This study is the first to report MTIs for HR-pQCT cortical bone properties in children. Our findings indicate that annual HR-pQCT measurements can reliably monitor growth and development in cortical bone density and micro-architecture, such as cortical porosity, at the distal radius and tibia in children. These findings also guide selection of primary outcomes in prospective pediatric HR-pQCT studies. Reported MTIs will also help avoid too frequent follow-up scans and minimize related radiation exposure in prospective studies, which is particularly important for the growing skeleton.

References

[1] McCalden et al., 1993
[2] Farr et al., 2014
[3] Shanbhogue et al., 2016
[4] Bjørnerem et al., 2013
[5] Kawalilak, **Bunyamin**, et al., 2017
[6] Gabel et al., 2017
[7] Glüer et al., 1999

Effects of Culture Duration and Medium on the Mesenchymal Stem Cell Secretome

Jolene A. Phelps, Jane Maynard, Amir Sanati-Nehzad, Neil Duncan, Arindom Sen
University of Calgary, Calgary, Alberta T2N 1N4

Introduction

There is evidence to suggest that many of the therapeutic effects of mesenchymal stem cells (MSCs) can be attributed to the collection of biomolecules they secrete (i.e. their secretome)[1]. Recent studies have provided evidence that similar effects may be produced by using only the secretome fraction that contains extracellular vesicles (EVs)[1]. EVs are membrane-bound vesicles that contain biomolecules such as growth factors and RNAs, and provide a stable delivery system to transfer these biological signals throughout an organism. There are 3 types of EVs: apoptotic bodies, microvesicles and exosomes. The exosome fraction has been considered the most promising therapeutic of all EVs[1].

The use of the MSC secretome and/or its derivatives presents advantages over the implantation of cells: (i) the secretome, including EVs, can be bioengineered for quality control and scaled to specific dosages, and (ii) the non-living nature of the secretome means it can be stored and transported relatively easily compared to cells. The MSC secretome is a dynamic system, and thus, the amounts and types of molecules secreted will depend on the protocols used to culture the cells[2]. This study examined how exosome and biomolecule concentration was affected by medium and time in culture. This research is pertinent to the development of a bioprocess tailored towards the production of MSC secretome-derived factors for their use as cell-free therapeutics.

Methods

Ethically approved human adipose tissue-derived MSCs were cultured in serum-free PPRF-msc6 medium at 37°C and 5% CO_2. A full medium change was performed on day 3 with either PPRF-msc6 (high growth medium) or DMEM (low growth medium). Growth curves for each of the different conditions were generated.

Expended medium was collected from day 3 and day 6 of each culture and centrifuged at 2000 g for 10 min to remove pelleted apoptotic bodies. To collect the secretome, the supernatant was centrifuged at 4000 g for 60 min in 3 kDa Amicon Centrifugal Filters and the concentrated supernatant was collected. To create the EV fraction, the supernatant was ultra-centrifuged at 100,000 g for 2 h, and the EV pellet was re-suspended in PBS.

EVs were sized by nanoparticle tracking analysis using Nanosight. The concentration of exosomes was measured via ELISA for CD81, a known marker for exosomes. Biomolecule analysis for known angiogenic factors was performed by Eve Technologies.

Results

The overall quantity of exosomes was highest in the secretome obtained from day 6 cultures grown in PPRF-msc6 as the number of cells was significantly higher. The average number secreted per cell was highest on day 6 in DMEM (Figure 1). The average number of exosomes secreted per cell grown in PPRF-msc6 did not significantly change per passage, but was reduced with increasing cell confluence (day 3 vs. day 6). Endoglin was higher in the EV fractions indicating enhanced stability within EVs. On a per cell basis, IL-8, G-CSF*, HGF*, VEGF*, follistatin and FGF-2 were highest in the samples taken from day 6 cultures grown in DMEM (*Figure 2).

Conclusions

On a per cell basis, cells secrete more exosomes and therapeutic factors when cultured in DMEM. As such, it is necessary to design bioprocesses aimed at collecting these factors after switching the culture to a low growth medium such as DMEM, while also taking into account the confluence of the cells.

References

1. Marote A, et al. *Front Pharmacol*. 2016. doi:10.3389/fphar.2016.00231.
2. Ranganath SH, et al. *Cell Stem Cell*. 2012. doi:10.1016/j.stem.2012.02.005.

Figures

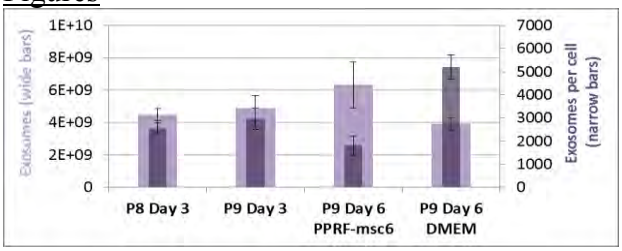

Figure 1: The number of exosomes secreted per cell in different conditions. P8/9 = passage 8/9.

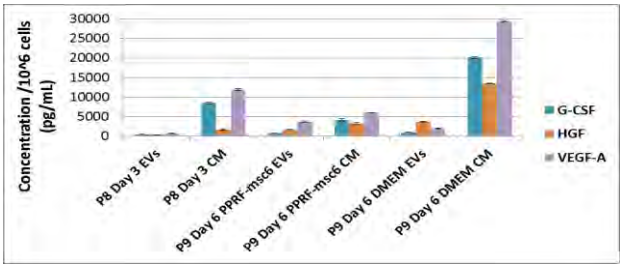

Figure 2: Concentrations of G-CSF, HGF and VEGF-A per 10^6 cells in the concentrated secretome and EV fractions of different conditions

Increased serum levels of CCL22 after exercise may be a marker of cartilage degeneration and pain in individuals with a previous joint injury

Guomin Ren, Jackie L Whittaker, Catherine A Leonard, Carolyn. A. Emery, Roman J. Krawetz
HRIC 3C41, 3330 Hospital Drive NW, Calgary, Alberta, Canada T2N 4N1

Introduction

MRI is able to detect minor structural changes in joint tissues at an early stage of osteoarthritis (OA)[1]. However, the biological processes involved in these changes are still not understood. Few studies have reported a temporary elevation of serum biomarkers after exercise in individuals with clinically diagnosed knee OA[2,3]. But it remains unknown if exercise-induced changes are present at early stages of OA (e.g. MRI-defined OA). The aims of this study were to 1. Evaluate the association between serum cytokine levels before and after exercise with pain and MRI sub-scores in a human cohort that suffered a previous joint injury (but without clinically diagnosed OA).
2. To validate the existence of identified cytokine(s) at the initial stage of the disease in a rat model of OA.

Methods

Patients: The analyses included a sub-sample of 145 from the Alberta PrE-OA cohort for whom 1st-year follow-up serum cytokine and clinical MRI were both studies completed. The blood samples were taken when rested and after 30-minutes exercise. Bone marrow lesion (BML), cartilage, meniscus, ligament and synovitis in both injured and non-injured knees were evaluated using MRI OA scores (MOAKS). Animal model: Standardized joint injuries (destabilization of the medial meniscus, DMM) were induced on the left knee joints of rats (N = 18). Nine were used for repeated serum cytokine analysis, the rest were sacrificed at different time after injury (7-time points: before and 3, 5, 10, 14, 20, 24 days after injury) for histology and immunohistochemistry (IHC) study. Inflammatory profiles (include 41 cytokine concentrations) in human and rat serum samples were analyzed using the Human Cytokine Panel (Millipore) and Milliplex MAP Rat Cytokine/Chemokine Array 23 Plex, respectively, on a Luminex platform.

Results

In the human cohort, no cytokine from pre- or post-exercise alone was found correlated with pain scores. The changes of CCL22 between pre- and post-exercise was correlated with both KOOS pain score (r=0.175, p=0.38), ICOAP overall score (r=-0.176, p=0.37) and MRI synovitis score (r=0.168, p=0.047).
In rat model, CCL22 was correlated with significant cartilage degeneration width (r=0.9, p=0.001) and surface matrix loss (r=0.767, p=0.016). CCL22 were detected in the cartilage or/and synovium in all joints (n=12) with visible damage (total degeneration width > 0 um). CCL22 was also found correlated with pain (r=0.25, p=0.048) in the rat model. In injured joints without cartilage degeneration, osteophytes or synovial inflammation, CCL22 were present in 3 out of 6 joints. By comparing the histology and IHC staining of adjacent slides in joints with DMM injury, CCL22 was found to be present in the areas even without visible damage (Figure 1).

Conclusions

We have shown that the increase of CCL22 after exercise, but not the resting level, was correlated with pain and MRI synovitis score in a joint injury cohort. In an OA rat model, CCL22 was detected in joints at initiation stage of joint degeneration when there was still no visible damage. These results suggest that exercise-induced increment of CCL22 might be potential biomarkers for detecting early deterioration of the joint. Future studies are needed to identify the biological role of CCL22 in the progression of joint degeneration.

References

1.Ding, C. *et al. Nat Clin Pract Rheumatol* **4**, 4-5 (2008).
2.Lems, W.F. *et al. Arthritis Res Ther.* (2010).
3.Andersson,M.L.*et al. BMC musculoskelet disord* 2006.

Figures

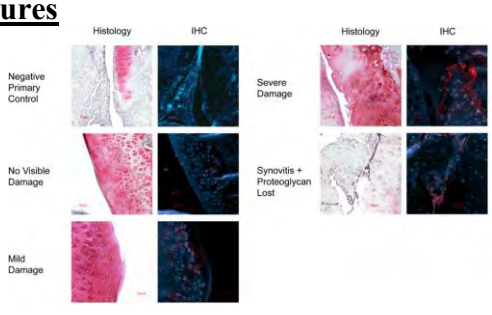

Transforming growth factor and hypoxia signaling regulate meniscus-like extracellular matrix production by human meniscus cells

Alexander Szojka, Brayden D. Lyons, Colleen Moore, Yan Liang, Melanie Kunze, Enaam Idrees, Aillette Mulet-Sierra, Nadr M. Jomha, Adetola B. Adesida
Department of Surgery, University of Alberta, Edmonton AB

Introduction: Meniscus fibrochondrocytes (MFCs) are a promising cell source for tissue engineering the non-healing inner meniscus regions. MFCs can be isolated and expanded *in vitro* from damaged meniscus tissue removed during arthroscopic surgery. They can then be induced by exogenously-supplemented transforming growth factor β3 (TGFβ3) to produce extracellular matrix (ECM) like the inner meniscus, rich in type II collagen and proteoglycans[1].

In the knee, the menisci experience a hypoxic (HYP) environment with 1-7% oxygen tension[2]. We showed that MFCs respond to HYP (3%) with enhanced ECM formation in the presence of TGFβ3[1]. As well, HYP alone (2%) can stimulate bone marrow-derived mesenchymal stem cells to undergo chondrogenesis[2]. Thus, we investigated the use of HYP to induce meniscus-like ECM formation by MFCs without added TGFβ3.

Methods: MFCs were isolated from five human donors undergoing partial meniscectomy. MFCs were expanded using TGFβ1 and fibroblast growth factor-2 to 3.4±0.4 population doublings under normoxia (NRX, 21% O_2), as described[1]. Using a cell pellet model (5×10^5 MFCs each), the samples were cultured for three weeks under NRX or HYP (3% O_2), with and without 10 ng/mL TGFβ3. Pellets were assessed quantitatively for meniscus-like ECM formation by measuring gene expression and total glycosaminoglycan (GAG) and DNA content and qualitatively for proteoglycans and collagen I/II. Hypoxic regions in pellets were visualized by immunofluorescence using the Hypoxyprobe kit. One-way ANOVA with blocking was performed with Tukey's post-hoc test to assess differences between groups.

Results: Low gene and protein expression of chondrogenic markers were observed in groups without TGFβ3. Combined HYP and TGFβ3 had increased SOX9 expression and GAG/DNA over all other groups (Fig.1). All groups showed type I collagen, but type II collagen was only observed in groups with TGFβ3 and was more abundant under HYP. The Hypoxyprobe marker appeared ubiquitously in HYP pellets. Interestingly, it also appeared internally in NRX pellets, indicating regional hypoxic regions. For the NRX group with TGFβ3, this corresponded to intense internal proteoglycan staining within a fibrous-looking capsule.

Conclusion: In this study, meniscus-like ECM formation was shown to be enhanced by 3% HYP but only in the presence of TGFβ3. Colocalization of the Hypoxyprobe marker and proteoglycan-rich ECM in the interior regions of NRX-cultured pellets with TGFβ3 indicates that HYP is a regulator of meniscus-like ECM formation by MFCs.

Figures:

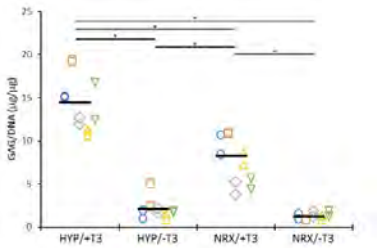

Fig. 1: GAG/DNA for MFC pellets. T3: TGFβ3. Shapes show separate donors while duplications show technical replicates. *: $p<0.01$.

References: [1]: Liang Y *et al*. 2017. Scientific Reports, *in press*. [2]: Lund-Olesen, K. 1970. Arthritis & Rheumatology. [3]: Marsano A *et al*. 2016. Stem Cells Translational Medicine.

Quantifying the Effect of Shear Stress on Murine Embryonic Stem Cell Aggregates

Alexander A. Wyma[1,3], Breanna Borys[1,3], Tania So[1], Michael S. Kallos[1,2,3]
[1]Pharmaceutical Production Research Facility, [2]Department of Chemical and Petroleum Engineering, [3]Biomedical Engineering Graduate Program, University of Calgary, 2500 University Dr. NW, Calgary, AB, T2N 1N4

Introduction

To optimize cellular growth kinetics and proliferation multicellular aggregates are often cultured in stirred suspension bioreactors [1]. Typically, the effect of agitation in stirred suspension bioreactors is quantified in terms of impeller speed [2]. However, the impact of impeller speed on cell aggregates is only valid for specific bioreactor geometries, and does not provide meaningful insight for bioprocess scale up. This study examines the effect of a geometry independent measure of agitation, shear stress, on murine embryonic stem cell (mESC) aggregate characteristics to serve as an alternative scalable measure of agitation.

Methods

mESCs were cultured in 100mL bioreactors at 60 and 120 RPM over a four day period. Trypan blue exclusion cell counts at 24 hour intervals were used to create a growth curve and measure cell growth kinetics in terms of exponential growth rate and fold expansion. Light microscope images of bioreactor cultures at each time point were captured to measure aggregate diameter distributions. A box counting method was applied to these photos to obtain the planar fractal dimension. Fractal dimensions were used to measure morphological change as fractal dimension describes the arrangement of cells within an aggregate. Computational fluid dynamics (CFD) simulations of a 100mL stirred suspension bioreactor were performed in ANSYS Fluent to calculate steady state values of volume average and maximum shear stress.

Results

Cell kinetics for bioreactor cultures at 60 and 120 RPM exhibited different exponential growth rates of 4.61×10^{-3} and 4.93×10^{-3} h^{-1} respectively. Both cultures had the same lag time (24 hours), but exhibited significantly different fold expansions of 15 and 39 at 60 and 120 RPM respectively. Average aggregate diameters increased daily and were significantly larger for the 60 RPM culture in comparison to the 120 RPM culture (Figure 1). The fractal dimension of studied aggregates increased independently of impeller speed from 1.605 on day one to 1.867 on day four. Both maximum and volume average shear stress values determined using CFD increased linearly relative to the change in impeller speed between bioreactor cultures.

Conclusions

The results of this study indicate that shear stress plays an important role in regulating the growth rate, fold expansion, and aggregate diameter of mESCs. The effect of shear stress on shear dependent aggregate characteristics scaled in a highly non-linear manner. Due to the large degree of non-linearity, small changes in bioreactor geometry impacting shear stress will have a correspondingly large effect on aggregate size and growth kinetics. Such changes in geometry are often encountered during bioprocess scale up. Thus, shear stress may provide a geometry independent method for multicellular aggregate bioprocess scale up.

References

[1] Gareau, T., et al. Journal of Tissue Engineering and Regenerative Medicine 2014; 8(4): 268–78
[2] Olmer, R., et al. Tissue Engineering: Part C 2012; 18(10): 772–84

Figure

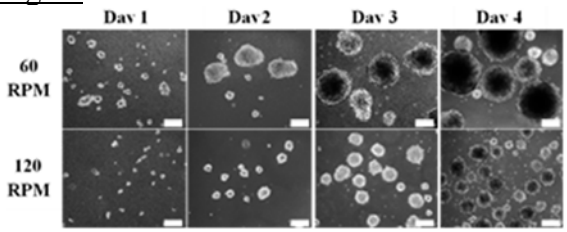

Figure 1: Light microscope images of mESC aggregates cultured in stirred suspension bioreactors at 60 and 120 RPM impeller speeds. Aggregates cultured at 60 RPM exhibited significantly larger diameters in comparison to those cultured at 120 RPM at the same time point. Scale bar represents a length of 200um.

Correlation between translational and rotational kinematic instabilities and osteoarthritis development in an in vivo ovine model of ACL injury.

Mehdi Shekarforoush, Kristen I Barton, Bryan J Heard, C Ryan Martin, David A Hart, Nigel G Shrive
McCaig Institute for Bone & Joint Health, Cumming School of Medicine, University of Calgary, Calgary, AB,

Introduction

Joint injury dramatically increases the risk of osteoarthritis (OA). There is a consensus that alteration of joint kinematics is a key factor in the development of osteoarthritis after joint injury. Although alterations to joint kinematics after injury have been generally established, the relationships between such kinematic instabilities and long-term OA development have not been clearly established. The first objective of this study was to investigate the translational and rotational instabilities of the knee joint after partial transection of the Anterior Cruciate Ligament (ACL) (p-ACL Tx) in a sheep model (just the Antero-Medial band of the ACL was transected). The second objective was to investigate correlations between changes in the kinematics and the gross morphological damage observed in the joint (related to initiation of OA) after injury. We hypothesized that after p-ACL Tx, that there would be both translational and rotational kinematic instabilities in the joints and these instabilities would be correlated to the gross morphological damages in the subjects.

Methods

Five skeletally mature, 3 to 5-year-old female Suffolk-cross sheep were used for this study (n=5). The animals were trained to walk on a treadmill at 2 mph for data recording. The stifle joint kinematics were measured in over 200 strides with an instrumented spatial linkage (ISL). After defining the normal (intact) kinematics of the joints, surgical interventions were performed on the subjects through arthroscopic surgery and the joint kinematics were measured again at 20 and 40 weeks after injury. After euthanization, both the right (surgical) and left (nonsurgical) stifle joints were graded for gross morphological cartilage score (GCS) (Drez et al., 1991) and the score for an animal was expressed as the difference of the surgical from the non-surgical scores (ΔGCS). The rotational instability of the joint was defined as the spatial angular change of the axes of rotations from intact after injury, and the translational instability of the joint was defined as the absolute change of distance between the coordinate systems attached to the bones. These variables were defined at six points through the gait cycle. The non-parametric Spearman's correlation test was used for correlation analyses.

Results

The partial ACL transection did lead to gross cartilage damage in the subjects. Both rotational and translational kinematic alterations were detected as early as 20 weeks after injury. There were linear correlations between the change of axes of rotation and ΔGCS at 2/6 points analyzed and linear correlations between the absolute translational change and ΔGCS at 5/6 points analyzed through the gait cycle, with significant level of difference ($0.03<\alpha<0.1$). Interestingly, the quantifications of these parameters at the early time point (20 weeks post injury) were not correlated to the ΔGCS at the later time point (40 weeks).

Conclusions

The correlation analyses suggest that generally, translational instabilities were more critical than rotational instabilities for the progression of OA after ACL injury. The reason may be a consequence of kinematic changes on the stress distributions across the articulated surfaces [2], or the change of relative surface velocity directions that define the frictional force distribution [3]. In contrast to our expectation, the most interesting finding was that early kinematic instabilities at the first measurement points were not consistently correlated with the gross morphological cartilage damage at the more advanced later time point.

References

1. The American journal of sports medicine, 19(3), 256–63.
2. Annals of biomedical engineering, 32(3), 447–57.
3. J Orthop Res. 2017 Mar;35(3):454-465.

Cortical porosity assessment in the radius through comparison with synchrotron-based measures

Soltan N[1], Kawalilak CE[1], Cooper DML[2], Kontulainen SA[3], Johnston JD[1]
[1]Department of Mechanical Engineering, [2]Department of Anatomy & Cellular Biology, [3]College of Kinesiology
University of Saskatchewan, Saskatoon, SK, Canada

Introduction

Cortical porosity (Ct.Po) is an important micro-architectural indicator of bone loss, fragility and the onset of osteoporosis [1,2]. Accurate Ct.Po assessment may complement assessment of fracture risk [1,2]. High-resolution peripheral quantitative computed tomography (HR-pQCT) is an *in vivo* imaging tool that quantifies Ct.Po using standard threshold-based segmentation and more recently, bone density [3]. Synchrotron radiation micro-computed tomography (SR-μCT) is an *ex vivo* imaging tool that is considered to be the gold standard in cortical bone analysis [4]. Previous studies have compared HR-pQCT derived Ct.Po with SR-μCT derived Ct.Po at small and isolated tibia samples [3,5]; however, studies have not yet assessed the distal radius; one of the most common fracture sites in postmenopausal women [6].

The objectives for this study were to: 1) determine the agreement between HR-pQCT-derived Ct.Po (standard threshold and density methods) and SR-μCT-derived Ct.Po at the distal radius; and 2) identify the segmentation threshold that optimizes the agreement between HR-pQCT derived Ct.Po and SR-μCT derived Ct.Po.

Methods

Ten cadaveric radii (mean age: 79 ± 11 years) were scanned at the distal standard clinical region using HR-pQCT and SR-μCT at an isotropic resolution of 82μm and 17.7μm, respectively. Common proximal slices in the standard scan site were visually identified in both imaging modalities. To obtain comparable regions for analysis, cortical regions were delineated for each specimen using a derived "peel level" (number of voxels radially inwards from the periosteal contour). The "peel levels" for each specimen were derived by finding the "peel" thickness which had the closest Ct.Po to Ct.Po acquired from the semi-manual segmentation of cortical bone from HR-pQCT images. The delineated cortical bone in both imaging modalities was analyzed for Ct.Po. The HR-pQCT images were analysed for Ct.Po using the threshold method (with the manufacturer prescribed standard threshold of 400 mgHA/cm^3, as well as thresholds ranging from 400 to 900 mgHA/cm^3) and the density method [3]. The SR-μCT images were analysed using the threshold method (threshold of 750 mgHA/cm^3 [3]). The agreement between HR-pQCT Ct.Po (threshold and density methods) and SR-μCT Ct.Po was evaluated using linear regression and Bland-Altman plots.

Results

The standard HR-pQCT threshold method explained 85% of the variance in SR-μCT-derived Ct.Po while the density method explained 89% of the variance. Bland-Altman plots indicated that the threshold method appeared to underestimate Ct.Po while the density method appeared to overestimate Ct.Po. An HR-pQCT threshold of 600 mgHA/cm^3 explained 91% of the variance in SR-μCT-derived Ct.Po.

Conclusions

HR-pQCT-derived Ct.Po measures at the distal radius were in good agreement with Ct.Po obtained with gold standard SR-μCT. These findings can be used to guide future HR-pQCT research striving to more accurately quantify bone degeneration and evaluate the efficacy of preventative and treatment methods for osteoporosis.

References

[1] Cooper et al., 2016; [2] Burghardt et al., 2010;
[3] Jorgenson et al., 2014; [4] Carter et al., 2012;
[5] Ostertag et al., 2014; [6] Tjong et al., 2012

Validity of Vertical Oscillation Measures Using a Markerless Motion Capture System

Ashley Johnston, Dylan Kobsar, Sean Osis, Russell Kohrs, Reed Ferber
University of Calgary, Faculty of Kinesiology, Calgary, AB

Introduction

Conventional marker-based three-dimensional (3D) gait analysis is the current gold standard in assessing running biomechanics. The precise placement of reflective markers on anatomical landmarks allows for the highly accurate measurement of lower limb and/or centre of mass (CoM) movement that can be useful in both a research and clinical setting. Unfortunately, collecting gait biomechanics with these systems are both expensive and time consuming, making their clinical accessibility limited. Alternatively, the use of markerless 3D motion capture technology (e.g., LiDAR camera) can provide a faster, more affordable, and therefore a more clinically accessible alternative. However, there are limited studies investigating the validity of markerless motion capture data [1]. Therefore, the purpose of this study was to validate CoM vertical oscillations (VO) from markerless motion capture technology compared to a conventional marker-based system.

Methods

Sixteen participants of differing running experience (9F, 7M; age: 29(9) years; height: 169.6(8.3) cm; mass: 65.4(11.5) kg) were outfitted with a pelvic marker cluster, in line with the posterior superior iliac spine, and wore standard laboratory shoes (Pegasus, Nike, Beaverton, USA). Participants ran on an instrumented treadmill (Bertec, Columbus, OH, USA) at 2.7 m/s for 1 minute while a 7-camera motion capture system (Vicon Motion System, Oxford, UK) and a marklerless LiDAR camera (Microsoft Kinect 2.0, Redmond, WA) collected data at 200Hz and 30Hz, respectively. Vicon VO were calculated based on pelvic cluster marker displacement, while Kinect VO was obtained by tracking pelvic point cloud displacement using a pelvic template and an iterative point cloud algorithm. The agreement between the systems was assessed using a two-way mixed intraclass correlation coefficient (ICC) and a Bland-Altman plot with 95% limits of agreement (LOA).

Results

The two systems exhibited similar ranges of VO, but the Kinect underestimated VO by an average of 13mm, compared to the Vicon system. After correcting for this systematic bias, the two systems demonstrated similar measures of VO (mean: Vicon = 90.0(15.9)mm vs. Kinect = 90.0(16.6)mm, range: Vicon = 57.7mm vs. Kinect = 54.2mm). The two systems also demonstrated good agreement (ICC = 0.84; 95% LOA ±17.8mm; see Figure 1).

Conclusion

The Kinect system demonstrated good agreement with the Vicon system for measures of VO during running. While the 95% LOA were ±17.8mm, all but three participants displayed VOs within ±10mm which could indicate multiple models might be needed to account for various body types or running patterns. Nevertheless, the current study remains a successful validation of markerless VO data, thereby suggesting that the Kinect may provide a faster, more affordable and therefore more clinically accessible alternative to conventional marker-based 3D gait analysis.

References

[1] Pfister et al., (2014), Comparative abilities of Microsoft Kinect and Vicon 3D motion capture for gait analysis. J Med Eng Technol. 38(5), 274-280.

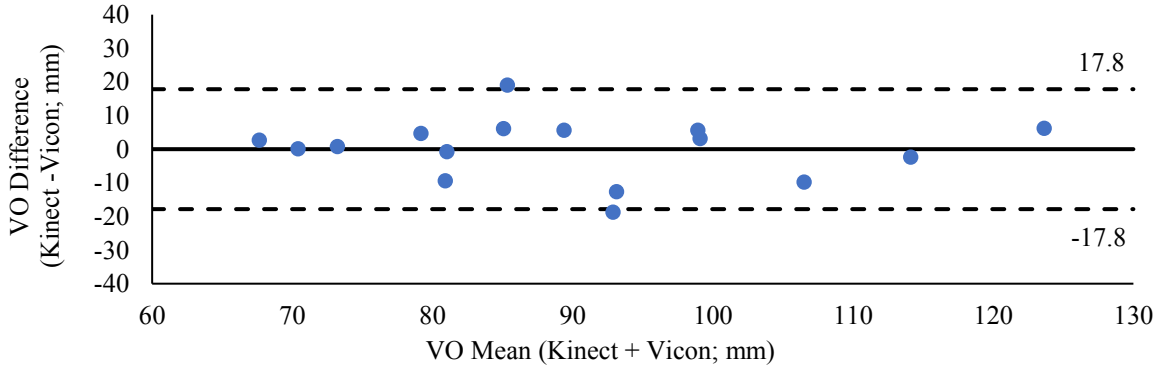

Figure 1: Bland-Altman Points with 95% LOA for Kinect vs Vicon. Abbrev. Vertical Oscillations

EXPERIMENTAL APPROACH TO THE MECHANICS OF AGONIST MUSCLES

Kalvin Wu[1], Seong-won Han[2], Andrew Sawatsky[2], Walter Herzog[2]
[1]Biomedical Engineering Program, University of Calgary, [2]Human Performance Lab, University of Calgary
kalvin.wu@ucalgary.ca

INTRODUCTION

A widely used assumption in biomechanics is that the sum of individual muscle torques is equal to the torque produced when all the muscles are contracted simultaneously. However, previous observation found that the sum of individual torques was greater than the torque produced by a simultaneous contraction. Two speculations on the cause of this torque difference has been suggested: i) that force is transmitted laterally through the connective tissue in agonist muscle groups [1], and ii) that the patellar moment arm length, a value used in muscle force calculations, varies during muscle stimulation.

The purpose of this study was to investigate whether the loss of torque in simultaneous compared to individual muscle activation in the quadriceps group is the result of either lateral force transmission or a changing patellar moment arm length.

METHODS

New Zealand white rabbits were used for this experiment (n=2). The individual nerves of the vastus lateralis (VL), rectus femoris (RF) and vastus medialis (VM) were electrically stimulated. Testing was done at various knee joint angles and trials were performed before and after muscle isolation which eliminated the effects of lateral force transmission. The muscle torque and force were measured at the tibia's distal end and in the patellar ligament respectively. Force readings were measured using an implantable force transducer (IFT) and were independent of the patellar moment arm length.

RESULTS & DISCUSSION

The sum of individual torques was greater than the torque generated by a simultaneous contraction for all knee joint angles both before and after isolation of muscles (Figure 1). This suggests that lateral force transmission is not the cause of the torque difference. Similarly, the sum of individual forces measured by the IFT was greater than the force generated by a simultaneous contraction (Figure 1). This suggests that the patellar moment arm length change is also not the cause of the torque difference.

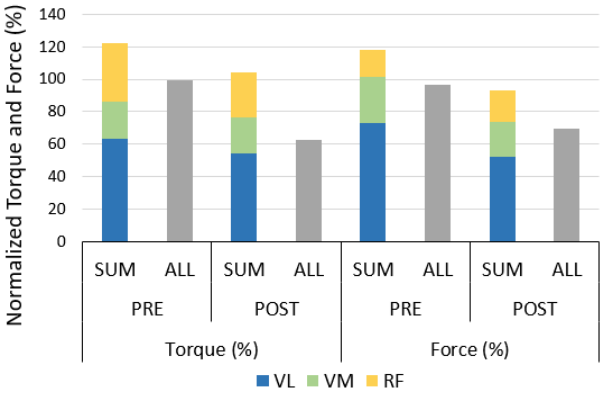

Figure 1: A representative result of this project at one knee joint angle (90 degrees). 100% was defined as the maximum torque/force value when all muscles were stimulated. Sum of individual muscle torques/forces (SUM) and muscle torques/forces of a simultaneous contraction (ALL) are shown before (PRE) and after (POST) isolation of muscles.

CONCLUSION

The loss of torque was not the result of either lateral force transmission or a changing patellar moment arm.

REFERENCES

1. Mass & Sandercock. *J Biomed Biotechnol.* 2010:575672, 2010.
2. Siebert et al. *J Biomech.* 47:1822-1828, 2014.

Extracellular recordings of rat cortical and hippocampal neurons with high signal resolution using novel multi electrode arrays

Simon Wong[1], Pierre Wijdenes[2], Angela Getz[3], Hidekel Mendoza[1,5], Naweed Syed[3,4], Colin Dalton[1,2]
[1]Department of Electrical and Computer Engineering; [2]Biomedical Engineering Graduate Program; [3]Hotchkiss Brain Institute; [4]Alberta Children's Hospital Research Institute, University of Calgary, Canada; [5]Department of Electrical and Computer Engineering, University of Waterloo, Canada.

Introduction

Many neurological disorders, like epilepsy, are the result of dysfunctional neural networks. Unfortunately, our lack of fundamental knowledge in neuroscience prevents clinicians from offering effective treatments, without side effects, to patients with such disorders. In order to develop effective long-term treatments, we must first further characterize how neural networks initially form and how they become dysfunctional. Electrophysiology, through Multi-Electrode Arrays (MEAs), enables the study of neurons at different electrode sites simultaneously for several week periods. However, conventional MEAs have two main issues that prevent such investigation: a lack of required recording stability and/or signal resolution. To address these issues, a new type of MEA was developed with nano-edge features on the microelectrodes [1]. This device was initially applicable only to giant invertebrate neurons (40-80µm diameter), and not mammalian neurons (5-25µm diameter). Based on the same electro-physical properties of the nano-edge MEAs, our group designed and fabricated the multi-well MEA (MW-MEA) to enable the recording of smaller, mammalian neurons at high signal resolutions.

Methods

MW-MEAs were fabricated at the Advanced Micro/Nanosystems Integration Facility (AMIF) at the University of Calgary. Primary rat cortical and hippocampal neurons were cultured in-vitro directly on MW-MEAs micro-electrodes (Fig. 1A). Neural growth and activity were analyzed with reference to their amplitudes and noise level using microscopy and an extracellular recording system.

Results

The MW-MEAs allowed us to record from up to 16 neurons simultaneously for extended periods of time (≥4 weeks), thus allowing the study of neuronal activity propagation across cultured networks. In terms of resolution, we could monitor and record spontaneous activity from mammalian cultured neurons (Fig. 1B) with a significantly higher averaged signal-to-noise ratio (SNR=9.52, n=30, $p<0.05$), and a maximum recorded field potential of up to 450% higher than the best planar MEAs found in literature [2; 3; 4].

In addition, we noticed that the MW-MEAs limit neuronal movement, without damage to the neurons' somas, thanks to the presence of the micro-wells on the electrodes; this improves recording stability.

Conclusion

MW-MEAs demonstrate potential for high resolution and long-term recordings, thus offering novel opportunities to further our understanding of neural network formation, neural plasticity, and neurological disorder.

Several future modifications to the MW-MEA could be made to improve recording resolution. For example, computational simulations have shown that replacing the gold electrodes with other metals or alloys, or using a platinum black coating can increase recording resolution.

References

[1] P. Wijdenes et al. (2016). Sci. Rep., 6(34553)
[2] Y. Nam and B.C. Wheeler (2011). Crit. Rev. Biomed. Eng., 39(1)
[3] H.S. Han et al. (2014). WCE 2014, 1
[4] J. Strickland et al. (2016). J. Nanotoxicology, 10(5)

Figures

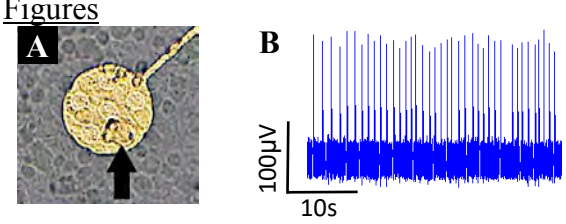

Figure 1. (A) Rat cortical neuron on an electrode micro-well; (B) recorded electrical activity from that neuron.

Methods for Gait Event Detection in Running Using Accelerometer Data

Tessa Exley, Lauren Benson, Ricky Watari, Christian Clermont, Sean Osis, Reed Ferber
University of Calgary, Faculty of Kinesiology, Calgary, AB

Introduction

Portability, affordability, and large storage capacity have made accelerometers useful for measuring running gait parameters in a natural setting.[1] Most gait analysis techniques rely on identifying gait cycles, which can be done by detecting heel-strike (HS) and toe-off (TO) events.[1] If gait event detection algorithms are accurate and automatic, real-time feedback can be provided to the user. Published gait event detection methods using accelerometry often do not provide adequate information to replicate the algorithms, rely on visual inspection, and are typically validated in only in-lab settings. Therefore, the purpose of this study was to validate an accelerometer-based automatic gait event detection algorithm for outdoor running on different surface conditions.

Methods

Part One: Ten participants (7M, 3F; 27.1(3.38) yrs, 1.78(0.06) m, 72.2(7.17) kg) ran on an instrumented treadmill (1000 Hz; Bertec Inc., Columbus, OH) for 1 minute each at 2.7, 3.0 and 3.6 m/s, and data was collected from 3D accelerometers (Shimmer3® +/- 16g, 201.03 Hz; Shimmer Inc., Dublin, IE) affixed to the dorsum of the right foot and low back. The accelerometers were resampled at 1000 Hz and synced with the treadmill force plate kinetic data. HS and TO were identified using force plate (FP), foot accelerometer (FA), and back accelerometer (BA) methods. FP was considered the gold standard and used a threshold of 20N to determine HS and TO. FA determined HS and TO using methods outlined by Strohrmann, et al.[2] BA found HS and TO by identifying peaks in the anterior-posterior accelerometer signal.[3] The number of frames between FA-FP was determined for HS and TO. Additionally, the number of frames between BA-FP and BA-FA were determined for HS and TO. Paired t-tests were used to identify differences between BA-FP and BA-FA for HS and TO, with a Bonferroni-adjusted significance level of $p<0.025$.

Part Two: Ten participants (5M, 5F; 36.3 (13.0) yrs; 1.72 (0.06) m; 69.8 (4.3) kg) ran 625 m each on sidewalk and grass at a self-selected speed with 3D accelerometers placed as in Part One. HS and TO were determined on both sidewalk and grass using FA and BA. The number of frames between BA-FA at HS and TO was determined for both grass and sidewalk conditions. Paired t-tests were used to compare sidewalk and grass differences in BA-FA for HS and TO, with a Bonferroni-adjusted significance level of $p<0.025$.

Results

Part One: The mean (SD) number of frames between FA and FP was -8.21 (9.74) and 2.14 (17.41) frames for HS and TO, respectively. There were no significant differences between BA-FP and BA-FA for both HS and TO (Figure 1a).

Part Two: There were no significant differences in BA-FA between the sidewalk and grass conditions for both HS and TO (Figure 1b).

Conclusions

Based on the results of Part One, FA is similar to FP in determining gait events. The results of Part Two suggest that the BA method detects gait events in a similar manner on both sidewalk and grass surfaces. Therefore, accelerometer-based gait event detection methods can be applied to outdoor running.

References

1. Norris M, et al. *Proc Inst Mech Eng Part P J Sport Eng Technol*. **228(1)**:3-15, 2014.
2. Strohrmann C, et al. *IEEE Trans Inf Technol Biomed*. **16(5)**:983-990, 2012.
3. Lee JB, et al. *J Sci Med Sport*.**13**:270-273, 2010.

Figure

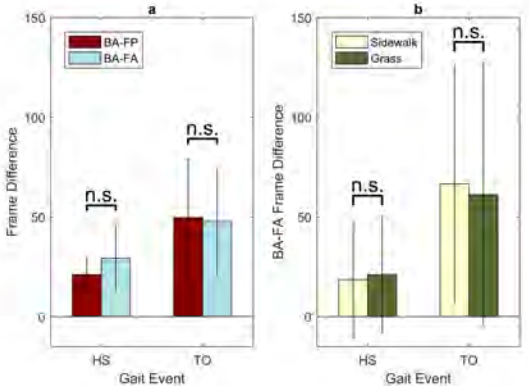

Figure 1: a) Difference between BA-FP and BA-FA during treadmill and b) sidewalk and grass running.

Repeated use of single-use veterinarian needles

K.B. Majcher[1], D.J. Eichhorn[2], J.D. Johnston[1], M.D. Jelinski[3]
1. Department of Mechanical Engineering, University of Saskatchewan, Saskatoon, Canada
2. Division of Biomedical Engineering, University of Saskatchewan, Saskatoon, Canada
3. Western College of Veterinary Medicine, University of Saskatchewan

Introduction: Single-use veterinary needles are frequently used beyond their recommended usage for financial reasons [1]. Broken and imbedded needles may result in animal euthanization, disposal, and monetary losses [2]. In Canada, 41% of processors issue contaminated beef complaints regarding needles annually [3]. Single use veterinary needles provide adequate resiliency to breaking upon first puncture [3]. Equally, dulled needle points are an issue to animal welfare possibly leading to unnecessary pain. To date, no previous studies have been performed assessing the repeated use of single-use needles.

The overall objective of this research was to identify the number of repeated uses prior to needle dulling for various single-use veterinary needle sizes.

Methods:

Specimens: Single use bevel tip (22°) needles of four different gauges (G14, G16, G18, G20) and re-usable stainless steel (SS) needles (G16) were evaluated. Needle hubs were separated from the stem for apparatus securement. The testing puncture material was hydrated untreated bovine leather strips (mean thickness 2.8 mm)

Testing Procedure: Needles were secured to a servo-hydraulic material testing system (MTS Bionix) and lowered at a constant rate of 2 mm/s until complete penetration was achieved. Each needle was puncture tested ten times, except for the G16 SS needles which were tested fifteen times. Leather was secured between two ridged metal plates with an exposed test diameter of 9.52 mm. Between punctures, leather was adjusted to expose a new test site.

Statistical Analysis: Repeated Measures ANOVA was used to access changes in penetration force. Pair-wise comparisons were used to assess whether penetration force changed from one specific penetration to the next. Needle dulling was assumed to coincide with no change in puncture force.

Results: The G14 and G16 needles indicated no change in puncture force between the third and fourth penetrations, indicating that the needle could be used two times prior to dulling. The G18 needle indicated no change in puncture force between the fourth and fifth penetrations, indicating that the needle could be used three times prior to dulling. The G20 needles showed no significant change in puncture force. The puncture force of the re-usable G16 SS needles did not change between tests, signifying no dulling occurred.

Conclusions: Our results indicate that needles G14 and G16 are limited to two repeated uses, G18 three repeated uses, while G20 was not affected by the number of repeated punctures. Nevertheless, we offer a conservative recommendation that single-use veterinarian needles should not be used more than 2-3 times. Findings will facilitate improved knowledge of the strength limitations of single-use needles.

References:

[1] Hunphrey, 2012. [2] Beef Quality Assurance (BQA), 2016. [3] Government of Alberta, 2017. [4] Hoff et al., 1999.

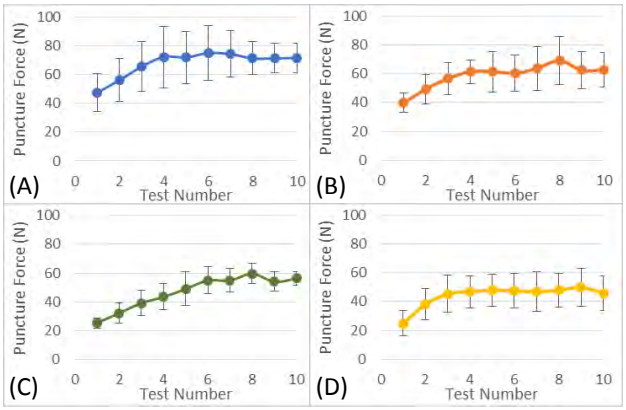

Figure 1. Average Penetration Force Plots; (A): G14. (B): G16. (C):G18. (D):G20

Intercellular Signaling in the Intervertebral Disc with applied Mechanical Load

Russell McWhae, Neil Duncan
McCaig Institute for Bone and Joint Health, Cumming School of Medicine, University of Calgary, 3280 Hospital Drive NW, Calgary, Alberta T2N 4Z6

Introduction

Intervertebral disc (IVD) degeneration correlates with low back pain, a common cause of disability with economic burden. Cells within the IVD are regulated by mechanical, biological and chemical stimuli, and improper regulation can initiate IVD degeneration [1]. Cells in connective tissue such as tendon, ligament, cartilage and bone are known to communicate with each other by calcium ion diffusion across intercellular gap junctions in response to mechanical load [2]. A network of cells exists in the annulus fibrosus, the fibrous outer layer of the intervertebral disc, that may also communicate with each other via calcium ion diffusion [3]. This study examined the active calcium ion response of cells in annulus fibrosus tissue subjected to direct mechanical loading.

Methods

A circumferential strip of live bovine annulus fibrosus was isolated and fluorescently labelled with 15 µM Fluo-4 (Molecular Probes, Eugene, OR) and 30 µM Fura Red (Molecular Probes) (calcium ion indicators) for 90 minutes at 37°C, rinsed in 100-times volume of calcium-free PBS for 25 min (5×), and loaded in uniaxial tension on a confocal microscope (Zeiss LSM 710, 20×1.0 NA water immersion objective, 488 nm argon laser, 18.7 µm optical slice), as shown in 1. Images were captured at strains of 0, 1%, and 5% at a loading rate of approximately 1%/min. The ratio between the Fluo-4 and Fura Red signals was analyzed and used to quantify the calcium response magnitude and duration.

Results

Figure 2 shows an increase in fluorescence intensity at 1% strain (arrow), which then decreases at 5% strain (the green channel represents the Fluo-4 signal, which increases with a calcium ion release, and red represents the Fura Red signal, which decreases with a calcium ion release).

Conclusions

Understanding the cellular response to mechanical loading *in situ* could help elucidate the biomechanical process of disc degeneration. Further work will include a microscope incubator controlling temperature, carbon dioxide and oxygen levels, and humidity to accurately simulate physiological conditions of the live tissue.

References

[1] Vergroesen *et al.*, *Osteoarthritis Cartilage*, pp. 1–14, 2015.
[2] Guilak *et al.* in *Cell Mechanics and Cellular Engineering*, Mow et al., Eds. Springer, New York, NY, 1994, pp. 380–397.
[3] Desrochers and Duncan, *CMBBE*, pp. 1–8, 2012.

Figures

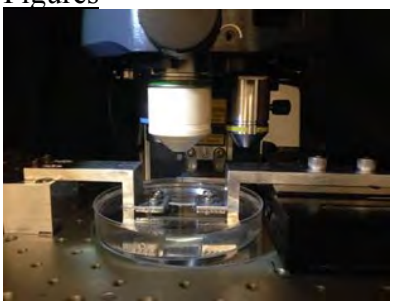

1. Loading apparatus on confocal microscope.

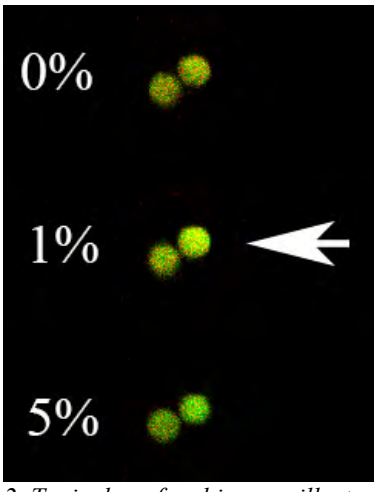

2. Typical confocal images illustrating fluorescence intensity of bovine outer annulus cells in situ *at indicated strain.*

Parkour wall climbing: Simple physics of an extreme task

Ryan T. Schroeder, James L. Croft and John E.A. Bertram
3C45A HRIC, Foothills Campus - 3330 Hospital Drive NW, Calgary AB T2N 4N1 (ryan.schroeder@ucalgary.ca)

Introduction

The urban sport of Parkour provides an extreme example of gait not commonly viewed in general populations—namely an abrupt transition from a horizontal to a vertical surface. This provides a rare opportunity to test hypotheses about the control of effective leg function.

In the Parkour wall climb an athlete runs toward a wall, leaps off the ground, and kicks off the wall with continuous motion. Both the ground and wall impulses are used to gain sufficient ballistic height to grasp the top edge of the wall. Even though a highly specialized maneuver, we theorized a control strategy minimizing mechanical work, as has been demonstrated for many aspects of typical gait. Consequently, we hypothesized that Parkour athletes employ an energy-preserving strategy transferring run-up velocity (related to kinetic energy) into height (proportional to potential energy) and performing little to no external work via ground reaction forces, a strategy referred to as energy transfer.

Methods

To test whether energy transfer is a prominent control feature during wall climbing, six Parkour enthusiasts in Perth, Australia were asked to scale a three-meter-high wall over ten or more trials. Ground reaction forces were measured with a force plate on the ground and another on the wall. The plates were calibrated with known loads, and a double integration was performed to calculate center of mass kinematics. Average kinematic profiles were calculated within individual and pooled subject data. Also, sagittal videos were digitized with custom MATLAB scripts [1] to incorporate initial conditions and to validate calculation of the center of mass kinematics. The resulting kinematics were then compared to an ideal, zero-work-based model for energy transfer (Fig. 1).

Results

The ideal model exhibits a smooth deceleration with increases in height (Fig. 1). Averaged empirical data follow a similar trend, but with moderate velocity fluctuations in either direction. These fluctuations reveal a limitation of the legs' ability to provide forces in ideal orientations (i.e. normal to the body's trajectory). The average data indicate that subjects performed slightly more positive work than negative work over the wall climb event, indicating that energy transfer is not the only strategy employed.

Conclusions

Although the control task of a Parkour wall climb is well explained by a strategy of energy transfer, insights into what makes a successful wall climb can also inform appropriate techniques for training and injury prevention of not only Parkour athletes, but police and military trainees as well.

References

[1] Hedrick, TL 2008. *BIOINSPIR BIOMIM*. 3(3):034001

Figures

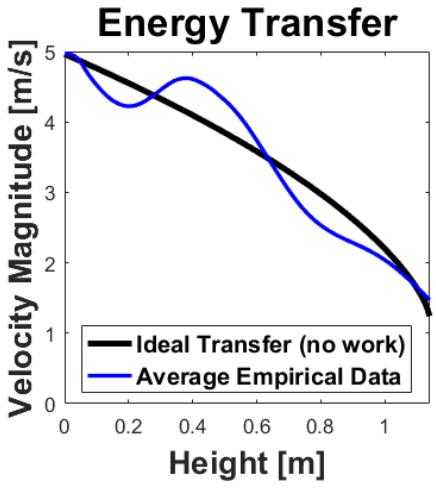

Fig. 1 – Velocity magnitude (related to kinetic energy) versus height (proportional to potential energy) is shown for ideal energy transfer and average subject data.

A Novel Approach for Fitting the Parameters in Cardiac Cellular Model through a Linear Least Squares Formulation of Currents

Elnaz Pouranbarani and Anders Nygren
Electrical & Computer Eng. Departement, University of Calgary

Introduction

Cardiac cellular modeling plays a crucial role in the drug discovery and development process. The action potential (AP) is a key electrophysiological feature of cardiac cells, and cellular models aim to reproduce an action potential accurately. To obtain a realistic action potential, several parameters in these models need to be tuned. Prevalently, empirical approaches are utilized for tuning these parameters, which is time-consuming [1]. Alternatively, strategies have been devised to find the unknown parameters using heuristic optimization techniques that require high computational burden and often depend highly on the initial guess. To avoid these problems, we propose a linear least squares-based formulation, based on the action potential clamp concept, for fitting the action potential shape via the total current.

Method

Two well-established human heart cellular models, called Ten Tusscher (target model) [2] and O'Hara model (model to fit) [3] are employed in this work. The problem of fitting the action potential shape is reformulated in terms of fitting the total current. In this method, the cellular model is "clamped" using the target action potentials (Ten Tusscher). Consequently, the nonlinear problem is transformed to a linear least square problem. Then, by considering seven parameters ($G_{to,}$ G_{Kr}, G_{Ks}, G_{K1}, G_{ncx}, $P_{Cab,}$ and $P_{NaK)}$ as unknown variables and the total current (I_{total}) as a objective function, the problem of fitting is solved. As a bench-mark, a genetic algorithm-based approach (population size=50 and generation=100) is compared to the proposed method.

Results

As the first step, O'Hara waveforms, modified by tuning the seven aforementioned parameters, were acceptably fitted to the original O'Hara waveforms. This verifies the successful performance of the proposed method in fitting a model to itself (Fig.1 (a), (b)). Mean squared error (MSE) of fitting different modified O'Hara total current waveforms to the original one are 0.003, 0.006 and 0.010 respectively. Furthermore, the efficacy of the proposed algorithm in a model-to-model fit was evaluated as shown in Fig.1 (c) and (d). It can be perceived from Fig.1 (c), in part of the repolarization phase, that the fitted model is not perfectly matched to the target. This is to be expected, given the limited number of free parameters. The performance of the proposed method and genetic algorithm (GA) are summarized in Table I, which confirms the superiority of the proposed approach.

Conclusions

In this paper, by taking advantage of the action potential clamp concept, the cellular modeling problem is reformulated into a linear least-squares problem. The results show the effectiveness of this approach in comparison to the heuristic method in terms of computational time, MSE, as well as reproducibility of result.

References

[1] W.Groenendaal, , *PLoS Comput.Biol. 2015;11: e1004242*
[2] T.Tusscher, *bio & Mol bio. 2006;90:* 326-345
[3] T. O'Hara, *PLoS Comput.Biol. 2011,7: e1002061*

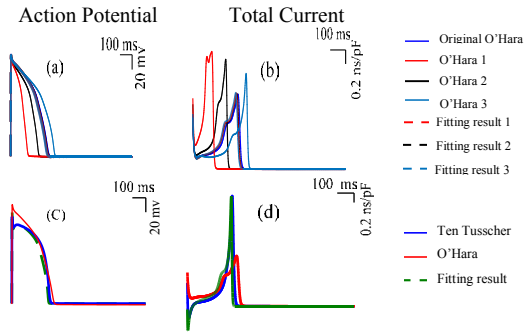

Fig.2. (a),(b): Fitting O'Hara 1 (red), O'Hara 2 (black), O'Hara 3 (light blue) to original O'Hara (blue) . (c),(d): Fitiing O'Hara (red) to Ten Tusscher (blue).

Table I: Comparing the performance of the proposed method and GA

Method	MSE (I)	Computational Time (s)
Proposed approach	**0.088**	**3.398**
GA (run 1)	0.265	3327.378
GA (run 2)	0.137	3431.060
GA (run 3)	0.126	3611.640
GA (run 4)	0.201	3461.945

Automated Segmentation of Callus and Cortical Bone in Distal Radius Fractures Using Machine Learning

Christopher M. O'Neill[1], Danielle Whittier[1], Steven K. Boyd[1]
[1]McCaig Institute for Bone & Joint Health, Cumming School of Medicine, University of Calgary, Calgary, AB

Introduction

High resolution peripheral quantitative computed tomography (HR-pQCT) is well suited to assess changes in bone density and microarchitecture due to aging, disease, or treatments [1-3]. Recently, HR-pQCT has been applied to analyze fracture healing *in vivo* at the distal radius [4]. Although existing segmentation methods are effective in standard cases, they do not perform well for fractured bone where the cortical bone is fragmented, and current segmentation methods do not account for presence of callus. To effectively analyze fracture healing, a method to reliably segment cortical bone fragments and callus is needed. The aim of this study is to develop and validate a robust automated segmentation algorithm to identify callus and cortical bone in HR-pQCT scans of distal radius fractures.

Methods

Four female participants with stable distal radius fractures and mean age of 56 years were scanned along a 20.4 mm region at the fracture site using HR-pQCT (XtremeCT II, Scanco Medical AG) at 61 µm isotropic resolution. Images were smoothed using a two-dimensional (2D) 5x5 Gaussian filter, and 7 first-order features, including local mean, median and standard deviation, were computed for each voxel in the image. The original image greyscale values were binned into 10 discrete grey levels and 24 second-order texture features were extracted using a 2D 15x15 kernel. Second order texture features consisted of grey level run length matrix (GLRLM) parameters. Size-matched samples of cortical bone and callus were then extracted, and used to train a linear support vector machine (SVM) classifier with 10-fold cross validation. The trained classifier was then used to classify the original image. The automatic segmentation was compared to a manual segmentation performed by a trained rater using Jaccard similarity coefficients.

Results

Scans were split into distal and proximal regions for analysis. A slicewise view of the manual and automatic segmentations is shown in Figure 1. The Jaccard similarity coefficients for the cortical bone and callus in the proximal scan region were 0.82±0.05 and 0.18±0.13, respectively, whereas the coefficients were 0.54±0.12 and 0.23±0.12, respectively, in the distal scan region.

Conclusions

The automatic segmentation compared well with the manual segmentation of cortical bone in the proximal region, and moderately in the distal region where it is thinner. The automatic segmentation performed poorly overall when segmenting callus. This is likely due to the high level of subjectivity in the manual segmentation by a single rater and the choice of using a 2D kernel for voxel features. Better definition of true callus in HR-pQCT scans is needed to improve and validate the segmentation algorithm of callus *in vivo*, and it is recommended the use of three dimensional kernels for voxel feature extraction be explored.

References

[1] Dalzell, N, et al., Osteo. Int (2009) Oct;20(10):1683-94. [2] Bacchetta, J, et al., JBMR (2010) Apr;25(4):849-57. [3] Burghhardt, AJ, et al., JBMR (2010) Dec;25(12):2558-71 [4] de Jong, JJA, et al., Bone (2014) Jul;64:356-62. 5.

Figures

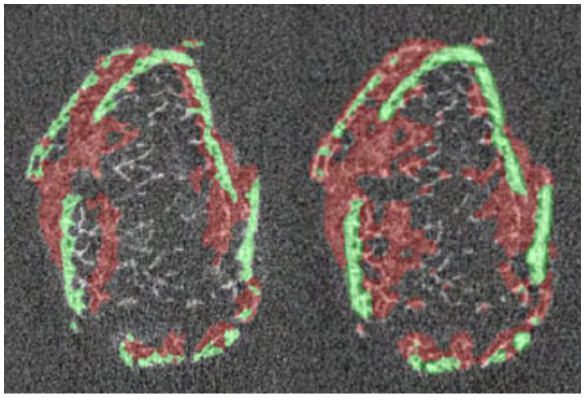

Figure 1: Comparison of manual (left) and GLRLM (right) segmentations in the proximal region.

Ultrafast High-Frequency Focused Beam Blood Flow Imaging

Bingjie Ma, Tarek Kaddoura, Min Choi, Ryan Chee, Quinn Barber, Mrinal Mandal, Roger Zemp

Introduction

High-frequency ultrasound (>20MHz) offers promising opportunities for high-resolution bloodflow imaging of the microcirculation at superficial depths owing to high backscatter coefficient and high resolution [1]. Plane-wave imaging offers improved sensitivity to slow blood flows owing to potential for accruing large ensembles of RF images for spatiotemporal flow estimation compared to traditional Doppler methods using limited numbers of ensembles per color Doppler A-scan. However, image quality is low, producing images with low SNR, decreased resolution, and high levels of clutter, especially in vivo [2]. Our approach uses high-frequency focused beam imaging which can reach frame rates nearly as high as that of ultrafast plane wave imaging due to shallow penetration depths and minimal time-of-flight. We aim to compare our ultrafast focused (UFF) method (also named Fast Walking Aperture) with plane wave (PW) and traditional Doppler (TD) sequences.

Methods

In order to show the advantage of UFF imaging compared with TD and PW Doppler, we performed Field II simulations and phantom experiments. We simulated a 20MHz high frequency transducer and measured blood flow with a range of speeds up to a maximum velocity of 0.01m/s at penetration depths <20mm. To implement UFF Doppler we used a frame rate of 1KHz. Each B-scan frame contained at least 20 A-scan lines. Ten pulse transmissions per line of sight for TD was used for comparison using 1KHz repetition rates, equivalent to the UFF frame-rate. In addition to simulations, we use a Visualsonics 21MHz array transducer connected to a Verasonics Vantage system to image flow phantoms with maximum flow velocity 0.01m/s at penetration depth around 10mm, The UFF can get frame rate to 780fps which is 10 times of TD and close to that of PW method. Within the same time period, the ensemble size of TD is 10 and of both UFF and PW are100.

Results

UFF imaging methods offered at least 200 times higher ensemble size than TD. These larger ensemble sizes, exhibited flow with lower variance and significantly greater sensitivity to slow flow speeds. The variance using TD and UFF with the above parameters was measured to be 0.0414 and 0.0038, respectively. Lower variance brings more continuous blood flow imaging. The SNR using PW and UFF with the above parameters was measured to be 17.6135 and 39.3462 dB, respectively.

Conclusion

In summary, we observed that UFF have best performance to resolve and measure slow flows. Higher image quality with higher SNR was achieved by using ultrafast focused (UFF) walking aperture compared to plane-wave (PW) or traditional Doppler (TD) methods.

Reference

[1] DAVID E. GOERTZ, DONALD A. CHRISTOPHER, JOANNE L. YU, ROBERT S. KERBEL, PETER N. BURNS and F. STUART FOSTER, "High-frequency color flow imaging of microcirculation," *Ultrasound in Med. & Biol.*, vol. 26, no. 1, pp. 63-71, 2000

[2] M. F. Mickael Tanter, "Ultrafast Imaging in Biomedical," *IEEE Transactions on Ultrasonics, Ferroelectrics, and Frequency Control,* vol. 61, no. 1, January 2014.

Figures

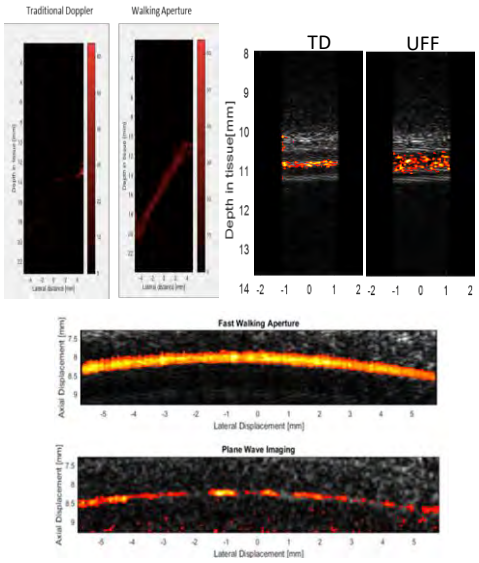

POSTER PRESENTATION ABSTRACTS

The Translamellar Cross Bridge Structures of the Intervertebral Disc

Chris Urbinsky, Jeff Dunn, John Matyas, Neil Duncan
McCaig Institute for Bone and Joint Health, Cumming School of Medicine, University of Calgary, 3280 Hospital Drive NW, Calgary, Alberta T2N 4Z6

Introduction

Several studies have identified radial structures in the intervertebral discs of animals and humans, generally referred to as 'translamellar cross-bridges'[1,2,3] (TLCB's), that span the circumferential lamellae of the annulus fibrosus (outer disc) that surrounds the inner nucleus pulposus.

What has not been shown is the full 3D extent of these structures throughout the annulus, nor is their contribution to disc mechanics well understood.

Our objective is to image and characterize the extent of this network, and quantify the TLCB's mechanical contribution to the disc.

Methods

High field (9.4T) Magnetic Resonance (MR) Imaging. 3D sequence to image bovine disc samples. Processing of the resultant image data using phase congruency edge detection.

Optical Coherence Tomographic (OCT) imaging of radial disc samples under load to compare the behavior of samples containing radial tie fibers (TLCB's) to those without.

Results

Qualitatively, the MR images appear to show a woven network extending throughout the annulus (Fig. 1) Where the fibers parallel to the lamellae intersect fibers in adjacent lamellae, which run at alternate 60-degree angles, they appear to be connected. Structures matching the previously identified TLCB's are apparent where fibers in multiple adjacent lamellae connect at a similar location.

A phase congruency edge detection algorithm[4] has been used to identify these structures algorithmically (Fig. 2).

As a method of validation, using similar methods[2], preliminary imaging has also shown that the translamellar cross-bridge structures are identifiable using OCT (Fig. 3), allowing for imaging of samples under load in near real time to further assist in quantifying the contribution of the network to disc mechanics.

Conclusion

This research shows promise to better understand the structure and multi-scale mechanics of the intervertebral disc, as well as a basis for design of tissue engineering methods and scaffolds to approximate the natural structure of the disc.

References

1. Schollum, et al. *J. Anat.* **214,** 805–816 (2009).
2. Han, et al. *J. Orthop. Res.* **33,** 304–311 (2015).
3. Yu et al.*Spine.* **40,** 1158–1164 (2015).
4. Kovesi, P. - *DICTA 2003* 309–18 (2003).

Figures

Figure 1 (above left): Slice from MR Data. **Figure 2** (above right) Slice with Edge Detection Algorithm Applied. **Figure 3** (below) Clip through 3D reconstruction of OCT image data showing TLCB.

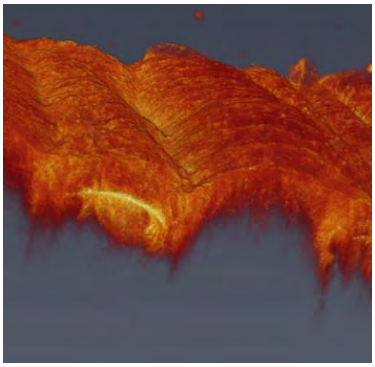

Design overview of an automated running wheel to examine recovery of spinal cord injured (SCI) mice

Leanne Young, Kyle Mayr, Patrick Whelan
Hotchkiss Brain Institute, University of Calgary, Calgary, Alberta, Canada

Introduction

Spinal cord injury (SCI) is a debilitating issue affecting 86,000 Canadians, however, goal-directed rehabilitation has shown improved recovery following injury (1). Our group is interested in examining neuropeptide related properties following goal-directed rehabilitation by comparing cohorts of SCI mice that have either daily passive treadmill training or access to a running wheel in their home cage.

To carry out this study, an automated running-wheel solution requires: revolution counting to track distance run, multi-animal housing, a locking system to operate after a mouse runs a given distance, a wireless system to handle 16+ wheels simultaneously, and a common receiver node that allows user communication with the wheels and data collection. Currently, no technology that meets these criteria is commercially available.

Methods

The wheel component uses an Arduino Nano operated by a 9V battery and the receiver node uses an Arduino Uno, which operates off the computer power. The wheel revolutions are counted by a hall effect sensor, which detects changes in its magnetic field, placed in the wheel base with a small magnet embedded into the wheel. Each mouse is implanted subcutaneously with an RFID transponder and an RFID reader sits in the wheel base. The locking system uses a micro servo that places resistance on the wheel axle to prevent further revolutions. Wireless transceivers communicate between the receiver node and each wheel. The receiver node user interface (UI) was generated in Matlab. The wheel bases were 3D printed.

Results

We have completed all software and hardware development. We will be testing it shortly in a cage housing multiple mice. When a mouse gets on the wheel, the RFID reader will scan its implanted tag and the hall effect sensor will detect the wheel revolutions. Once the mouse reaches its revolution limit, the servo will rotate to lock the wheel. The revolution counts and wheel lock status are associated with each RFID tag so that the conditions are held for each individual mouse.

The UI has multiple features that allow the user to easily interact with the wheels such as pinging the wheels to check the wireless connection or resetting the revolution counts for individual or multiple mice.

Conclusions

We expect this wheel-setup fills a market void and provides the technology necessary for SCI rehabilitation studies in mice. Further, this technology can be customized for applications in other types of studies requiring locomotor activity tracking.

References

1. van den Brand R, Heutschi J, Barraud Q, DiGiovanna J, Bartholdi K, Huerlimann M, et al. Restoring Voluntary Control of Locomotion after Paralyzing Spinal Cord Injury. Science. 2012 May 31; 336(6085):1192-5.

Figures

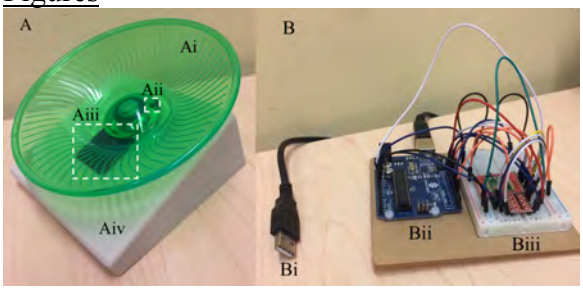

Figure 1. Ai: wheel; Aii: hall effect sensor; Aiii: RFID reader; Aiv: wheel base; parts under wheel base not shown: 9V battery, Arduino Nano, wireless transceiver, micro servo; Bi: USB connection to computer, Bii: Arduino Uno, Biii: wireless transceiver

Geometric and Strain-Based Analysis of Abdominal Aortic Aneurysms Undergoing Open Repair vs Endovascular Repair

Harsupreet Sidhu, Flavio Bellacosa Marotti, Arianna Forneris, Randy Moore, Elena S. di Martino
Biological Tissue Mechanics Lab, University of Calgary

Introduction

Abdominal aortic aneurysms (AAAs), which account for 80% of aortic aneurysms, occur between the renal arteries and aortic bifurcation, below the chest [1]. Currently, there are two treatment options: open repair surgery, which is completed by making a large incision or endovascular repair, which only requires a small opening by the groin.
Our lab currently investigates the mechanical properties of the aorta of AAA patients to determine if they may provide indications to surgeons to decide whether a patient is considered for surgery. The focus of this project was to apply statistical methods to analyze the mechanical properties of AAAs selected for surgery. The type of surgery a patient undergoes is normally decided based on clinical and geometrical factors including proximal neck angulation, diameter of the iliac artery, and certain patient features such as age and gender [1,2]. Our approach was to consider the intraluminal thrombus thickness and local deformation of the aortic wall, properties which were obtained pre-operatively.

Methods

Ten patients undergoing surgical repair of their AAAs, 5 undergoing open surgery and 5 endovascular surgery, were analyzed. Key steps in data acquisition included acquiring multiphase CT data and creating a 3D reconstruction of the aorta that was split into patches giving us a total of 48 data measurements for each patient. One-tailed t-tests for comparison between operation types and two-way analysis of variance (ANOVA) using patients and patches as factors were run to observe statistically significant differences. Properties tested included thickness of intraluminal thrombus, maximum principal stress, maximum principal strain, and the constrained deformation ratio (CDR), a ratio of circumferential and axial stretch.

Results

The resulting box plots from the tests showed no statistical difference for the aforementioned mechanical properties between data collected for each surgery type. There is an observable difference in thrombus thickness between the two groups. The two-way ANOVA showed significant difference among patients for both maximum principal strain and CDR, and between patches for CDR.

Conclusions

The absence of any statistical difference in the mechanical properties between the two groups suggests they are not factors in determining which operation a patient should undergo. The results from thrombus thickness showed that patients selected to undergo endovascular repair had more variation in thicknesses and an overall greater mean. Looking at differences among patients and using the location on the aorta as a factor, we found that the maximum principal strain was different between patients, suggesting that strain measures can be used to classify patient risk. CDR was different between patients and based on the location on the aneurysm. CDR may be especially interesting since the areas on the aortas where this property was consistently elevated corresponded with areas deemed as high risk of rupture by surgeons.

References

1. Aggarwal et al. *Exp Clin Cardiol.* **16**:11-15, 2011.
2. Iezzi & Cotroneod. *Abdom Imaging.* **31**:722-731, 2011.

Single Fibre Force Production in the Triceps Surae Following Chronic Exercise Training

Boldt, K. R.[1, 2], Rios, J. L. [1, 2], Joumaa, V. [1, 2] & Herzog, W. [1, 2]
[1]Human Performance Lab, University of Calgary, [2]Faculty of Kinesiology, University of Calgary

Introduction

Physiological adaptations of skeletal muscle to exercise training have been well documented[1-3]. However, it is not as well understood how skeletal muscles adapt mechanically. The purpose of this study was to evaluate the dose-dependent effects of chronic aerobic exercise training on skeletal muscle force properties.

Methods

Twenty-four 3-month-old Sprague-Dawley rats were randomized into four groups: moderate duration exercise (MD; 30 minutes 5 days/week) (n=6), high duration exercise (HD; 60 minutes 5 days/week) (n=6), extra high duration exercise (EHD; completed 60 minutes 7 days/week) (n=6), or no exercise (CON) (n=5). In weeks 9, 10, and 11, EHD animals also completed 2, 3, and 4 sessions/day (up to 4 hours). Animals trained on a treadmill for 11 weeks at 25m/min. One week following the exercise training, muscles of the hind limb were dissected and weighed. Soleus and gastrocnemius muscles were chemically skinned in solution for 3 weeks. Mechanical testing consisted of isolating and attaching skinned fibres on one end to a force transducer and at the other end to a length controller. Average sarcomere length was set to 2.2 µm using laser diffraction. Fibres were maximally activated to determine maximum force production. Following these activations, fibres were passively stretched 25% of their initial length (to an average sarcomere length of 2.75um) and held for 20 seconds until stress relaxation led to steady state force. Fibre type (Soleus-slow and Gastroc-fast) was confirmed using pSr.

Results

Absolute muscle mass of the lower limb was greater in the MD group compared to all the other groups (p=0.015), but not different between the CON, HD, and EHD group animals. Relative to body mass, muscle mass was not different between CON, MD, and HD, but was greater in the EHD group compared to all the other groups (p=0.010).

Active stress production was not different in the soleus between the CON, MD, or EHD groups, but was significantly lower in the HD group animals (p=0.042). There were no differences between any groups for active stress production in the gastrocnemius. Passive stresses were not different between any of the groups (p=0.092-0.666).

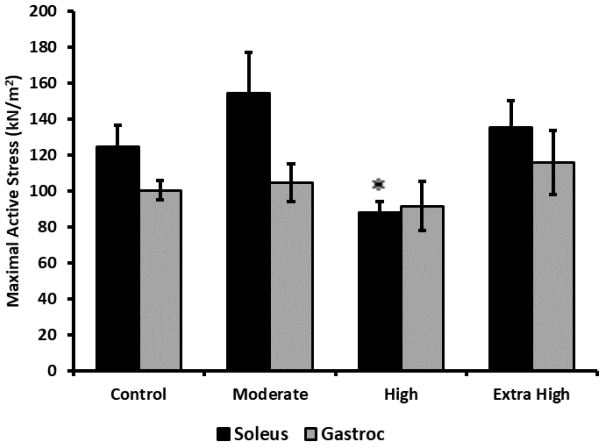

Figure 1. *Maximum active stress for single fibres from soleus and gastrocnemius.*

Conclusions

Moderate levels of treadmill running led to a greater muscle mass in MD group compared to sedentary animals. Higher levels of aerobic training led to a decrease in muscle mass. However, relative to body mass, the EHD group animals had greater muscle mass, likely because of the reduced body weight associated with a lower body fat content in the EHD group compared to the other group animals.

Maximal active force production was not different across groups, except for lower force in the HD soleus. Passive forces were not significantly altered by training.

References

1. Allen et al. (2001). *J, Applied Phys., 90*(5).
2. Gibala et al. (2006). *J. Phys., 575*(3).
3. Carter et al. (2001). *Can. J. Phys. Pharm., 79.*
4. Hoar et al. (1979). *J. Phys. 295*(1).

A robust daily activity analysis methodology using a single tri-axial accelerometer mounted on the chest

Milad Nazarahari[1], Hossein Rouhani[1]
[1]Mechanical Engineering Department, University of Alberta, Edmonton, AB, Canada

Introduction

Population growth and increase in life expectancy lead to an aging population that considerably challenges the healthcare system due to increasing health care costs. At the same time, investigations showed that quantification of daily physical activities (PAs) provides the chance to evaluate the functional ability and quality of life of elderly population and patients with limited mobility. The nature of long-term PA monitoring proposes the application of wearable inertial measurement units (IMUs) in the free-living environment.

The previous research works in the literature are (1) unable to detect a wide range of PAs using a single IMU [1,2], and (2) not robust against different movement habits as they were developed based on features of the signals and not the PAs [3]. As such, the purpose of this study is to develop a robust approach based on a single IMU mounted on the chest to identify a broad range of PAs.

Methodology

An experimental study has been performed in a free-living environment with ten healthy participants that performed eight activities including standing, sitting, level walking, walking upstairs/downstairs, and lying. During the experiments, a tri-axial accelerometer was attached to their sternum (Fig. 1).

To determine the posture of the body, first, postural transitions (PTs) were detected and classified. Next, the body posture was determined based on the identified PTs. Trunk inclination was used as a robust measure to detect the PTs. The largest variations (peaks) in the trunk inclination correspond to lie-to-sit/sit-to-lie transitions, and the smaller ones correspond to sit-to-stand/stand-to-sit transitions or walking.

It was shown that during sit-to-stand/stand-to-sit transitions, the acceleration always follows a certain pattern, which can be used for accurate classification of these transitions. Level walking periods were detected from the successive peaks of the acceleration pattern above a predefined threshold. Again, trunk inclination was used to differentiate between walking upstairs/ downstairs and level walking.

Results

Lie-to-sit, sit-to-lie, and stand-to-sit transitions were detected and classified with sensitivity and specificity of 100% among all participants. While the specificity of identifying sit-to-stand transitions was 97%, the sensitivity of 100% was achieved by the proposed method. Also, walking periods were correctly distinguished and the number of steps counted with the accuracy of 95% or higher in different walking speeds.

Conclusion

Classification of the body postures using features originated from the biomechanical nature of the postural transitions has shown high classification rates and robustness among different participants. This method can be utilized as a robust tool for long-term daily activity analysis.

References

[1] Godfrey et.al. (2011) Med. Eng. Phys. 33, 1127–1135.

[2] Najafi et.al. (2004) Biomed. Eng. IEEE Trans. 50, 711–723.

[3] Karantonis et.al. (2006) Inf. Technol. Biomed. IEEE Trans. 10, 156–167.

Figures

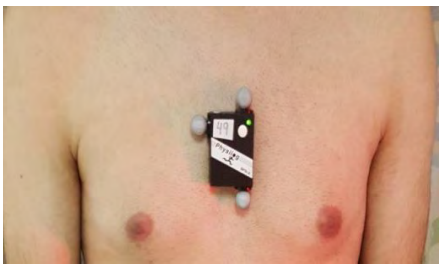

Figure 1: IMU placement on the chest. Three reflective markers are attached to the IMU only for validation of the detected postural transitions using motion capture cameras.

Altered Synovial Fluid Proteoglycan 4 (PRG4) / Lubricin Concentration and Structure in Rheumatoid and Juvenile Inflammatory Arthritis

Das, N; Regmi, S; Veeramreddy DN; Schmeling H; Krawetz, RJ; Schmidt, TA
University of Calgary, Calgary, AB, Canada

Introduction

Proteoglycan 4 [PRG4], also known as lubricin, is a mucin-like glycoprotein and key macromolecular constituent of synovial fluid (SF)[1]. While classically studied and described as a boundary lubricant, recently it has also been found to have biological (e.g. anti-inflammatory) properties[2]. SF concentration of PRG4 composition can be altered in osteoarthritis (OA) and rheumatoid arthritis (RA)[3,4], resulting in altered lubricating functional and/or biological activity in terms of binding and activating various cell surface receptors. Juvenile Idiopathic Arthritis (JIA) is a form of inflammatory arthritis like RA, though PRG4 composition has yet to be studied in this patient population. Furthermore, it remains unclear if concentration of full length PRG4 alone is altered in arthritis, or if there is fragmentation of PRG4 as well potentially contributing to altered SF function in these different inflammatory conditions.

The objective of this work was to characterize PRG4 concentration and structure in human SF samples from normal (NL), OA, RA and JIA patients.

Methods

Human SF NL, OA, RA, and JIA (N=9-10 each) samples were collected and processed by centrifugation and storage at -80^{o}C. PRG4 concentration was determined via a competitive amplified luminescent proximity homogeneous assay (AlphaLISA)[5], using anti-PRG4 mAb 9G3 (Millipore, recognizes central mucin domain) and recombinant human PRG4 (Lubris, BioPharma) as a control[6]. PRG4 structure was characterized via SDS-PAGE western blotting, both 3-8% and 10-20% (Life Technologies), using mAb 9G3 and anti-peptide pAb LPN (c terminal). SF samples were treated with hyaluronidase prior to electrophoresis, and were examined under non-reducing conditions[6].

Results

PRG4 concentration was greatest in both JIA (4189±650 ug/ml, mean±SEM) and RA (3532±283 ug/ml), both of which were significantly greater ($p<0.001$ to $p<0.05$) than the concentration in both OA (1816±244 ug/ml) and NL (1264±216 ug/ml). PRG4 concentration in JIA was similar to RA, and that in OA similar to NL. While all samples demonstrated high MW, full length immunoreactivity to mAb 9G3 (*), in only JIA and RA was a lower MW (~65kDa) LPN immunoreactive fragment (**, Fig 1) observed.

Conclusions

These results agree with and extend previous studies demonstrating that PRG4 concentration is altered in inflammatory SF, here reporting an increase in both RA and JIA, and for the first time observe a lower MW PRG4 fragment in these samples. The specific protein identify[7], and proteolytic source of the fragment, as well as potential biological function are areas for future research. Characterization and quantification of PRG4 fragments in inflammatory SF could contribute to further understanding of PRG4's role in joint health and homeostasis.

References

1. Jay+ Mat Bio '14 2. Iqbal+ Sci Rep '16 3. Ludwig+ A&R '12. 4. Elsaid+ A&R '08 5. Alirifi+ ARVO '17. 6. Abubacker+ An BME '16 7. Regmi+ EER '17.

Figures

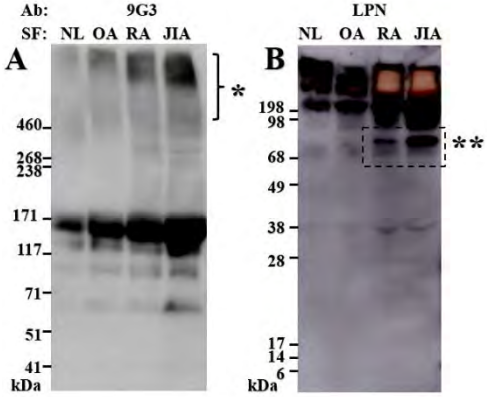

Fig.1.SDS-PAGE western blotting of PRG4 with mAb 9G3 and Ab LPN in NL, OA, RA, and JIA SF.

Using HR-pQCT and finite element analysis at the tibia to differentiate vertebral fracture patients from healthy controls

Jacob K. George [1,2], Lauren A. Burt [1,2], Steven K. Boyd [1,2]
[1] McCaig Institute for Bone and Joint Health; [2] Department of Radiology, Cumming School of Medicine, University of Calgary

Introduction

Osteoporosis (OP) is a disease defined by deterioration of bone structure, resulting in increased bone fragility and fracture risk. The most common major osteoporotic fracture is vertebral [1].

Bone microstructure can be imaged and quantified through High- Resolution peripheral Quantitative Computed Tomography (HR-pQCT). Virtual loading tests can be applied to these scans through Finite Element (FE) models, allowing for an estimation of bone mechanical parameters.

HR-pQCT scans cannot be performed on the spine; however tibia scans have indicated differences between vertebral fracture patients and age-matched controls, most significantly in bone mineral density (vBMD) and compression FE modulus of elasticity (E_{axial}) [2,3,4]. These findings suggest that evaluating vertebral fragility may be possible though tibia scans. This study aims to determine whether alternate loads by FEA (bending and torsion) can better distinguish the presence of a vertebral fracture.

Methods

HR-pQCT tibia scans from postmenopausal women with a vertebral fracture within 5 years (N=10) were compared to a group of age- and sex-matched controls (N=20) with no fracture history. These scans were retrospectively collected from the Canadian Multicenter Osteoporosis Study (CaMos).

Distal tibia scans were contoured, thresholded and segmented into cortical and trabecular regions using Image Processing Language (IPL V5.07). Microstructural parameters were calculated from segmented images.

A linear FE analysis in compression (1% uniaxial strain), torsion (1° twist) and bending (1° bend) was performed using FAIM 7.1; mechanical parameters like modulus of elasticity (E), Von Mises Stress (σ_{VMS}) and Strain Energy Density (u_{SED}) were simulated. Student's t-tests compared the healthy group to the injured.

Results

Consistent with previous studies [3][4], both vBMD (15.0% diff, $p<0.05$) and E_{axial} (14.5% diff, $p<0.05$) were significantly different between the groups.

Torsion, bending, and HR-pQCT parameters had larger differences in their trabecular properties compared to their cortical, though only trabecular Strain Energy Density (u_{SED}) and Von Mises Stress (σ_{VMS}) in bending reached significance. Summarized FE results are shown in Table 1.

Conclusion

This study's importance lies in tibia microstructure and the FE method being able to differentiate vertebral fractures from controls.

Table 1 indicates greater trabecular differences between the groups. Given that vertebrae are a trabecular-dominant bone, systematic changes in trabecular bone would correlate with an increased risk of vertebral fracture.

This pilot study is in the process of being validated with a larger cohort (N= 29 fx, N=58 control) drawn from multiple centers in Canada. Future work will determine if FE outcomes improve vertebral fracture classification beyond that of HR-pQCT microstructure and BMD, justifying the computational cost of the test.

References and Figures

1. Melton et al. Osteo Int. 1993; 2. Wang et al. Bone. 2016
3. Sornay- Rendu et al. JBMR. 2009; 4. Vilayphiou et al. Bone. 2010;

Table 1: Differences between fractures and controls in avg. σ_{VMS}, avg. u_{SED} and E through tested FE loadings. **Bolded** values indicate significant differences in student's t- test ($p<0.05$)

	Axial [% diff]	Torsion [% diff]	Bending [%diff]
Trabecular σ_{VMS}	0.12	6.28	**7.43**
Cortical σ_{VMS}	0.16	4.05	2.60
Trabecular u_{SED}	0.64	12.1	**12.6**
Cortical u_{SED}	1.62	8.52	4.28
E	**13.5**	3.44	3.45

Ex vivo Validation and In vivo Repeatability of HR-pQCT FE-based Distal Radius Bone Strength

Seyedmahdi Hosseinitabatabaei[1], Chantal Kawalilak[2], Matthew P. McDonald[2], Saija A. Kontulainen[3] James D. Johnston[1,2],
[1] Division of Biomedical Engineering, University of Saskatchewan, Saskatoon, SK, Canada
[2] Mechanical Engineering Department, University of Saskatchewan, Saskatoon, SK, Canada
[3] College of Kinesiology, University of Saskatchewan, Saskatoon, SK, Canada

Introduction

Colles' fracture is the most common osteoporotic fracture in women and an important predictor of other osteoporotic fractures [1]. Bone fracture occurs when the external forces applied to bone exceed the bone strength. High resolution peripheral quantitative computed tomography (HR-pQCT), combined with finite element (FE) modeling, can be used to estimate distal radius failure load. Currently, the standard HR-pQCT-based FE model does not account for variations in bone tissue's mechanical properties. Further, the standard model has been validated using embalmed specimens, which can alter bone's mechanical properties [2].

Using HR-pQCT imaging, FE modeling and mechanical testing, the first objective of this study was to validate a FE model which accounts for variations in tissue mechanical properties using distal radius images obtained from fresh-frozen cadaveric forearms. The second objective was to define in vivo precision errors for distal radius bone strength predictions for different FE modeling parameters and failure criteria.

Methods

Specimens: We acquired 19 cadaveric forearms and potted their midshafts in bone cement (PMMA). We imaged the distal radius via HR-pQCT (Scanco) using the standard clinical protocol [3]. To define FE precision errors in vivo, we imaged the radius of 28 postmenopausal women at two time points.

Mechanical Testing: Potted forearms were vertically aligned in a material testing system (MTS Bionix). We performed failure testing at 3mm/s onto the palm of the intact hand. Failure force was defined for each specimen.

FE Analyses: We converted radius images to FE models using manufacturer-provided FE software. For the standard model, we used a single elastic modulus (i.e., E=6.829 GPa) for bone tissue [2,4]. For the other model (E-BMD), we used imaged bone mineral density (BMD) to define elastic moduli for individual elements [4].

We used Pistoia's failure criteria for the standard model where failure occurs when 2% of the bone tissue exceeded an energy equivalent strain of 7000 μstrain [2]. The corresponding load at the critical strain limit represented the 'failure load' [2]. For the E-BMD model, we obtained a range of 'failure loads' using different failure criteria (i.e., stress or strain based) and percentages of strained tissue (i.e., 0.06%-7.5%).

Statistics: We assessed relationships between FE-derived and experimentally measured failure loads using linear regression. Based on the coefficients of determination, we identified the FE model and failure criteria that best predicted bone failure load. We also report root-mean-squared coefficient of variation ($CV\%_{RMS}$) to define precision errors for different FE estimates of failure load.

Results

The standard FE model explained 72% of variance in experimentally derived failure load. The E-BMD model explained 77% of variance in failure load when using an energy equivalent stress criteria with critical volume and critical stress limits set to 1.0% and 70 MPa, respectively. $CV\%_{RMS}$ was 3% and 2.6% for the standard and E-BMD models, respectively.

Conclusions

The E-BMD model, accounting for bone heterogeneity, appeared to predict 5% more of variance in in fracture load when compared to the standard FE model [2]. Also, precision errors appeared less for the E-BMD model compared to the STM model. Results indicate that E-BMD model may offer an attractive alternative to estimate distal radius failure load. E-BMD FE model may help to improve the assessment of distal radius fracture risk and improve monitoring efficacy of treatment and preventive therapies.

References

[1] Cuddihy et al., 1999; [2] Pistoia et al., 2002; [3] Kawalilak et al., 2016 [4] MacNeil & Boyd

Shear Stress and Nanoparticle Distribution in Zebrafish Blood Vessels

Branden Shin[1], Juliana Gomez[2], Hagar Labouta[2, 5], Bahareh Vadafar[3], Sarah J. Childs[6], Kristina D. Rinker[2,4,7]
[1]Biomedical Engineering Program, University of Calgary, [2]Cellular and Molecular Bioengineering Research Lab, [3]Zymetrix Lab, [4]Department of Chemical and Petroleum Engineering, [5]Department of Chemistry, [6]Department of Biochemistry and Molecular Biology, [7]Center for Bioengineering Research and Education
branden.shin@ucalgary.ca

INTRODUCTION

Nanoparticles have emerged as a powerful tool for both drug delivery and diagnosing diseases [1]. As most medical nanoparticles require vascular administration, it is important to understand how factors such as blood flow affect their distribution. After injection into the bloodstream, nanoparticles will target the cells lining the blood vessel (endothelial cells). As these endothelial cells are exposed to flow, they experience fluid forces such as wall shear stress. Previous studies have determined that areas of lower shear stress result in higher levels of nanoparticle accumulation [2].

This study explored the effects of vascular flow on nanoparticle distribution *in vivo.*

METHODS

Transgenic zebrafish embryos manipulated to express green and red fluorescence in their endothelial and red blood cells respectively were injected with a solution of marina blue stained liposomes. A 3D geometry of the vasculature is generated by collecting confocal images from the zebrafish and importing them into the software Simpleware ScanIP. Line scans were collected for particle image velocimetry of the red blood cells done in MATLAB to calculate the average velocity of the blood flow. The 3D vessel models were meshed and prepared to be imported into computational fluid dynamics (CFD) software Ansys FLUENT.

RESULTS

The average blood flow velocities for the dorsal aorta and the caudal vein are 246.25 ± 148.25μm/s and 497.96±290.64μm/s respectively. The dorsal aorta is characterized by straight, laminar flow with high wall shear stress, whereas the caudal plexus contains areas of disturbed flow with low shear stress. The relative nanoparticle accumulation per unit volume (μm^3) was determined to be 0.122 for the dorsal aorta, 0.336 for the ventral vein, 0.691 for the dorsal vein, and 1.0 for the capillaries. The results showed nanoparticle localization was affected by the vascular architecture and shear stress.

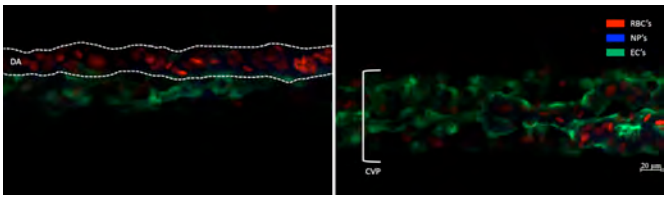

Figure 1: The figure shows images of the dorsal aorta (left) and the caudal venous plexus (right) of the embryo. The nanoparticle (blue) signal has a higher intensity in the plexus, indicating higher accumulation.

CONCLUSION

The results showed that shear stress has a significant impact on the distribution of nanoparticles in the bloodstream of the zebrafish embryos. The liposomes accumulated in areas of lower shear stress and altered architecture, showing that blood flow has an effect on nanoparticle distribution. In order to optimize medical nanoparticles for treatment or diagnostic techniques, we must understand the behaviour of such particles in the presence of blood flow.

REFERENCES

[1] Murthy, *Int J Nanomedicine*. **2**: 129-141, 2007.
[2] Jiang et al. *Nanomedicine.* **13**: 999-1010, 2017.

Quantitative magnetic resonance imaging (qMRI) of the meniscus in the knee joint in the unloaded and loaded conditions

Madeline Martel, Chelsey Thorson, Emily McWalter
Department of Mechanical Engineering, University of Saskatchewan, Saskatoon, SK

Introduction

Osteoarthritis is a disease that causes the meniscus in the knee to degrade, and lose function[1,2]. Quantitative magnetic resonance imaging (qMRI) is associated with biochemical composition of the meniscus[3], however, most work is carried out with tissues in unloaded, non-physiologic conditions. Thus, our objectives were to 1) design, build, and test an MRI safe loading device to apply load to cadaveric knee joints, and 2) develop custom software that compares meniscal qMRI parameters in the unloaded and loaded knee.

Methods

Our MRI safe loading device (Fig. 1) features an acrylic tube, and end caps held on to the tube with polyester straps which are locked and tightened using plastic buckles. Axial compressive load is applied to the specimen via four threaded rods that tighten into the tube against a disc. The disc presses down on the specimen, compressing it. An MRI safe load cell (Futek, Irvine, USA) at the back end measures the force applied. The planned procedure involves imaging cadaveric knee joints unloaded and loaded. Analysis of the qMRI parameters from the images will be carried out using custom software developed in MATLAB (the MathWorks, Natick, MA). The custom software collapses the 3D meniscus qMRI data into an axial plane. A circle is fit to the meniscus using a modified Taubin Circle Fit for radial division, and an ellipse is fit for circumferential divisions. The meniscus is then divided into radial and circumferential segments. A set of statistical parameters are calculated for each region; differences between regions and between the unloaded and loaded cases are determined.

Results

To date, the MRI safe loading device has been built and tested, and the qMRI analysis software has been created. An example of meniscal division by the software using test data is shown (Fig. 2). Validation testing of the loading device showed the maximum applied force to be ~200 pounds. Proof of concept was demonstrated by imaging a bovine carpal joint both unloaded and loaded. This project is ongoing.

Conclusions

The MRI-safe loading device is suitable for experimental use. The post-processing software allows for direct comparisons of unloaded and loaded qMRI data. In the future we will acquire unloaded and loaded qMRI data in human cadaveric knee joints.

References

[1] Herwig et al; 1984 Ann Rheum Dis; [2] Wilson et a. 2009 Arthritis Res Ther; [3] Son, M, et al. 2013 OA&C

Figures

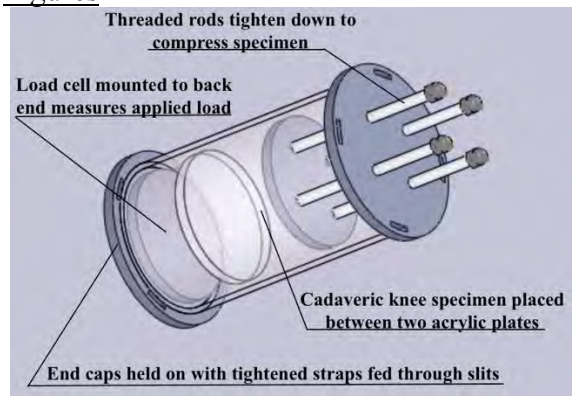

Figure 1: Model of MRI safe loading device

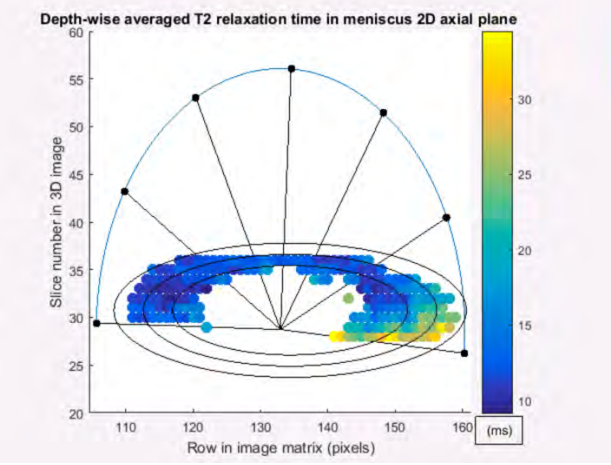

Figure 2: Meniscal regional division

Quantifying Asymmetry and Performance of Lower Limb Mechanical Muscle Function in Male and Female Varsity Soccer and Hockey Athletes

Meredith Stadnyk, Yvonne Qiu, Joseph Sabbagh, Eric Goldberg, Michael Cook, Samer Adeeb
University of Alberta, Edmonton, Alberta

Introduction

Muscle asymmetry is commonly found in athletes in various sports due to the preference of a dominant side of the body. Additionally, athletes from different sports can have substantial differences in their muscle performance. The objectives of this study were to: (1) create a mathematical tool to analyze force-time data outputted when subjects performed assessment jumps, (2) compare lower limb muscle performance of male and female athletes in varsity soccer and hockey programs, and (3) study muscle asymmetry between lower limbs.

Methods

This study sampled 11 varsity soccer players (8 female, 3 male) and 10 varsity hockey players (5 female, 5 male). Subjects performed 5 trials each of a non-counter movement jump (NCMJ) on dual force plates: subjects began on force plates, squatted down and held for 2 seconds to eliminate momentum, and then performed a jump. Capstone analysis software recorded the normal force as a function of time, and data was imported into Wolfram Mathematica. A Gaussian filter was used to smooth data, and a cubic spline interpolation function was applied to analytically describe normal force as a function of time. Using this function, the peak force, kinetic impulse, and phase length in eccentric and concentric jump phases can be obtained to allow for comparison of muscle function [1]. To allow for comparison, subjects were grouped into soccer versus hockey, and female versus male.

Results

Table 1 indicates the average peak force of each group, and Table 2 indicates the average kinetic impulse of each group.

Group	Avg. Peak Force (Left Leg), N	Avg. Peak Force (Right Leg), N	Peak Force Ratio (R/L)
Soccer (n=11)	773.9 ± 166.7	815.8 ± 175.9	1.05 ± 0.03
Hockey (n=10)	920.5 ± 164.0	940.1 ± 20.3	1.02 ± 0.05
Female (n=13)	722.1 ± 88.6	744.4 ± 88.5	1.03 ± 0.04
Male (n=8)	1041.3 ± 69.4	1087.2 ± 115.8	1.04 ± 0.05

Table 1: Average Peak Force

Group	Avg. Kinetic Impulse (Left Leg), N·s	Avg. Kinetic Impulse (Right Leg), N·s	Kinetic Impulse Ratio (R/L)
Soccer (n=11)	475.2 ± 168.9	444.7 ± 125.4	1.0 ± 0.2
Hockey (n=10)	446.5 ± 118.7	502.4 ± 192.7	1.1 ± 0.2
Female (n=13)	427.7 ± 164.9	407.9 ± 120.9	1.0 ± 0.2
Male (n=8)	516.6 ± 85.2	576.6 ± 165.8	1.1 ± 0.3

Table 2: Average Kinetic Impulse

The hockey group exhibited a greater peak force compared to the soccer group, and the male group exhibited a greater peak force compared to the female group. However, the hockey group exhibited greater kinetic impulse for the right leg, but not the left leg, compared to the soccer group. The male group exhibited greater kinetic impulse for both legs compared to the female group.

Conclusions

Kinetic impulse is equivalent to the area under the force-time curve [1]. When comparing groups, a similar kinetic impulse paired with one group having a larger peak force—such as the hockey group—suggests this group may have a more "explosive" jump rather a longer, less forceful jump. Future work includes the analysis of athletes of additional sports, as well as incorporating a counter movement jump and a 30-cm drop jump into the analysis. The mathematical model and methodology used can be used as a tool to assess lower limb injury rehabilitation as well as to enhance lower limb muscle performance in athletes.

References

1. Jordan, M.J. et. al. Lower limb asymmetry in mechanical muscle function: a comparison between ski racers with and without ACL reconstruction. *Scand J Med Sci Sports* 2015: 25: e301-e309.

Efflux Study of Cryoprotective Agents after Loading in Combination with Antioxidant Additives to Porcine Articular Cartilage

Kezhou Wu[1], Leila Laouar[1], Rachael Dong[1], Janet A. W. Elliott[2,3], Locksley E. McGann[3], Nadr M. Jomha[1]

1. Department of Surgery, University of Alberta, Edmonton, AB, Canada
2. Department of Chemical and Materials Engineering, University of Alberta, Edmonton, AB, Canada
3. Department of Laboratory Medicine and Pathology, University of Alberta, Edmonton, AB, Canada

Introduction

Cryoprotective agent (CPA) loading is an essential step in many cryopreservation protocols for various kinds of cells, tissues and bioproducts. Vitrification is an ice-free preservation process that requires high concentration of CPAs. High concentrations of CPAs may be toxic for the preserved samples (e.g. articular cartilage), thus antioxidant additives can be added into the CPA loading solution to mitigate oxidative injuries of CPAs. The objective of this study was to investigate CPA efflux after CPA loading in combination with antioxidant additives to porcine articular cartilage to determine if the additives have any effect on the permeation/efflux processes. We hypothesized that CPA loading with antioxidant additives would not disturb the CPA loading/unloading.

Methods

Healthy porcine knee joints from sexually mature pigs (killed for meat consumption) were collected from a slaughter house in Edmonton, Alberta, Canada. Femoral condyles were dissected, cleaned and randomly divided into four groups (N = 6). CPA cocktail solutions (concentrations from 6M to 9M) were prepared with dimethyl sulfoxide, ethylene glycol and propylene glycol. Three additives: ascorbic acid (AA: 2000 μM), chondroitin sulfate (CS: 0.1 mg/ml), and glucosamine (GlcN: 400 μM) were added to all the CPA solutions respectively. A control group was exposed to CPAs without any additive. After a stepwise CPA loading procedure for 310 mins, 10 mm diameter full thickness cartilage disks were shaved off the bone. Cartilage disks were then immersed in 10 ml PBS (1X) and the osmolality of the PBS washing solution was recorded using an Osmette™ Micro-Osmette Osmometer at different time points as a measure of efflux[1]. After 30 minutes, the cartilage was immersed in a second fresh PBS washout solution for a further 30 minutes and osmolality recorded. ANOVA and post hoc tests were used to analyze data with SPSS 20.0 software.

Results

CPA efflux rates were similar in the three experimental groups and the control group. After 30 min efflux in the first washout, there were no statistically significant differences ($p = 0.879 > 0.05$) in the measured total osmolality (Mean ± SE) (ΔOsmolality (mOsmol/kg) / mL articular cartilage disk (mOsmol/kg*mL)) of the washout solutions among the control group and AA, CS and GlcN groups. At the end of the second 30 min efflux, again there were no statistically significant differences ($p = 0.853 > 0.05$) in the osmolality changes among the control, AA, CS and GlcN groups.

Conclusions

This study showed that the permeation and efflux kinetics of CPAs in combination with antioxidant additives in porcine articular cartilage were similar to those of CPAs when used alone. This is an important finding that CPA loading with additives does not affect CPA permeation and efflux, which might be helpful in optimizing the vitrification of articular cartilage.

References

1. Yu. H, KK Al-Abbasi, JAW Elliott, LE McGann, NM Jomha. "Clinical efflux of cryoprotective agents from vitrified human articular cartilage." Cryobiology 66, no. 2 (2013): 121-125.

Dynamic Contrast-enhanced (DCE) MR Imaging: A Promising Approach to Differentiate True Cancer and Pseudo Progression in Glioblastoma Patients

Fatemeh Rezapoor,[1,4] Linda B Andersen,[2,4] Robert J Sevick,[2-4] R Marc Lebel,[1,2,4,5] Richard Frayne[1-4]
[1]Biomedical Engineering, [2]Radiology and [3]Clinical Neurosciences, Hotchkiss Brain Institute, University of Calgary;
[4]Seaman Family MR Centre, Foothills Medical Centre, and [5]General Electric Healthcare, Calgary, Alberta

Introduction

Glioblastoma multiforme (GBM) is a common and aggressive primary brain tumor in the central nervous system. Post-treatment care involves multiple magnetic resonance (MR) imaging scans over time. However, in some patients, conventional MR imaging does not provide adequate information to discriminate between true cancer progression (TP) and treatment induced damage (or pseudo progression, PP). A limitation in conventional MR imaging derives from the contrast agent extravasation due to blood brain barrier (BBB) disruption. As a result, TP and PP can appear quite similar and may be undistinguishable on post-contrast T1-weighted (T1-w) MR images.[1] We are evaluating the role of dynamic contrast enhanced (DCE) MR imaging to distinguish TP from PP. A high-resolution DCE MR imaging sequence[2] has been developed that characterizes both tissue perfusion and vessel wall permeability. We hypothesize that changes in perfusion and permeability measures will provide sensitive biomarkers that differentiate TP from PP.

Methods

We are in the first year of a three-year longitudinal study of GBM post-treatment. To date, 16 patients have been scanned (each between 1 and 5 sessions; 33 total examinations). High-resolution, full-brain permeability and blood volume maps have been generated for all patients.

Results

Figure 1(a)-(d) present pre- and post-contrast T1-w scans, permeability and blood volume maps, respectively, for the same patient. Figure 1(e) shows typical MR signal intensity *vs* time curves for GBM, healthy tissue and an arterial region. The GBM region has a differing behavior compare to healthy tissue and arterial signal. The GBM signal continues to increase with time, likely due to increased wall permeability. This difference in signal behavior may provide a robust indication of GBM-related BBB disruption and can help differentiate normal and cancer tissues.

Conclusions

Our advanced DCE MR technique has the potential to improve cancer management post-treatment, ultimately improving quality-of-life by preventing unnecessary surgeries or stopping ineffective treatments, while providing a quantitative biomarker for future clinical trials. We are planning to extend our qualitative findings and use a variety of quantitative analysis methods including region-based analyses to determine characteristic spatial features of our quantitative perfusion and permeability imaging sequence, in order to better discriminate TP from PP.

References

1. Eilaghi, AE, *et al*. Quantitative perfusion and permeability biomarkers in brain cancer from tomographic CT and MR images. *Biomarkers in Cancer* 2016; **8**: 47.
2. Lebel, RM, *et al*. The comprehensive contrast-enhanced neuro exam. *Proc. ISMRM* 2015: 3705.

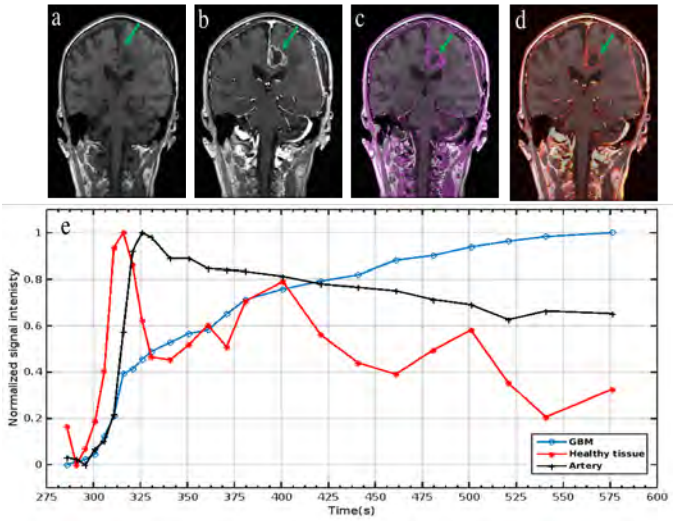

Figure 1: *(a) pre-contrast T1-w image, (b) post-contrast T1-w image, (c) permeability map, (d) perfusion map, and (e) representative signal intensity vs time curves for GBM (arrow). healthy tissue, and an artery. Curves are scaled independently.*

IMPROVING EEG SIGNALS WITH GEOPHYSICAL PROCESSING METHODS

Julie A. Aitken[1], Elise Fear[2] and Andrea Protzner[3,4]

Biomedical Engineering Graduate Program[1], Department of Electrical Engineering[2], Department of Psychology[3], and Hotchkiss Brain Institute[4], University of Calgary

Introduction

An electroencephalogram (EEG) measures and records neural activity using a series of electrodes placed on the scalp. Differences in neural voltages across the cerebral cortex can be observed and localized to study functional relationships in the brain [1]. When a participant is engaged in a visual recognition task, these neural responses can be segmented into waveform components called event-related potentials (ERPs). ERPs are embedded in the EEG signal and characterization of these responses requires the repetition of stimuli and averaging across many trials to allow for the segregation, quantification and measurement of its distinct waveform. In language tasks, different stages in neural temporal processing occur and correlate directly with features of the ERP (referred to as N170 and P300 components). Key measurements of these components include amplitude, area and latency. These measurements are complicated by detrimental noise arising from non-related biological artifacts such as skin potentials, eye movement, or from electrical interference [2]. A key challenge for noise removal is that both artifact and electronic noise require different preprocessing techniques to attenuate their effects. Whereas Independent Component Analysis (ICA) is used to isolate and eliminate artifact noise, random noise must be removed using data preprocessing techniques such as averaging, filtering or noise attenuation. The second challenge is that, since the signal-to-noise ratio (SNR) remains an issue, numerous participants or multiple trials are needed to accurately infer behavioral responses. The effect of noise is therefore a critical issue in EEG recordings, specifically in the integrity and extraction of an ERP. To improve SNR, we plan to enhance standard EEG preprocessing by developing signal processing tools adopted from geophysical exploration. EEG and seismic signal analysis bear similar characteristics in terms of the total frequency band, the necessity for filtering unwanted noise, and the enigma of an "unknown" source wavelet inherent in the data. By integrating this synergy, the objective is to highlight the brain signal, minimize measurement noise and isolate key metrics of the ERP components.

Methods

The new geophysical preprocessing flow will be tested on a simulated ERP dataset. We investigate new ways to tackle noise through the adaptation and application of different Butterworth and Ormsby filters, amplitude enhancement techniques, and deconvolution [3], directed across the delta, theta and alpha frequency bands: 0.1 - 13 Hz. The simulated dataset allows for the testing and comparison of the standard preprocessing EEG typically employed in the Brain Lab, with individual processes, and a combined geophysical preprocessing flow, to determine their effect on the ERP waveform. This dataset also enables preliminary investigation of whether decreasing or increasing the number of participants or trials effects the integrity of the ERP waveform for both preprocessing flows.

Conclusions

Adaptation of geophysical preprocessing techniques to EEG has shown promise in earlier work on resting-state EEG, specifically increased power in the lower, and relevant frequency bands. Establishing a multidisciplinary EEG signal processing flow to elicit key brain ERP metrics related to cognition will serve as a guideline for future psychological and clinical research.

References

1. van Hees, S., et al., *Frontiers in Human Neuroscience,* 2016. **10**(NOV2016).
2. Luck, S., J., *An Introduction to the Event-Related Potential Technique*. 2005, Cambridge, Massachusetts, USA: The MIT Press. 374.
3. Abutaleb, A., A. Fawzy, and K. Sayed. *2012 Cairo International Biomedical Engineering Conference, CIBEC 2012*. 2012.

Improved Harvest of Equine Cord Blood Mesenchymal Stem Cells from Microcarriers in Stirred Suspension Bioreactors

Tiffany Dang[1], Erin Roberts[1,3], Thomas G Koch[4], and Michael S. Kallos[1,2,3]

[1]Pharmaceutical Production Research Facility, [2]Department of Chemical and Petroleum Engineering, Schulich School of Engineering, [3]Biomedical Engineering Graduate Program, University of Calgary, 2500 University Drive NW, Calgary, AB, CANADA T2N 1N4

[4]Department of Biomedical Sciences, Ontario Veterinary College, University of Guelph, Gordon St., Guelph, ON, CANADA, N1G 2W1

Introduction

Musculoskeletal injuries are the leading causes of lameness and loss of performance in horses [1]. One potential treatment is the use of equine cord-blood derived mesenchymal stem cells (eCB-MSCs) due to their high proliferation potentiation, immunomodulatory properties and chondrogenic potential [2]. The promise of these cells is currently hampered by the inability to grow them into the high numbers required for multicenter clinical studies and commercial product development. However, by culturing the cells on microcarrier beads in stirred suspension bioreactors, it allows for extensive cell expansion. The aim of this project was to develop and optimize a removal protocol for eCB-MSCs from microcarriers at the end of the bioprocess.

Methods

Using 10 mL and 100 mL stirred suspension bioreactors, eCB-MSCs obtained from our collaborators at the University of Guelph, were expanded on microcarriers. The effects of enzyme type and exposure time were determined by exposing samples obtained from 100 mL bioreactors to 0.05% and 0.25% trypsin, Accutase, TrypLE or TrypZean for a total of 15 minutes. 10 mL bioreactors were used to determine the effects of agitation rate and regime following enzyme treatment. Optimized criteria were scaled up for full harvest in 100 mL bioreactors. The scaled-up agitation rate was determined using the volume average energy dissipation rate for a 100 mL bioreactor. Harvesting efficiencies and viabilities were determined using the trypan blue exclusion assay and nuclei counts.

Results

It was found that 0.25% trypsin optimized a high viable cell yield following 9 minutes of exposure. Harvesting efficiencies of 0.05% trypsin, 0.25% trypsin, Accutase, TrypLE, and TrypZean were determined to be 11%, 44%, 35%, 35% and 27% respectively with comparable viabilities (Figure 1). The use of continuous agitation for 9 minutes at 80 rpm removed the most cells in 10 mL bioreactors. Finally, 0.25% trypsin with 9 minutes of agitation at 80 rpm resulted in 75% harvesting efficiency and 95% viability in 100 mL bioreactors.

Conclusions

Continuous agitation for 9 minutes with 0.25% trypsin resulted in high viable cell yields. The results of this project will not only contribute in developing a scalable harvesting protocol for eCB-MSCs but for other cell lines grown from microcarriers.

References

[1] Koch et al. *BMC Biotechnol.* **7**:26, 2007.
[2] Russell et al. *PLoS One.* **10**:1-3, 2015.

Figures

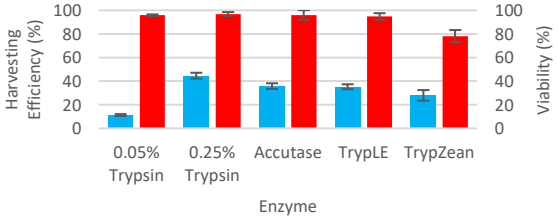

Figure 1: The harvesting efficiency (blue) and viability (red) of different enzymes

A Simple Approach to Designing a Subtalar Joint Loading Simulator

Jonelle M Jn Baptiste[1], Joseph Sabbagh[2], Stephen HJ Andrews[3], Julia Bowes[3], Nadr M Jomha[3], Samer Adeeb[1]
1 Department of Civil Engineering, 2 Department of Mechanical Engineering, 3 Division of Orthopaedic Surgery, Faculty of Medicine & Dentistry, University of Alberta, Edmonton, AB

Introduction

The development of subtalar joint prostheses is a novel approach to supersede subtalar arthrodesis. Arthrodesis of a joint alleviates pain but eliminates articulation. Since successful cases of ankle joint replacements have been recorded, it may be possible for prostheses to maintain some subtalar joint motion in addition to reducing joint pain. To date, no standards on the wear testing of subtalar joint prostheses exist. Therefore, standards for wear testing of total hip-joint prostheses [1] were used to develop the loading conditions that the subtalar joint implants would be subjected to. The objective of this research is to develop a flexible test setup that enables the experimenter to apply double actuation to possible subtalar joint implants made from various materials.

Methods

The proposed subtalar joint prostheses replicate the mating surfaces of the talus and calcaneus bones. Prostheses are generally subject to cyclic loading and rotary displacement for wear testing. For this experiment, a four-bar crank rocker mechanism provides +/- 10 degrees rotary displacement while a fatigue-testing machine provides 50-800 N cyclic compressive load. To simulate physiological conditions, the implants are submerged in 20 g/l bovine serum diluted with deionized water during testing. The implants will be subject to these loading conditions for 5 million cycles at a rotary frequency of 3 Hz. After 500,000 cycles, 1 million cycles and every 1 million cycles thereafter, the implants will be tested for wear gravimetrically. The surfaces of the implants will also be inspected using scanning electron microscopy (SEM). Finite Element Analysis (FEA) determined the input torque required to drive the four-bar mechanism under the applied load and a suitable cross section for the linkages to withstand at least 1 million cycles without failure from fatigue. A dynamic force analysis was done to confirm the input torque calculated from FEA. The other mechanical components of the setup were designed according to standards. For initial testing, 3D printed implants are used to ensure that the setup functions properly.

Results

Using FEA to determine the size of the motor required and suitable dimensions of the linkages necessary to withstand at least 1 million cycles without failure from fatigue proved successful. After finalizing the design and procuring all the parts, the simulator was assembled (Figure 1). Adjustments were made to rectify design and manufacturing errors.

Conclusion

Preliminary testing with 3D printed implants proves that the design of the simulator is successful. In the future, the actual subtalar joint implants will be tested for wear under the prescribed conditions.

References

1. BS ISO 14242-1:2014 *Implants for surgery. Wear of total hip-joint prostheses. Loading and displacement parameters for wear-testing machines and corresponding environmental conditions for test.* (2014). BSI Standards Limited.

Figures

Figure 1. Isometric and front views of subtalar joint simulator

Investigating Sagittal Plane Lower Limb Kinematics in Children and Adolescents with Juvenile Idiopathic Arthritis

Scholz R, Kuntze G, Esau S, Nesbitt C, Brooks J, Mosher D, Benseler S, Emery CA
Faculties of Engineering and Kinesiology, University of Calgary

Introduction

Juvenile Idiopathic Arthritis (JIA) affects ~ 3 in 100 youth < 18 years[1] and is characterized by joint swelling, pain, stiffness, weakness, and fatigue[2]. Current evidence indicates alterations in lower limb mechanics in patients with JIA[3]. However, little information is currently available on the consequences of JIA on musculoskeletal aspects of walking and running[4]. The aim of this research was to quantify differences in the biomechanics of walking and running in children and adolescents with JIA. The hypothesis was that participants with JIA show alterations in sagittal plane kinematics compared to normally developing children during walking and running.

Methods

Twenty-five participants with JIA [JIA; female n=17; median age=14.72 (range 10-20 yrs); mean weight=58.62 (95%CI; 52.82-64.37 kg) and 24 participants with no history of JIA [CON; female n=15; median age=15.77 (range 10-19 yrs); mean weight=53.95 kg (95%CI; 48.94-58.96 kg)] volunteered for participation in this study. Ethics approval was received by the local ethics boards. Participants were fitted with 32 reflective markers placed on the lower limbs and pelvis. Participants walked at 1.3ms^{-1} and ran at 2.5ms^{-1} on a motorized treadmill (Woodway, USA). Kinematics data were recorded using a 12-camera motion analysis system (Motion Analysis, USA, 240Hz). Heel strikes were recorded using a one-axis accelerometer (PCB, USA, 2400Hz). Data were processed in Evart 5.0.4 (MA, USA) and Visual3D (C-Motion, USA). Data were processed using custom written code in Matlab (v2016b, Mathworks, USA). All participant data were time normalized to stride duration (101 data points from heel strike to consecutive heel strike). Statistical analyses of sagittal plane hip, knee and ankle kinematics were conducted using Statistical Parametric Mapping at alpha 0.05, (www.spm1d.org) in Matlab.

Results

The results of this study did not support the hypothesis. No significant differences in sagittal plane kinematics were observed between JIA and CON groups at the hip, knee and ankle during walking or running.

Conclusions

In contrast to current research evidence[3,5], participants with JIA in this cohort did not appear to experience significant alterations in sagittal plane lower limb kinematics during controlled speed treadmill walking and running. These findings may be regarded as an indication of an efficacious clinical management of JIA for participants in this study. Further work is currently ongoing to investigate lower limb kinematics in the coronal and transverse planes. In addition, multi-muscle electromyography data, collected as part of this investigation, will be analyzed to investigate potential neuromuscular alterations that may persist despite apparently normal movement mechanics.

References

1. https://arthritis.ca/understand-arthritis/types-of-arthritis/childhood-arthritis
2. Hansmann S, Benseler SM, Kuemmerle-Deschner JB. Dynamic knee joint function in children with juvenile idiopathic arthritis (JIA). Pediatr Rheumatol Online J 2015;13:8.
3. Hartmann et al. (2010). Effects of Juvenile Idiopathic Arthritis on kinematics and kinetics of the lower extremities call for consequences in physical activity recommendations. Int Journal Ped. DOI: 10.1155/2010/835984
4. Kuntze et al. (2017). Exercise therapy in Juvenile Idiopathic Arthritis: A systematic review and meta-analysis. Arch Phys Med Rehabil. DOI 10.1016/japmr.2017.05.030.
5. Frigo et al. (1996). Gait alteration in patients with juvenile chronic arthritis: A computerized analysis. Journal of Orthopaedic Rheumatology. 1996:08:05.

The effects of meniscal damage on bone microarchitecture in anterior cruciate ligament reconstructed knees 5 years after reconstructive surgery

Andres Kroker [1,2], Denise Chan [3], Sarah Manske [1,2], Nick Mohtadi [1,2,3], Steven Boyd [1,2]
[1] McCaig Institute for Bone and Joint Health; [2] Department of Radiology, Cumming School of Medicine; [3] Sports Medicine Centre, University of Calgary

Introduction

Anterior cruciate ligament (ACL) tears are a common sports-related knee injury associated with an increased risk of developing osteoarthritis (OA) [1]. ACL tears do not commonly occur in isolation but rather in conjunction with other soft tissue injuries such as meniscus injuries [2]. Depending on injury severity, menisci can be treated with meniscal repair or meniscectomy (partial or total resection of menisci). Meniscus injuries and meniscectomy are a frequently identified risk factor for OA development following ACL tears [3]. While previous studies used radiographs or self-administered questionnaires to identify radiographic and symptomatic OA [4,5], no previous studies have investigated the underlying changes in bone microarchitecture that are associated with meniscal damage in these knees. In this study we investigate differences in bone micro-architecture between ACL reconstructed (ACLR) knees with meniscal injury compared to ACLR knees without meniscal damage using high-resolution peripheral quantitative CT (HR-pQCT).

Methods

28 individuals (13 female, 15 male) with unilateral ACLR knees 5.2 years prior to imaging were recruited and divided into groups depending on meniscus injury severity: a. no-meniscal treatment (n=5); b. meniscal repair (n=11); c. meniscectomy (n=12). Bone microarchitecture of the distal femur and proximal tibia weight-bearing regions were assessed in each condyle using HR-pQCT, including the subchondral bone plate (density, thickness), and trabecular bone at different depths (density, thickness, separation, number) [6]. Both the ACLR and uninjured contralateral knees were imaged, and the percent-difference between each pair was determined for each bone parameter. Kruskal-Wallis tests with Mann-Whitney-U post-hoc tests were performed to identify differences in bone parameters between groups.

Results

Differences in bone microarchitecture percent-difference between meniscal treatment groups were found only in the femur. Trabecular density increased at all depths in the lateral condyle in the meniscal repair group as compared to the no-treatment group (9.1-10.2%, $p<0.05$). This was accompanied by a near-significant increase in trabecular thickness in the meniscal repair group as compared to the no-treatment group (6.4-12.6%, $p<0.1$).

The thickness of the lateral subchondral bone plate increased in both the meniscal repair and meniscectomy groups as compared to the no-treatment group (26.4%, $p<0.05$), though density did not differ between them.

Conclusion

Individuals who receive meniscal repair exhibit increased trabecular bone density in the lateral femur 5 years post-surgery. While trabecular thickness increases in the lateral femur were not significant, trabecular bone deposition could explain the increase in density in the meniscal repair group. The small sample size may have resulted in lack of statistical power to detect a difference in thickness, which was near-significant.

Increased subchondral bone plate thickness, similar to OA-related bone sclerosis, could be an indicator for future OA risk in the injured knee. Similarly, bone turnover rate is altered in the femur in OA knees, and changes in trabecular density and structure could be related to future disease development. A longitudinal study would be required confirm the relevance of these bone changes to future OA risk.

References

1. Lohmander et al. *Am J Sports Med*. 2007;
2. Meunier et al. *Scand J Med Sci Sports*. 2007;
3. Oiestad et al. *Am J Sports Med*. 2009; 4. Aglietti et al. *Clin Orthop*. 1994; 5. von Porat A. *Ann Rheum Dis*. 2004; 6. Kroker et al. *Bone*. 2017

Implementation of Electromechanical Controls for Agitation Rate in a Bioreactor System

James Colter[1,3], Breanna Borys[1,3], Michael Kallos[1,2,3]

[1]Pharmaceutical Production Research Facility, [2]Department of Chemical and Petroleum Engineering, Schulich School of Engineering, [3]Biomedical Engineering Graduate Program, University of Calgary, 2500 University Drive NW, Calgary, AB, CANADA T2N 1N4

Introduction

Bioreactor designs have become of increasing necessity for the translation of laboratory based culture protocols to effective, reproducible, and scalable bioprocesses [1]. Implementation of a micro scale bioreactor system with the capacity to produce shear stress profiles like those of larger scale stirred suspension bioreactors could allow for immediate expansion and scale-up following initial cell harvest [2]. Electromechanical controls were designed and implemented to control agitation rates in 1-3 mL vessels, to study shear stress and cell behavior in a micro bioreactor system.

Methods

A custom electromechanical system was designed to provide precise control over agitation rate. Sub-systems were designed to facilitate power conditioning, digital processing, and digital-to-analog conversion of signals to drive the system. A user interface was implemented using a custom USB driver derived from Microchip's USB Framework for PIC microcontrollers. Python programs were written in a Linux environment to facilitate user control. The system was tested under standard environmental conditions to verify operational readiness at 100 RPM over 44 hours, and 150 RPM over 25 hours. Murine embryonic stem cell (mESC) aggregation was also tested over 12 hours to study growth potential of the bioreactor.

Results

Over 45 hours at 100 RPM, a mean agitation rate of 100.006 RPM with standard deviation of 0.319 were calculated. For 25 hours at 150 RPM, a mean of 149.978 RPM was observed, with a standard deviation of 0.302. Cell aggregate formation was observed 12 hours after mESC inoculation in the bioreactor.

Conclusions

Implementation of the electromechanical controls for operation of the bioreactor was successful. Digital communication between the user and control system allowed for changing and maintaining agitation rates, programming behavior over time in the bioreactor, and data-logging of agitation rates. mESCs exhibited aggregate formation in the bioreactor, suggesting cell growth and suitable conditions for proliferation.

References

[1] D. Wang et. al., "The bioreactor: A powerful tool for large-scale culture of animal cells," *Current Pharmaceutical Biotechnology,* vol. 6 (5), pp. 397-403, 2005.

[2] N. Tandon et. al., "Bioreactor engineering of stem cell environments," *Biotechnology Advances,* vol. 31 (7), pp. 1-26, 2013.

Figures

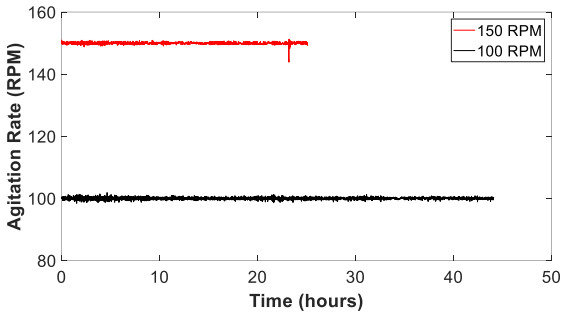

Figure 1. System stability at 150 RPM (red) and 100 RPM (black).

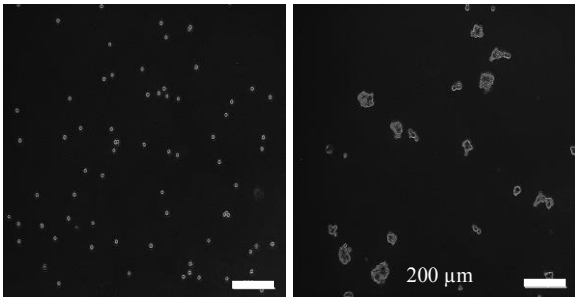

Figure 2. Cells after seeding (left) and aggregate formation in parallel vessels after 12 hours in stirred suspension (right).

Evaluation of distal femoral subchondral bone mineral density using quantitative computed tomography in patients with knee osteoarthritis

[1]Najafi Semnani A; [1]Burnett,WD; [1]Arjmand H: [2]Wilson DR; [3]Hunter DJ; [1]Kontulainen SA; [1]Johnston JD
[1]University of Saskatchewan, [2]University of British Columbia, [3]University of Sydney

Introduction: Knee osteoarthritis (OA) is a debilitating and painful joint disease, and the leading cause of pain and disability in the elderly. In addition to cartilage changes, the disease is commonly characterized by (underlying) subchondral bone changes, including altered subchondral thickness, bone mineral density (BMD) as well as the presence of cysts. These alterations are thought to be involved in the OA pain process, with recent studies showing links between knee joint pain and low BMD at the proximal tibia [1,2] and patella [3]. However, the relationship between joint pain and subchondral bone features at the distal femur has not yet studied, partly due to lack of validated imaging methodology able to qualify bony features at the distal femur.

Using quantitative computed tomography (QCT) imaging and novel image processing algorithms, the objectives of my MSc research are as follows:

1. Develop an image processing method for assessing subchondral bone features of the distal femur, including depth-specific measures of subchondral bone density, epiphyseal trabecular bone density, and cysts characteristics
2. Determine precision (repeatability) errors of derived subchondral bone features of the distal femur
3. Examine relationships between clinical symptoms of osteoarthritis (disease severity, knee pain) and derived subchondral bone features of the distal femur

Methods: *Objective 1:* For analyzing depth-specific measures of subchondral bone, I will develop a variation of imaging processing methods developed by Johnston et al [4], Speirs et al [5] and Wright et al [6]. This method will account for curvature of the distal femur. For analyzing epiphyseal trabecular bone and cyst presence, I will manually segment these regions. I will use Matlab to conduct regional analyses of these features across the distal femur.

Objective 2: Fourteen participants (2 men and 12 women; mean age 51.4, SD 11.8 years) were previously scanned using clinical QCT three times over 2 days. Participants were categorized as either normal (n = 7) or exhibiting radiographic OA (n = 7). I will assess the precision of distal femur subchondral bone features using root mean square coefficients of variation (CV%) [7].

Objective 3: The preoperative knee of 42 participants (17 men and 12 women; mean age 64, SD 10.1 years) scheduled for knee arthroplasty was previously scanned using QCT. These participants were scored for pain using the Western Ontario and McMaster Universities Arthritis Index (WOMAC) [8] and were classified for OA severity using Kellgren-Lawrence scoring [9]. As well, they were assessed for medial and lateral joint space narrowing (JSN) and joint alignment. These clinical symptoms will be related to subchondral bone features of the distal femur acquired with my imaging technique using statistical correlation analyses (Pearson, Spearman rank).

Results: The research is currently ongoing. Methodologies are currently being established.

Anticipated Conclusions: A better understanding of pain pathogenesis is crucial for preventive and therapeutic targeting [10]. Further, as pain is the reason patients seek medical care, rational treatment targeting requires specific understanding of which structures contribute to pain [10]. This research will strive to clarify the role of bone in OA-related pain. As well, findings may be valuable in guiding outcome selection in OA studies addressing subchondral bone and pain, particularly in determining regions of interest for future prospective studies.

References: [1] Burnett et al., 2017; [2] Burnett et al., 2015; [3] Burnett et al., 2016 ; [4] Johnston et al., 2009; [5] Speirs et al., 2013; [6] Wright et al., 2012; [7] Gluer et al., 1995; [8] Bellamy et al., 1988 [9] Kellgren & Lawrence 1957 [10] Neogi 2012

Design of a new Dynamic Microfluidic Separation System for Exosome Isolation

Sara Hassanpour-Tamrin[1], Amir Sanati-Nehzad[1,2], Arindom Sen[1,2]
1. Biomedical Engineering Graduate Program, 2. Schulich School of Engineering
University of Calgary, 2500 University Drive NW, Calgary, Alberta T2N 1N4

Introduction

Extracellular vesicles are a group of structures which are released by cells, and can be found in all bodily fluids. Exosomes (40-120 nm) are a type of vesicle, that contain genetic information and play an important role in intercellular communication. As an analysis of exosome content has been shown to reliably differentiate between diseased and healthy states, the isolation of a pure population of exosomes would facilitate studies in exosomes physiological functions and their roles in various pathologies. However, there is a need for new technologies to isolate pure exosomes from other vesicles [1].

Compared with current widely-used conventional methods for exosome isolation, microfluidic-based separation technologies have shown great potential for achieving fast exosome separation from biological samples with high purity and recovery, as well as enabling on-chip detection and analysis [2]. Despite the exciting progress in microfluidic-based systems for exosome isolation, this technology is still limited by several factors, such as photolithography fabrication and surface bonding processes, indicating the importance of further developing microfluidic devices for the efficient isolation of pure exosomes from bio-fluids [2]. In this study, we propose an integrated multi-filtration microfluidic device in combination with an external electrical force to isolate and enrich exosomes from a mixture of various particles and contaminants.

Methods

The device was designed as an open crossflow channel in which two track-etched polycarbonate (PCTE) membranes (200 and 30 nm pore size) sandwiched between poly (methyl methacrylate) (PMMA) layers (five layers,1.5 mm thick) with the aid of double sided adhesive (DSA). Aluminum layers were used as the electrodes to apply electric filed using a DC power supply. The sample and buffer solutions were infused at different flow rates; here, plastic tubes were connected to apply flow-rate driven flows by a syringe pump. Based on the principle of size-exclusion, membranes with pore sizes of 200 and 30 nm were used to fractionate and enrich particles within this size range; particles larger than 200 nm are excluded by the membrane with a pore size of 200 nm in the sample chamber, whereas particles smaller than 30 nm filtered out to a waste chamber (Figure1.). To enhance particle mobility, an electric field was used.

Results

The efficiency (in terms of purification and quantification) of the proposed approach was compared to given subsets in a reference database. The two modes of separation (pressure mode and electrical mode) were also compared, and an analysis was conducted to determine the potential of using external electric fields to improve desired exosome isolation.

Conclusions

Electrical fields can influence exosome separation by exerting electrophoretic forces on the particles, as well as improving the size-based separation of particles, indicating the potential of our proposed system for providing an effective platform to isolate exosomes efficiently (size uniformity and purity in isolated outcome).

References

1. Barile, L, et al. Pharmacology and Therapeutics 174, 63–78 (2017).
2. Salafi, T, et al. Lab Chip 17, 11–33 (2017).

Figure

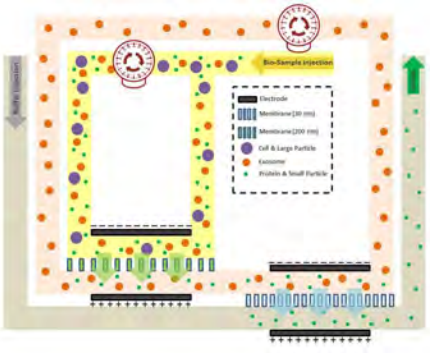

Fig.1. Schematic of the proposed microfluidic method for exosome isolation

DTI histogram skewness distinguishes recently concussed youth from recovered and control subjects

Najratun Nayem Pinky, Kassondra Pedenko, Carolyn Emery, Chantel Debert, Bradley Goodyear
Biomedical Engineering, Depts of Radiology, Pediatrics, Clinical Neurosciences, Community Health Sciences
University of Calgary

Introduction

The structural integrity of white matter tracts of the brain can be inferred by quantifying the directional preference of water motion, using fractional anisotropy (FA); a whole-brain map of FA is derived from diffusion tensor imaging (DTI) data. Several FA studies of concussed individuals have observed decreases in FA and suggest that white matter injury is present [1]; however, the success of such studies are limited success due to limitations of current analysis approaches. Whole-brain analysis of FA relies on the assumption of a common site of injury across a subject group, which is unlikely in case of concussion. In addition, detecting a significant difference between concussed and control subjects in the mean of FA over an entire tract relies on a relatively large number of FA pixels being different between groups. Alternatively, the shape of the FA distribution for a tract (e.g., quantified by skewness) can change significantly with fewer pixels, regardless of their location within the tract. We therefore hypothesized that FA skewness can distinguish recently concussed youth from recovered and control.

Method:

Forty-eight youth players (18 recently concussed, 15 recovered and 15 controls) were recruited. DTI was performed using a 3 Tesla GE Discovery MR750 scanner. After motion and eddy current correction and brain extraction of the raw images, FA maps were calculated for each participant. FA maps for all subjects were registered to the standard MNI brain template. Using a standard white matter atlas, 16 major tracts were identified, and a histogram of FA values was generated by sorting FA pixels within each tract into 40 equal width bins. Skewness was then calculated for each tract, for each participant. Between-group differences in FA skewness were tested for each tract using an analysis of variance (ANOVA).

Results

Table 1 summarizes white matter tracts that exhibited a significant difference in FA skewness between groups; Figure 1 shows tract location. Follow-up tests showed that the recently concussed group significantly differed from the recovered and healthy control groups.

Table 1. Tracts exhibiting significant between-group differences in FA skewness

Tract	***F (x,x)***	***p value***
L corticospinal	4.3	.019
R corticospinal	3.5	.037
L temporal superior longitudinal fasciculus	7.7	.001
L superior longitudinal fasciculus	9.8	.000
R inferior longitudinal fasciculus	14.3	.000
R inferior fronto occipital fasciculus	4.4	.017
Forceps major	16.8	.000

Conclusions

FA skewness successfully identifies white matter tracts with decreased structural integrity following concussion. Our results also suggest that integrity returns with recovery. FA skewness may therefore be a useful tool in assessing concussion recovery, and may also help identify brain mechanisms responsible for prolonged symptoms often reported by concussion sufferers.

Reference:

[1] A Systematic Review of Diffusion Tensor Imaging Findings in Sports-Related Concussion, Gardner et. al. J Neurotrauma, 2012, (2521-38)

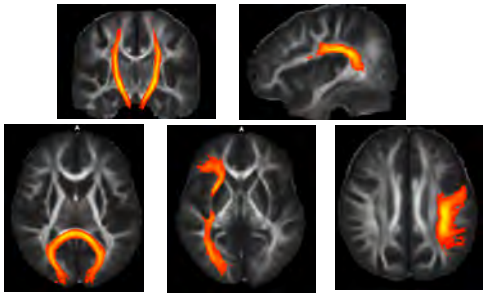

Figure 1: White matter tracts exhibiting altered FA skewness in the recently concussed: (clockwise from top left) bilateral corticospinal, left temporal superior longitudinal fasciculus, left superior longitudinal fasciculus, right inferior fronto occipital & longitudinal fasciculus, forceps major.

Creating Microfluidic Device for Cell Analysis

Pavey Gill[1], Douglas Kondro[2], Mark Ungrin[3]
[1]Schulich School of Engineering, [2]Graduate Program of Biomedical Engineering, [3]Department of Comparative Biology and Experimental Medicine, University of Calgary

Introduction

Microfluidics has been a quickly-growing area of research since its advent in the 1990s. The ability to manipulate fluid flow in channels with sub-millimeter dimensions provides a number of advantages in experimentation such as cost, time, and reproducibility. The use of microfluidics in biological applications is particularly interesting, as the smaller scale allows for more precise control of cells' microenvironment. The goal of this project was to create a PDMS-based microfluidic device that could accommodate a membrane with cells on it. The cells on the membrane would be subject to apical and basal flow of different nutrients, growth factors, and media. The main application of the device will be to study the migration and differentiation of embryonic stem cells. By seeding stem cells with nuclear markers onto one side of a porous membrane and perfusing media above and below the membrane, the cells can be tracked proliferating and migrating across the membrane in response to the different factors being perfused in the apical and basal channels. This will provide a better understanding of what causes stem cells to choose the fates that they do in early embryonic development.

Methods

Using a laser-cutter, a channel design can be cut into Kapton tape, which is a polyimide tape of a precise known thickness on the order of tens of microns. PDMS can then be cast on top of the Kapton tape channel design. After the PDMS has cured, it can be peeled off and it will have a channel in it with the same depth as the thickness of the tape that it was cured on top of. This simple principle was used to create a PDMS-based device that accommodated a circular membrane with flow channels above and below it.

Results

To seal the device, a mechanical clamp with screws was used. It has an acrylic lid and an aluminum body. The device was placed inside the clamp and the screws were tightened. For testing, red dye was perfused into the device through both the apical and basal channels. A test membrane was also placed into the device. After testing, the device successfully implemented fluid flow above and below a membrane. The device is designed such that it can accommodate membranes made to fit in 96-well plates. Currently, Retinal Pigment Epithelium (RPE) cells are being grown on membranes, and these membranes will eventually be placed into the device with media and growth factors being perfused.

Conclusion

With the microfluidic device working, the next aim is to have cells on membranes inside the device kept alive while being imaged. An onstage incubator will house the device while cells in the device are subject to apical and basal flow. Once RPE cells can confidently be kept alive in the device, stem cells will take their place and their differentiation and migration will be monitored and analyzed. Ultimately, a better understanding of the influences of stem cell fate will be gained.

References

[1] Yeo, Leslie Y., et al. "Microfluidic Devices for Bioapplications." *Small*, vol. 7, no. 1, Nov. 2010, pp. 12–48., doi:10.1002/smll.201000946.
[2] "PDMS Microfluidics | Polymer Optics." *Syntec Optics*, syntecoptics.com/polymer-optics-microfluidics/pdms-microfluidics. Accessed 13 Aug. 2017.
[3] Mcdonald, J. Cooper, and George M. Whitesides. "ChemInform Abstract: Poly(Dimethylsiloxane) as a Material for Fabricating Microfluidic Devices." doi:10.1002/chin.200238265 (2002)

Quantification of functional activity in human brain using a novel fNIRS-EEG multimodality system: the first steps

Ibukunoluwa Oni, Lia M. Hocke, Christopher Duszynski, Daniel Pittman, Bradley Goodyear, Jeff F. Dunn
[1]Biomedical Engineering Graduate Program, [2]Alberta Children's Hospital Research Institute, [3]Hotchkiss Brain Institute, [4]Department of Radiology, [5]Cumming School of Medicine, [6]University of Calgary.

Introduction

Functional activity measurements in the brain provide novel information on neurological disorders. Multi-modality imaging has the potential of providing synergistic information. Electroencephalography (EEG) provides a measure of neuronal firing whereas Functional Near-Infrared Spectroscopy (fNIRS) provides a measure of brain hemodynamics. When combined, these noninvasive modalities provide unique and complementary information which can be used to better characterize functional activity in the brain[1]. To undertake this multimodal imaging approach, we need to develop a pipeline for data acquisition and processing. The first step for implementing this approach is to: design a head-cap containing both the EEG electrodes and the fNIRS optodes, and to ensure that we can simultaneously detect brain activity with both modalities.

Methods

The electrode and optode locations were arranged according to the EEG 10-20 system to ensure regional localization. An fNIRS cap was adjusted to house the electrodes and optodes. The setup was then used to collect preliminary EEG and fNIRS time signatures during a standard visual checkerboard task[2]. We will compare fNIRS task activation and EEG gamma band activity as a marker of optical cortex activation and visual attention[3].

Results

We will:

1. Present the design and construction of our EEG-fNIRS head-cap,
2. Explain our acquisition and processing pipeline, and
3. Show preliminary simultaneous EEG-fNIRS measurements of task activation in human subjects.

Conclusion

This project introduces new multimodal technology for studying functional activity in the human brain. It is the first simultaneous EEG-fNIRS data collected in our lab and provides a starting point for our future research.

References

1. Wallois, F., et al. "Usefulness of simultaneous EEG–NIRS recording in language studies." Brain and language 121.2 (2012): 110-123.
2. Odom, J. Vernon, et al. "ISCEV standard for clinical visual evoked potentials:(2016 update)." Documenta Ophthalmologica 133.1 (2016): 1-9.
3. Si, Juanning, et al. "Correlation between electrical and hemodynamic responses during visual stimulation with graded contrasts." Journal of biomedical optics 21.9 (2016): 091315-091315.

Figures

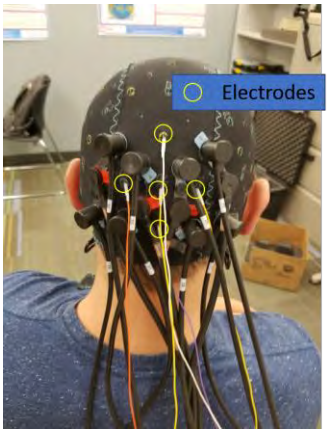

ANALYSIS OF BONE QUALITY AFTER KNEE INJURY IN AN OVINE MODEL

Tannis Kemp[1,2], Kristen Barton[3,4], Duncan Raymond[3], Andres Kroker[2,3], Jessica Norman[1,2], Nigel Shrive[1-5]

[1]Department of Mechanical Engineering, University of Calgary, Calgary, Alberta, Canada;
[2]Biomedical Engineering, University of Calgary, Calgary, Alberta, Canada;
[3]McCaig Institute for Bone & Joint Health, University of Calgary, Calgary, Alberta, Canada;
[4]Cumming School of Medicine, University of Calgary, Calgary, Alberta, Canada;
[5]Department of Civil Engineering, University of Calgary, Calgary, Alberta, Canada

Introduction

An anterior cruciate ligament (ACL) tear is a very common injury that can have severe long term consequences on the health of the knee joint such as the development of post traumatic osteoarthritis (PTOA) [1, 2]. To our knowledge, there are few studies relating the microarchitecture of the subchondral bones to ACL transection in a long-term large animal model. There are also few studies that have used micro computed tomography (Micro-CT) as a radiographic imaging method. Therefore, the main objective of the present study was to investigate the microstructure of the femur and tibia subchondral bones after anterior cruciate ligament ACL transection (ACL Tx) in an ovine model using high-quality imaging techniques.

Methods

Ten skeletally mature female Suffolk-cross sheep were studied for the partial ACL Tx model. Animals were sacrificed at either 20 or 40 weeks post-surgery. The animals were allocated into three groups: 1) 40 weeks post-partial ACL Tx (n=4), 2) 20 weeks post-partial ACL Tx (n=1), and 3) controls (n=5). All surgeries were accomplished to the right stifle joint, with the left joint serving as the control. High-resolution peripheral quantitative computed tomography (XtremeCTII, Scanco Medical, Brüttisellen, Switzerland) was used to measure bone macro-architectural and micro-architectural parameters at the distal femur and proximal tibia.

Results

The parameters of interest were trabecular area, trabecular bone mineral density, trabecular thickness, cortical area, cortical porosity and cortical thickness. We took note of the changes in parameters from each subject's right (ACL Tx) femurs and tibias to the left (contralateral control) femurs and tibias. We compared the changes in parameters of the 40 and 20 wk ACL Tx groups to the control group. The control sheep tend to have similarities between right and left bones, whereas the ACL Tx groups show large differences between the right and left bones. All parameters decrease in the event of an ACL tear for both ACL Tx groups. In the case of the trabecular and cortical areas, differences are only observed in injured femurs and not in the injured tibias. In general, larger differences are observed in cortical bone measurements compared to trabecular bone.

Conclusions

The off-loading of the injured bones caused by torn ACLs leads to an observed decrease in trabecular area, trabecular bone mineral density, trabecular thickness, cortical area, and cortical thickness. Although not conclusive, it can be said that there is an observed change in microarchitecture and an overall decrease in the quality of the bone in ACL Tx sheep following injury.

References

1. Andriacchi, T.P., et al., *A framework for the in vivo pathomechanics of osteoarthritis at the knee.* Ann Biomed Eng, 2004. **32**(3): p. 447-57.
2. Vlychou, M., et al., *Chronic anterior cruciate ligament tears and associated meniscal and traumatic cartilage lesions: evaluation with morphological sequences at 3.0 T.* Skeletal Radiol, 2011. **40**(6): p. 709-16.

Inhibition of p21 does not protect against bone loss in osteoporotic mice

Priyatha Premnath, Dante Louie, Steven Boyd, Roman Krawetz

McCaig Institute of Bone and Joint Health

Introduction: p21, a cyclin-dependent kinase inhibitor controls cell cycle progression. Inhibition of p21 has been linked to enhanced regeneration in several tissues after injury, including bone [1]. Moreover, a correlation has been reported between p21 and the osteogenic potential of human MSCs [2]. Based on these results, it was hypothesized that loss of p21 would protect against bone loss.

Methods: C57BL/6 and p21 knockout ($p21^{-/-}$) mice (4 per group) were employed to assess bony changes after ovariectomy (OVX) to induce osteoporosis. The mice were divided into three groups where bony changes were assessed from 1 to 4, 1 to 8 and 1 to 16 weeks after OVX via micro-computed tomography (μCT). Flow cytometry was performed to enumerate the number of Sca1+/CD140a+ positive mesenchymal stem cells and the number of osteoblasts and osteoclasts present in the bone marrow. Osteoclast resorption assay was carried out to assess the functionality of the osteoclasts. The mechanical characteristics of the bone was assessed via a three-point bending test.

Results: $p21^{-/-}$ and C57BL/6 mice demonstrated a reduction in bone mineral density after OVX, which was more pronounced at the 4-week time point (Figure 1). Trabecular bony parameters show a reduction in all mice, while $p21^{-/-}$ mice demonstrate an increased rate of loss compared to C57BL/6 mice (Figure 2). Mesenchymal stem cells, osteoclasts and osteoblasts are quantitatively and functionally similar in both mice strains. The 3-point bending test demonstrates that both mice have similar bone strength at the end of 16 weeks; $p21^{-/-}$ mice have stronger bones before OVX.

Conclusions: While inhibition of p21 has been reported to increase cell proliferation and consequent tissue regeneration, we found that osteoporotic $p21^{-/-}$ mice are not protected against bone loss. This finding may be due to the relationship between absent estrogen, p21 and cytokines such as IL-6, where the absence of estrogen and the additional loss of p21 causes increased IL-6, and consequently osteoclasts function longer and cause more resorption [3].

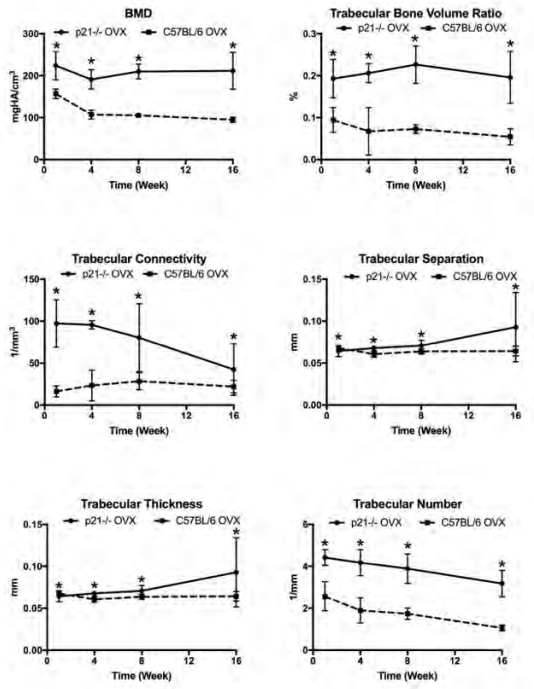

Figure 1: Bone histomorphometry of $p21^{-/-}$ and C57BL/6 mice 16 weeks post OVX. $p<0.05$

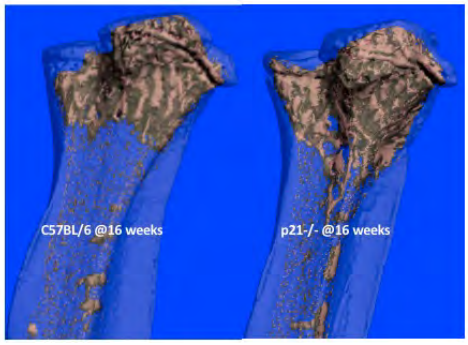

Figure 2: Representative μCT images 16 weeks post OVX in C57BL/6 and $p21^{-/-}$ mice.

References

[1] Premnath et al., BMC MSK, Submitted
[2] T. Yew et al., *Aging Cell*, 2011
[2] H. Perlman *et al.*, *J. Immunol.*, 2003.

Development of an Intraoral Force Measurement Device for Jaw Reconstruction Patients

Clayton W. Molter, Suresh Nayar, Hyun-Joong Chung, Daniel Aalto
Institute for Reconstructive Sciences in Medicine, Edmonton & University of Alberta, Edmonton

Introduction

Head and neck cancer treatment may require the patient to undergo jaw reconstruction which often results in compromised oral function and intraoral sensation. Intraoral force measurement has historically been used as a metric for evaluating the functional state of the masticatory system and the therapeutic effects of oral prostheses [1]. However, studies have found that the current occlusal force measurement standard does not provide an accurate depiction of the loading profile at the implant level [2]. A prosthesis-integrated force measurement device would provide new insight on the biomechanics of the reconstructed jaw and may inform clinicians on how to improve the jaw reconstruction and rehabilitation process. The goal of the present study was to create a prototype force measurement device on a benchtop system, serving as the first step towards characterizing the interfacial force response *in vivo*, and the development of a sensory biofeedback device for extended patient use.

Methods

The proposed design consists of a cap fixed to the implant abutment. The contact faces of the cap fit passively with individually-calibrated piezoresistive force sensors (FlexiForce A201, Tekscan) attached to the contact surfaces of the load-bearing column, which in turn is rigidly connected to the prosthesis (Figure 1). A two-implant, single-segment fibular reconstruction dentition model was 3D-printed and mounted onto a dental articulator (Figure 2). The device was wired to external data-acquisition electronics which relayed the measurement data to the computer. Experiments consisted of applying static loads to the articulator to simulate clenching and running a custom MATLAB data-acquisition program which computed the resultant three-dimensional force vector at each implant from the sensor voltage outputs at each individual face. The performance of the system was evaluated by analyzing the raw voltage measurements and behaviour of the computed force response.

Results

The device produced net force vectors with orientations similar to those found in literature. Variability between voltage measurements within a single trial was negligible, demonstrating the system's high signal-to-noise ratio. However, post-fabrication altercations to the original design, significant sensitivity to minor sensor displacement, and inherent instability of the current design led to inconsistent performance across separate trials. In contrast, behavioural tendencies persisted across all experiments, albeit at different scales. The net implant force shares a quasi-linear relationship with the applied force, but this can be attributed to propagation of the non-linear behaviour of the calibration curves.

Conclusions

This study demonstrated the feasibility of integrating this device into the prosthesis-implant interface to obtain multi-axial force measurements. The existing design is not a practical solution for *in vivo* adaptation due to issues of instability and inconsistency. The infrastructure developed in this study will serve as a foundation for the extended development, evaluation, and validation of future device iterations. Future work also aims to miniaturize and integrate this technology into a biofeedback system.

References

[1] Koc, D., *Eur J Dent* vol. 45, pp. 223-232 (2010)
[2] Kobari, H. *Int J Oral Maxillofac Implants* vol 31, pp. 1049-1057 (2016)

Figures

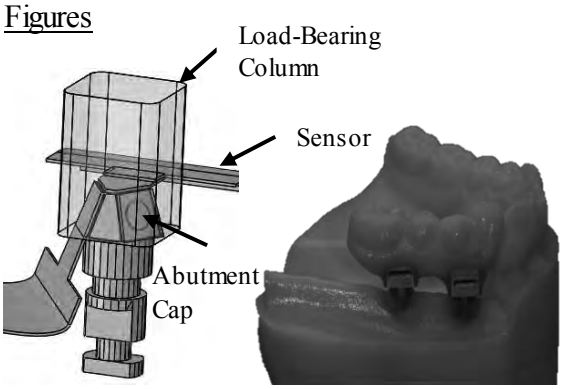

(Figure 1, left) Cap-column assembly; and (Figure 2, right) Force device mounted on 3D-printed model

Early changes in bone density and volume during fracture healing at the distal radius

Danielle E Whittier[1], Cory Kwong[2], Steven K Boyd[1], Prism S Schneider[1,2]
[1]McCaig Institute for Bone & Joint Health, [2]Department of Surgery, Division of Orthopaedic Trauma, Cumming School of Medicine, University of Calgary, Calgary, AB

Introduction

Distal radius fractures (DRF) are the most common upper extremity fracture and most often treated with immobilization in a cast [1,2]. Despite a high incidence, there is significant variability treatment duration and insufficient evidence to provide guidance on the appropriate duration for immobilization [3]. High-resolution peripheral quantitative computed tomography (HR-pQCT), offers a new and promising approach to non-invasively assess the fracture-healing process [4]. Unfortunately, current scan protocol and measured parameters for HR-pQCT are not intended for fractured bone, which contains detached cortical bone fragments and callus, often extending outside the standard scan site. A method to measure and quantify healing processes using HR-pQCT must be developed and validated. The aim of this exploratory study is to determine if 1) there are significant differences in key bone parameters between the fractured distal radius and the contralateral side shortly after fracture, and 2) if changes in bone density and bone volume during healing can be monitored using HR-pQCT.

Methods

Four female participants with stable DRFs and a mean age of 52 years have been recruited for the study. Each has completed HR-pQCT scans (XtremeCT II, Scanco Medical) of their fractured distal radius at 2 and 4 weeks from the date of fracture, and one scan of the non-fractured contralateral radius. Each scan consists of a 20.4 mm long section beginning the distal radius endplate with a 61 μm nominal isotropic resolution. Total volumetric bone mineral density (BMD) and total bone volume fraction (BV/TV) were measured from each scan. Paired samples t-tests were used to determine if significant difference ($p<0.05$) exists between the contralateral and fractured side 2 weeks after the fracture occurred, and if significant changes in BMD and BVTV can be observed in the fracture region between 2 and 4 weeks from the time of fracture.

Results

Average BV/TV of the contralateral side was 21% higher than fractured side 2 weeks after fracture, but no significant difference was observed in BMD. Average BV/TV and BMD showed a significant increase of 9.8% and 10.6%, respectively, between 2 and 4 weeks since the time of fracture. Results for BV/TV are presented in Figure 1.

Conclusions

Changes in BMD and BV/TV for the total fracture region have potential to be used as metrics for the study of fracture healing, and these results are in line with previously reported values [4]. Further work must be done to validate these findings with a larger cohort (ongoing) with more scan intervals to better assess the changes in these parameters during later stages of healing. Future assessment of fracture-healing should also take into consideration callus formation and movement of cortical bone fragments throughout fracture healing.

References

1. Koval KH, et al., J Am Acad Orthop Surg 2014 Sep;22(9):566-575. 2. Chung KC, et al., JBJS Am 2009 Aug;91(8):1868-1873. 3. Handoll HH, Madhok R., Cochrane Database 2003 4:(2)-2003. 4. de Jong, JJA, et al., Bone 2014 Jul;64:356-62.

Figures

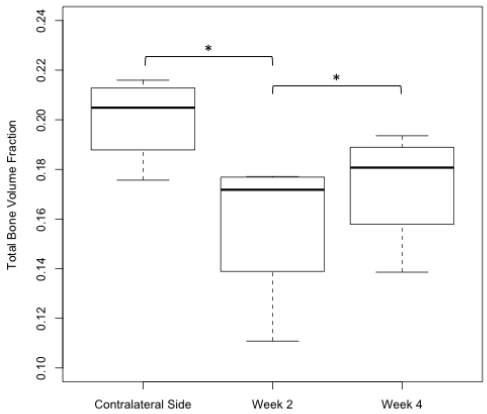

Figure 1: Differences in BVTV at distal radius between time since fracture and the contralateral radius (N=4). *p<0.05

Morphological alterations of cultured neurons in response to the mechanical properties of hydrogel

Mahdi Moezzi, Mohsen Janmaleki, Emily Kuervers, and Amir Senati-Nezhad
BioMEMS and Bioinspired Microfluidic Laboratory, Biomedical Engineering Program,
Department of Mechanical and Manufacturing Engineering, University of Calgary, Canada

Introduction

Hydrogels resemble some essential properties of extracellular matrix (ECM). Controlling the mechanical properties of photo-crosslinkable hydrogels such as gelatin methacryloyl (GelMA), mimicking ECM, provides a beneficial approach to control the behavior of neurons such as proliferation, plexus formation, and morphological characteristics.

Methods

Bovine skin gelatin was dissolved in PBS (10% wt/vol). Then, 1 mL of Methacrylic anhydride was added for each gram of Gelatin in drop wise. The obtained gelatin Methyacrylate was followed by dialysis in 12-14 kDa tubes for 4 days and freeze-dried for another 4 days. The precursor of GelMA was dissolved in PBS containing 0.5% photo-initiator (Igracure 2959) fand also was prepared to be crosslinked under UV exposure. Exposure time was selected from 5 s to 60 min to adjust the stiffness of the hydrogel. CAD cells were cultured on the GelMA that had different stiffness. ImageJ was used to analyze the length of the axons, area of the cells and the number of cells. MAP-2 and DAPI were used for staining the microtubules and nucleus respectively.

Results

The pictures were taken every 2 hours and the results are showing that the growth of CAD cells was linear in terms of the length of axons and the area of the cells for all samples. However, it was observed that the cells cultured on the stiffer GelMA grew longer axons and proliferated at a faster rate. The other interesting behavior was the number of connections that were formed among the neurons. The neurons that were cultured on the GelMA with higher stiffness had more inter-connected networks. The neurons were stained with MAP-2 to observe the possible distribution of microtubules in axons and dendrites. Due to the hydrogel nature, the captured fluorescence images did not provide a clear image of organizations of microtubules within the cells. Therefore, the hydrogel must be prepared on a dark substrate for fluorescence imaging purposes. In the next step, we will be culturing the neurons within the hydrogel to understand how 3D micro-environment affect the cellular behavior.

Conclusion

By manipulating the mechanical properties of the substrate, the effects of neural cells behavior can be observed, such as morphology and proliferation. Therefore, in order to treat or to make a model of the neurodegenerative disease, a suitable hydrogel with appropriate properties must be used.

References

[1]G. Ebersole, P. Anderson and H. Powell, "Epidermal differentiation governs engineered skin biomechanics", Journal of Biomechanics, 2010.
[2] Tong X and Yang F 2014 Engineering interpenetrating network hydrogels as biomimetic cell niche with independently tunable biochemical and mechanical properties Biomaterials 35 1807–15

Figures:

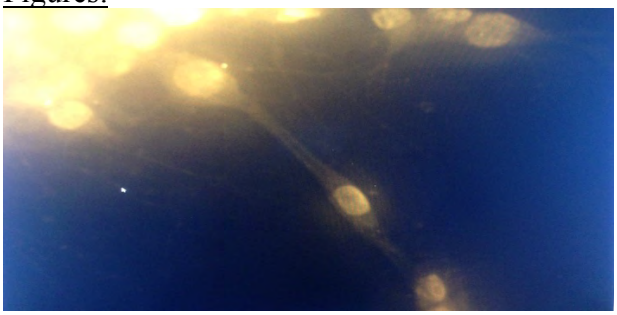

Fig1: fluorescence imaging of stained CAD cells (MAP-2) showing Axon and cell body

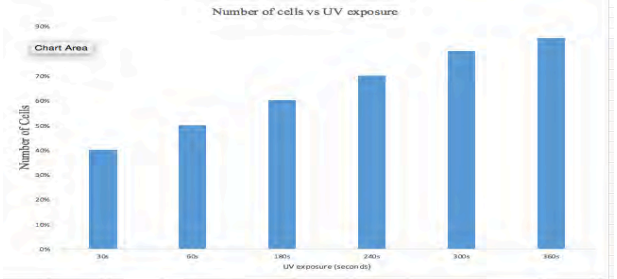

Automatic Segmentation of Subchondral Bone in Weight-bearing Regions of the Tibia

Michael T Kuczynski, Andres Kroker, Steven K Boyd, Sarah L Manske
McCaig Institute for Bone & Joint Health, Cumming School of Medicine, University of Calgary, Calgary, AB

Introduction

To better understand how osteoarthritis (OA) and other bone diseases affect subchondral bone, developing an automated segmentation technique for identifying subchondral bone in the knee is desired. High-resolution peripheral quantitative computed tomography (HR-pQCT) is currently used to provide three-dimensional images of bone with sufficient spatial resolution to resolve individual trabeculae. While global thresholding approaches are sufficient to segment bone from soft tissue in standard distal radius and distal tibia HR-pQCT scan sites, automated segmentation of the subchondral bone in tibial condyles poses a new challenge, as the density of subchondral bone varies with depth. The objective was to develop a more accurate segmentation techniques for *in vivo* scans that account for local density differences in the suchondral bone of the tibial condyle.

Methods

Eight intact cadaveric tibia scans were acquired on the HR-pQCT (XtremeCTII, Scanco Medical) using *in vivo* settings (61µm isotropic voxel size) and a gold standard (30µm isotropic voxel size). To determine the optimal segmentation techniques 22 different segmentation methods were applied to 30µm cadaveric tibia scans and implemented using the Image Processing Language (IPL, Scanco Medical). The new methods were compared to the current standard global segmentation technique based on three metrics: 1) bone volume fraction (BV/TV), 2) trabecular thickness (Tb.Th), and 3) visual inspection. To avoid individual bias when visually ranking segmentation methods, 15 people were asked to score various segmented regions based on how well they visually represent a grayscale image. Regression and Bland-Altman plots were generated to compare 61µm current standard and cube segmentation methods against 30µm segmentations (gold standard).

Results

The best performing local cube segmentation technique splits the ROI into smaller sub regions, or cubes. These cubes are then processed individually and concatenated back together after applying local Gaussian and median smoothing filters, a local 3D Sobel edge detection operator, a local subtraction operation, and finally applied Otsu's method to each cube to separate bone from soft tissue. This segmentation technique was chosen based on the smallest difference in BV/TV and Tb.Th between the 30µm gold standard method and the 61µm local cube method. When comparing visual scoring results, 11 out of 15 people chose the local cube segmentation method as the best representation of the original scan.

Conclusions

An improved automatic segmentation technique for subchondral trabecular bone for *in vivo* HR-pQCT proximal tibia scans been developed, with a run time of only 15 to 20 minutes per scan. Splitting the ROI into smaller sub regions (150x150x150 voxels) facilitated the segmentation techniques to distinguish between bone and soft tissue. The use of Otsu's method for threshold selection allowed for a robust segmentation method as it is ideally suited to scans with varying bone mineralization. Obtaining accurate segmentation of subchondral trabecular bone will help improve our understanding of the microarchitecture underlying early knee OA and other bone-related diseases.

Figures

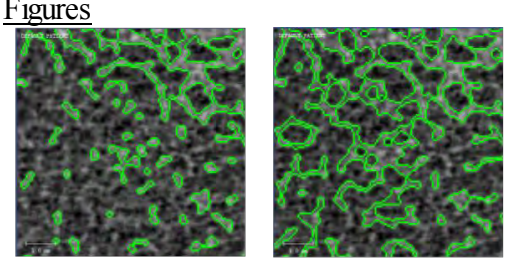

Figure 1: Comparison of Current Standard Segmentation Technique and the Improved Local Cube Segmentation Technique

Towards an Improved Gluten Detection Device

Nikhil Vastarey,[a] Jonathan Wong,[a] Winnie Chou,[a] Varun Vij,[a] Prof. Ray J. Turner,[b] Prof. Orly Yadid-Pecht[a]

[a] Integrated Intelligent Sensing (I2Sense) Laboratory, Department of Electrical and Computer Engineering, Schulich School of Engineering, University of Calgary, Alberta, Canada
[b] Department of Biological Sciences, University of Calgary, Canada

Introduction- Gluten sensitivity, gluten intolerance and celiac disease are conditions that cause a person to react after ingesting gluten, a protein commonly found in wheat, barley and rye. These can lead to gastrointestinal problems, diarrhea, joint pain, ulcerative colitis, eczema, skin rashes, tiredness, depression, etc. Since the switching to complete gluten free diet is the only promising solution to this problem so far, the amount of gluten in unknown food products needs to be strictly monitored and controlled to be below the standardized limit of 20 ppm. For this level of detection, a dye labelled aptamer based 'turn-On' fluorogenic sensor is being developed in our lab to detect gluten in food. This particular aptamer has selective affinity towards 33-mer immunogenic peptide found in the alpha-gliadin sub-unit of gliadin protein which is responsible for wheat allergies and Celiac disease.[1] Standard emission based curves for the fluorophore in the presence of peptide is developed against known subsequent concentrations of gliadin standard. This standard curve is used to detect the amount of gliadin present in the unknown food sample after measuring the emitted fluorescence from an unknown food sample. We will describe the mechanism of our hybrid sensing material towards gliadin detection, followed by the imminent challenges towards the development of a functioning gluten sensing device. These results are compared against ELISA (Enzyme Linked ImmunoSorbent Assay) results from food diagnostic labs, and other contemporary devices to gauge the accuracy of our system.

Conclusion- A portable gluten detection device is currently under design. This device is to be capable of sample extraction from the food, interaction with the bio-probe and undergo fluorogenic detection *via* sol-gel based micro optical filters (Figure 1) over the CMOS imager.[2]

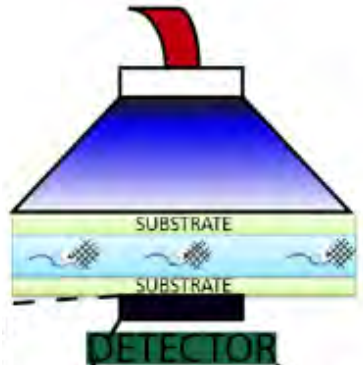

Figure 1. This figure illustrates a transmittable substrate for imaging fluorescent emission on binding of the sample with the sensing material.

[1] Schalk, K.; Lang, C.; Wieser, H.; Koehler, P.; Scherf, K. A. *Sci. Rep*. 2017, 7, 45092.
[2] Cao, M.; Mahto, S. K.; Yadid-Pecht, O. *IEEE Sensors*, 2016, 16, 3611.

Quantitative MRI of cadaver knee articular cartilage in axial compression using a custom MRI-safe loading rig

Chelsey S Thorson, Madeline M Martel, Emily J McWalter
Mechanical Engineering Department, University of Saskatchewan, Saskatoon, SK, Canada

Introduction

Articular cartilage plays the important role of transmitting load through the joint. T_2 relaxation time mapping is a quantitative magnetic resonance imaging approach that is associated with articular cartilage collagen architecture[1], water content[2] and mechanical properties[3]; assessing changes in T_2 with load may provide information about articular cartilage function *in situ*. Therefore, the objectives of this study are to design, build, and test an MRI-safe loading rig capable of applying compressive force to a cadaveric knee joint, as well as to develop a post-processing protocol to compare focal changes in T_2 maps of articular cartilage between unloaded and loaded conditions.

Methods

Mechanical Testing

A custom device was needed in order to apply a compressive load to the cadaver joint. The chosen design (Fig. 1) is made of MRI-safe material and utilizes four threaded rods {A} that can be tightened into the containment tube {B} compressing the specimen {C} against a non-ferrous load cell {D} (Futek, Irvine, USA). The rig can apply up to ~890N of compressive load to a biological specimen.

Image Acquisition

A cadaveric human knee joint will be scanned in a 3.0 T MRI scanner (Magnetom Skyra, Siemens, Erlangen, Germany modified double echo steady state (DESS) sequence[4]. Quantitative T2 maps will be created using an approximation method[5]. The specimen will be scanned unloaded and then with an ~890 N load. Since cartilage is viscoelastic, the specimen will be allowed to reach equilibrium prior to acquiring the loaded scan by subtracting time series MRI scans until only noise is visible (~45 min).

Image Analysis

A cluster-based analysis, developed previously, by our group will be adapted for our purpose[6]. Briefly, T_2 projection maps of the unloaded and loaded data will be created and then subtracted, resulting in a difference map. A cluster analysis is carried out on the difference map to identify focal areas of change between conditions (Fig. 2).

Results

The compression rig was built and tested with a bovine sample in the MRI scanner. Sample data was used to test the image processing pipeline. This work is ongoing.

Anticipated Conclusions

We successfully designed and constructed an MRI-safe loading device and established an articular cartilage post-processing pipeline, which will be used in human cadaver knee specimens. The resulting cluster maps will give initial indications of any areas that might be disproportionally affected by applied load.

References

[1] Nieminen et al. *MRM.* 2001 [2] Lusse et al. *MRI.* 2000 [3] Lammentausta et al 2006 JOR [4] Staroswiecki et al. *MRM.* 2012 [5] Sveinsson et al. *JMRI.* 2016 [6] Monu et al. *OA&C.* 2016

Figures

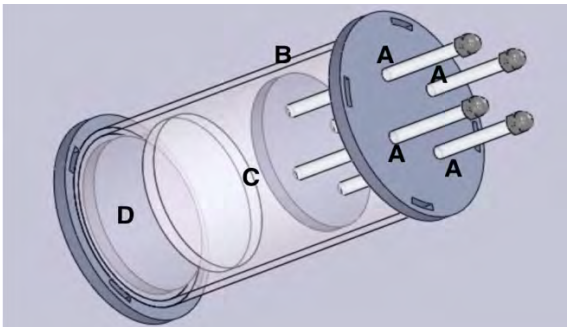

Figure 1: Model of MRI-safe, custom loading rig

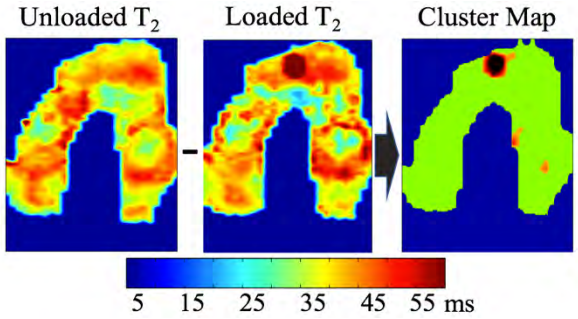

Figure 2: Image analysis pipeline. Unloaded and loaded projection maps are subtracted. The cluster map identifies regions of change with load.

Paracrine effects of mesenchymal stem cells on *in vitro* cardiac fibrosis model

Kar Wey Yong[1,2], Amir Sanati Nezhad[2], Arindom Sen[1]

[1] Department of Chemical and Petroleum Engineering, University of Calgary, Calgary, AB, T2N 1N4, Canada.
[2] BioMEMS and Bioinspired Microfluidic Laboratory, Center of Bioengineering Research and Education, Department of Mechanical and Manufacturing Engineering, University of Calgary, Calgary, AB, T2N 1N4, Canada.

Introduction

Cardiac fibrosis is a heart remodelling process which cannot be completely stopped or reversed by the currently available drugs and surgeries once it has begun, adversely leading to cardiac failure and death [1]. With the advances in regenerative medicine, mesenchymal stem cell (MSC) therapy could be a promising treatment for cardiac fibrosis, as MSCs have been demonstrated their great potential in multi-lineage differentiation and secretion of soluble factors, which help to regulate tissue repair and regeneration [2, 3]. To explore the therapeutic effects of MSC on cardiac fibrosis, it is required to develop an *in vitro* cardiac fibrosis model mimicking a native fibrotic cardiac tissue.

Methods

Collagen coated polyacrylamide hydrogel at a stiffness of 30 kPa, which mimics the stiffness of a native fibrotic cardiac tissue [4, 5], was fabricated. Cardiac fibroblasts were cultured on the hydrogel for 5 days following by the assessment of cardiac myofibroblast differentiation (a hallmark of cardiac fibrosis) markers, including alpha smooth muscle actin, collagen type 1, collagen type 3, and transforming growth factor beta-1, through the immunofluorescence staining or Real-Time PCR method. Then, the conditioned medium of MSCs derived from adipose tissues was added to determine its effects on the cardiac myofibroblast differentiation.

Results

Cardiac fibroblasts were found to differentiate into cardiac myofibroblasts, which significantly highly (p<0.05) expressed all the cardiac myofibroblast differentiation markers, suggesting that 5-day cultured cardiac fibroblasts on a hydrogel with the stiffness of 30 kPa can be used as an *in vitro* cardiac fibrosis model. Conditioned medium of MSCs applied to the model was found to significantly suppress (p<0.05) expression of all the cardiac myofibroblast differentiation markers, indicating the inhibitory effects of MSCs on cardiac myofibroblast differentiation through the paracrine mechanisms.

Conclusions

MSCs may inhibit cardiac myofibroblast differentiation via the paracrine secretion of anti-fibrotic factors, which in turn alleviate cardiac fibrosis. These findings will aid in establishment of the therapeutic application of MSCs for cardiac fibrosis in future.

References

1. Daskalopoulos, E.P., B.J. Janssen, and W.M. Blankesteijn, *Myofibroblasts in the infarct area: concepts and challenges.* Microscopy and Microanalysis, 2012. **18**(1): p. 35-49.
2. Ramkisoensing, A.A., et al., *Interaction between myofibroblasts and stem cells in the fibrotic heart: balancing between deterioration and regeneration.* Cardiovascular research, 2014. **102**(2): p. 224-231.
3. Yong, K.W., et al., *Cryopreservation of human mesenchymal stem cells for clinical applications: current methods and challenges.* Biopreservation and biobanking, 2015. **13**(4): p. 231-239.
4. Berry, M.F., et al., *Mesenchymal stem cell injection after myocardial infarction improves myocardial compliance.* American Journal of Physiology-Heart and Circulatory Physiology, 2006. **290**(6): p. H2196-H2203.
5. Engler, A.J., et al., *Embryonic cardiomyocytes beat best on a matrix with heart-like elasticity: scar-like rigidity inhibits beating.* Journal of cell science, 2008. **121**(22): p. 3794-3802.

Validating In Vivo Measures Quantitative Magnetization Transfer MRI of Cartilage using Mechanical, Biochemical, and Histological Analysis

Kirstin D Olsen[1], Ives Levesque[2], Emily J McWalter[1]
[1]University of Saskatchewan and [2]McGill University Health Centre

Introduction

Osteoarthritis (OA) is a chronic disease that involves the loss of proteoglycan and collagen in articular cartilage and meniscus[1-4]. Quantitative magnetization transfer (qMT) magnetic resonance imaging (MRI) is a promising, non-invasive approach to study cartilage degeneration because it probes the relationship between free and bound water in the tissue; we hypothesize bound and free water interactions will change with degeneration. The aim of this study is to validate qMT as an imaging biomarker of cartilage and meniscus structure and function in OA patients.

Methods

Tissue Sample Acquisition, Preparation and Registration: We will scan 20 pre-total knee arthroplasty (TKA) patients at 3T using an established *in vivo* qMT protocol[5] and a 3D 0.6 mm isotropic, morphological sequence. We will retrieve articular cartilage and meniscus tissue post-TKA surgery. Intact tissues will be used for mechanical testing and core samples will be obtained for biochemical and histological analysis. An Iterative Closest Points (ICP) algorithm[6] will be used to register MRI, mechanical testing, biochemical, and histological data.

Mechanical Testing: Indentation testing will be carried out using a materials testing system (Mach-1, Biomomentum, Laval, PQ). In particular, shear modulus and Young's modulus will be determined at discrete points over the entire articular cartilage and meniscus surface at a resolution of 0.5 mm. The topology of the 3D surface will also be mapped at the same resolution for registration.

Biochemical Assessment: Proteoglycan and collagen content will be determined through standard sulfated glycosaminoglycan (sGAG) and hydroxyproline assays, respectively. Specimens will be weighed, lyophilized, and re-weighed to determine wet to dry mass ratio. The samples will then be digested in proteinase-K. sGAG content will be determined using a dimethylmethylene blue assay and hydroxyproline content using a pDAB/chloramine T assay.

Histology: Histological scoring of cartilage and meniscus samples will be performed using standard scoring systems[7, 8]. Samples will be stained with hematoxylin and eosin (H&E)[8], safranin-O[7], toluidine blue[9], picosirius red[10], and goldner's trichrome[9] in order to assess tissue morphology, proteoglycans, and collagen.

Statistical Analysis: Multiple regression will be used to determine if qMT parameters can predict mechanical tissue properties using a packaged software (Stata, Statacorp, College Station, TX). Correlation between qMT parameters and biochemistry and histology results will also be assessed using a Pearson product-moment correlation coefficient and Spearman rank-order correlation coefficient, respectively.

Results

This project is ongoing and as such no results are presently available. We are currently establishing detailed protocols for all testing procedures.

Anticipated Conclusions

We expect to validate qMT as a non-invasive, *in vivo* imaging biomarker of both tissue health and function in OA patients. This will provide an objective measure that can assess tissue function.

References

1) Bursac et al, Biorheology, 2009; 2) Herwig et al, Ann Rheum Dis, 1984; 3) DiMicco et al, Arthritis Rheum, 2004; 4) Morel et al, Biorheology, 2004; 5) Simard et al, ISMRM, 2016; 6) Besl et al, IEEE Trans. Pattern Anal. Mach. Intell., 1992; 7) Pritzker et al, Osteoarthritis Cartilage, 2006; 8) Pauli et al, Osteoarthritis Cartilage, 2011; 9) Schmitz et al, Osteoarthritis Cartilage, 2010; 10) Junquiera et al, Anal Biochem, 1979

Investigating the role of cell cycle activation in stem cells on cartilage regeneration *in vivo*

A.O. Masson, T.M. Underhill, R. Krawetz
University of Calgary, Calgary, AB, Canada

Introduction

Cartilage shows little intrinsic repair after injury, which can lead to the development of degenerative diseases as osteoarthritis (OA). Affecting over 4.6 million Canadians aged 15 and older [1], OA current treatments provide temporary or incomplete improvements in health, function and/or quality of life. Thus, the development of methods for regenerating injured cartilage tissue and/or treating OA with sustained effects is clinically relevant. One promising area of study in the field is tissue regeneration by $p21^{CIP1/WAF1}$ inhibition [2], [3], since the only known single mutation capable of inducing a cartilage regenerative phenotype is that of p21 knockout ($p21^{-/-}$ mouse). However, the mechanisms between this cause and effect remain poorly understood, especially given the involvement of p21 in multiple intricate cellular processes [3]. Since p21 is an important cell cycle regulator, whose inhibition allows cell cycle progression, in this study, we aim to investigate if *in vivo* cell cycle activation of quiescent mesenchymal stem cells (MSCs) can regulate cartilage repair after injury.

Methods

MSCs reporter mice $EMC^{CreERT2\text{-}TdT}$ on a non-healing C57Bl6 background (controls) were bred to a conditional E2F1 (downstream of p21) overexpression mouse ($ROSA^{CAG\text{-}E2F1\text{-}EGFP}$). E2F1 overexpression was induced with tamoxifen. 6-8 weeks old control and E2F1 activated mice underwent standardized focal cartilage injuries in the ear (vascular) and knee (avascular). Through and through ear wounds (Ø = 2 mm) were generated with a standard ear punch, and full thickness cartilage defects (FTCD) were induced in the femur trochlear groove (Ø ≅ 0.4 mm) with a hypodermic needle. Healing was assessed at 1, 2 and 4 weeks after injury by measuring ear role diameter and histologically grading knee cartilage defect in a 14-point scale [4]. MSCs (TdT+) and E2F1 activation (GFP+) were identified using immunofluorescence.

Results

In these preliminary results, control nor E2F1 activated mice ear holes demonstrated repair over 4 weeks (Fig.1). At 2 weeks, the mean histological score after FTCD was 3.5 ± 0.3 in controls vs. 9.7 ± 0.5 in E2F1 mice (Fig.2A-C). MSCs (TdT^+) with E2F1 activation (GFP^+) were observed in the injury site in all time points (Fig.2D-I)

Conclusions

Activated MSCs migrate to injury site, but do not directly contribute to newly formed cartilage tissue. Further studies are required to elucidate the potential role of cell cycle activation in MSCs on cartilage repair.

References

[1] C. Bombardier, G. Hawker, and D. Mosher, "The Impact of Arthritis in Canada : Today and Over the Next 30 Years," 2011.
[2] K. Bedelbaeva *et al.*, *Proc. Natl. Acad. Sci. U. S. A.*, vol. 107, no. 13, pp. 5845–50, 2010.
[3] L. Arthur and E. Heber-Katz," *Stem Cell Res. Ther.*, vol. 2, no. 3, p. 30, 2011.
[4] J. Fitzgerald *et al.*, *Osteoarthr. Cartil.*, vol. 16, no. 11, pp. 1319–26, 2008.

Figures

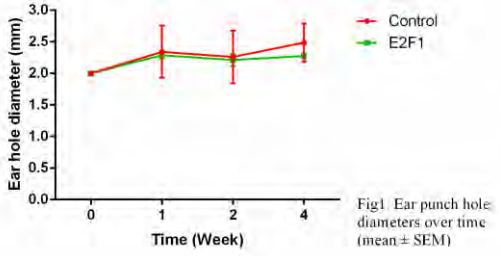

Fig1. Ear punch hole diameters over time (mean ± SEM)

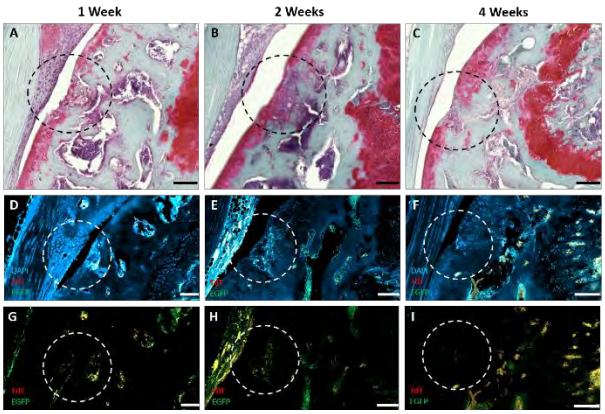

Fig2. Sagittal sections of E2F1 mouse femurs 1, 2 and 4 weeks after FTCD. A-C: stained by Safranin-O/Fast Green, D-F: DAPI-TdT-EGFP and G-I: TdT-EGFP immunofluorescence. Scale bars = 100µm.

Prx1^{+} Progenitor Cells Contribute to Spontaneous Articular Cartilage Repair in p21$^{-/-}$ Mice

Jablonski CJ[1], Ali J[2], Tailor P[2], Leonard C[2], Krawetz RJ[2]
[1]Faculty of Biomedical Engineering, University of Calgary, AB, Canada, [2]Faculty of Medicine, University of Calgary, AB, Canada

Introduction

Cartilage injuries in mammals do not demonstrate robust capacity for repair. Previous studies in p21$^{-/-}$ mice have shown that p21$^{-/-}$ mice can spontaneous repair cartilage injuries [1], however the contributing cell type(s) remain unknown. While mesenchymal stem cells (MSCs) are unique in their ability to self-renew or differentiate into the chondrocytes that make up articular cartilage [2], studies in the literature have shown that MSCs only rarely directly contribute to the formation of new tissues after injury [3]. To address this knowledge gap, lineage tracing using the MSC marker Paired Related Homeobox-1 (*Prx1*) was performed as *Prx1*$^{+}$ cells are known to give rise to bone, fat and cartilage *in vivo* and *in vitro* [4].

Methods

Full-thickness cartilage defects were induced in the trochlear groove of left femurs in *Prx1*$^{CreERT2\text{-}GFP}$R26R^{TdTomato};C57BL/6 (C57) and *Prx1*$^{CreERT2\text{-}GFP}$R26R^{TdTomato};p21$^{-/-}$ (p21$^{-/-}$) mice. Cartilage regeneration was assessed using a 14-point scoring scale. Immunofluorescence was used to identify endogenous Prx1^{+} progenitors (GFP^{+}TdTomato^{-}) and their differentiated progeny (GFP^{-}TdTomato^{+}). Data was collected 1day/1, 2, 4week(s), post-injury in C57 (Figure 1) and p21$^{-/-}$ mice.

Results

Compared to C57 controls, p21$^{-/-}$ mice demonstrated increased cartilage regeneration at 4 weeks post-injury (4.8±0.61 vs. 8.10±0.73, respectively). Furthermore, *Prx1*$^{+}$ progenitors were only observed within the cartilage site within in p21$^{-/-}$, while in C57 mice, *Prx1*$^{+}$ cells were observed adjacent to the injury. However, *Prx1*$^{+}$ progenitors in p21$^{-/-}$ mice remained un-differentiated and did not directly contribute to the formation of new cartilage.

Conclusions

Prx1^{+} progenitors are differentially recruited to injury sites in C57BL/6 vs. p21$^{-/-}$ mice, and while these progenitor cells are in proximity to the regenerating cartilage in p21$^{-/-}$ mice, they remain undifferentiated and do not directly contribute to the formation of new cartilage (e.g. differentiate into chondrocytes). This suggests that *Prx1*$^{+}$ progenitors produce trophic factor(s) that induce spontaneous cartilage regeneration. The identification of these factors may have significant clinical potential in treating patients with cartilage injuries and/or degenerative diseases such as osteoarthritis.

References

[1] Bedelbaeva et al. Proc. Natl. Acad. Sci. U. S. A., vol. 107, no. 13, pp. 5845–50, 2010.
[2] Pittenger et al. Science, vol. 284, no. 5411, pp. 143–7, 1999.
[3] Kurth et al. Arthritis Rheum., vol. 63, no. 5, pp. 1289–300, 2011.
[4] Nohno et al. Dev. Biol., vol. 158, no. 1, pp. 254–64, 1993.

Figure

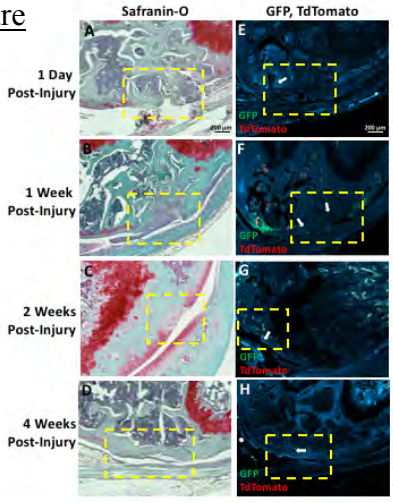

Figure 1. Safranin-O staining (A-D) and immunofluorescence images (E-H) to identify endogenous Prx1^{+} progenitors (GFP^{+}TdTomato^{-}) and their differentiated progeny (GFP^{-} TdTomato^{+}) in C57 mice at 1 day, and 1, 2, and 4 weeks post-injury.

Automated lymph node segmentation in histopathological images

Salah Alheejaw[1], Hongming Xu[1], Richard Berendt[2], Naresh Jha[2], and Mrinal Mandal[1],
Department of Electrical and Computer Engineering[1], Department of Medicine[2], University of Alberta

Introduction

Melanoma is a dangerous type of skin cancer, spread around the world [1]. Melanoma shows aggressive and unpredictable behavior which can spread to any part of the body through lymphatic system. The lymph nodes collect the cancer cells that escape from the original tumor and try to spread to the rest of the body, Lymph node analysis is important for grading many types of diseases such as melanoma and breast cancer. In image based Computer Aided Diagnosis (CAD), lymph node segmentation is the first step for lymph node analysis. nodes.

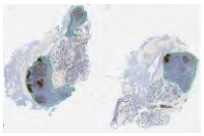

Fig. 1. Sentinel Lymph Nodes (SLN) contoured by green line and stained with MART-1.

Methods

In this paper, we propose an automated technique to segment the lymph nodes in a histopathological image obtained with MART-1, Ki-67 and H&E staining. The proposed technique consists of three steps. First, we perform a coarse segmentation of the image based on histogram analysis and

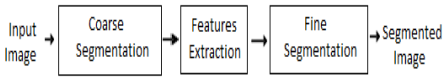

Fig. 2. Schematic of the proposed technique.

identify three regions: lymph node (*Class-1*) tissue, melanoma (*Class-2*) and other tissue region (*Class-3*). First, we calculate the texture feature of every pixel based on the frequency of the classified pixels in the neighborhood area. another feature vector has been defined by the number of pixels that belong for each *Class* in that neighborhood. Finally, Support Vector Machine (SVM) is applied on the extracted features to perform the fine segmentation of the lymph

Results

The proposed technique has been evaluated on database of 27 histopathological image with 76 lymph nodes. The ground truth for these images, has been generated by segmenting the lymph nodes manually by doctors. After SVM classification, the sensitivity, precision, specificity and accuracy are calculated.

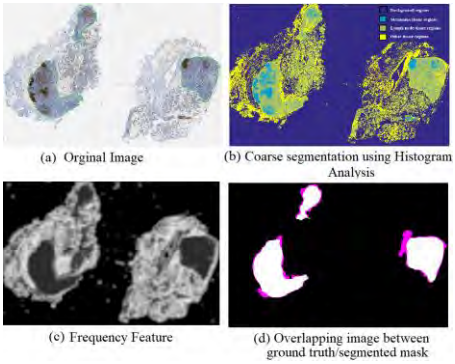

Fig. 3. Shows the resulted images.

Table 1 Lymph node Segmentation performance

sensitivity	specificity	precision	accuracy
93%	95%	90%	96%

Conclusion

The technique has been tested with different stains and it shows a good performance in the lymph node segmentation. In future, we will use the technique to measure the proliferation index of the melanoma region inside the segmented lymph node on ki-67 stain.

References

[1] I Maglogiannis, Overview of advanced computer vision systems for skin lesions characterization. IEEE Trans. Inf. Technol. Biomed, (2009).

[2] A. C. Bovik, "Multichannel Texture Analysis Using Localized Spatial Filters", *IEEE Trans. PAMI*, 1990.

Modeling of the Mechanical Behavior of 3D-Bioplotted Scaffolds

Saman Naghieh[1], Mohammad Reza Karamooz-Ravari[2], MD Sarker[1], Adam D McInnes[1], Xiongbiao Chen [1,3]

[1] Division of Biomedical Engineering, College of Engineering, University of Saskatchewan, Saskatoon, SK, Canada

[2] Department of Mechanical Engineering, Graduate University of Advanced Technology, 76318-18356 Kerman, Iran

[3] Department of Mechanical Engineering, College of Engineering, University of Saskatchewan, Saskatoon, SK, Canada

Introduction

Developing of tissues scaffolds to repair the damaged tissues/organs is one of the fundamental goals of tissue engineering [1]. To this end, the design and fabrication of tissue scaffolds have been shown as challenging tasks [2]. One important issue in the design of scaffolds is to achieve the mechanical properties that match those of tissues/organs to be repaired. To address this issue, modeling and numerical simulations of scaffold mechanical properties are of powerful tools but limited by the imperfect representation of the features of fabricated scaffolds. Specifically, due to the fluid nature of scaffold solution for 3D bioplotting, scaffolds are always fabricated with the penetration of strands in one layer into the previous layer. This feature, however, has been ignored in the literature. The significance of the present study rests on the development of a novel model representative of the mechanical behavior of bioplotted scaffolds, by taking into account the aforementioned strand penetration. Once validated by experiments, the model was used to discover the influence of strand penetration, along with other scaffold geometrical features, on the scaffold mechanical behavior, which is also missing in the literature.

Methods

The finite element method was utilized to develop a model for predicting the elastic modulus of 3D bioprinted alginate scaffolds. Compression tests were performed to calculate the elastic modulus of the scaffolds.

Results

Experimental results were compared with the numerical model and it was concluded that the model can predict the mechanical behavior of alginate with 8% difference. Then, the effect of strand penetration and other geometrical features on the elastic modulus of bioplotted scaffolds was studied using this model.

Conclusions

In this study, a novel finite element model is presented to predict the elastic modulus of bioprinted scaffolds. The focus of this model was on the penetration within layers and accordingly, the effects of the number of layers and strand diameter were studied. Results demonstrated 8% difference between model and the experimental findings. Hence, to evaluate the mechanical properties of scaffolds before fabrication, this model can be used to have scaffolds with desired mechanical properties.

References

1. Zehnder, T., et al., Evaluation of an alginate-gelatine crosslinked hydrogel for bioplotting. *Biofabrication* **7,** (2015).
2. Chen, X. B. Dispensed-Based Bio Manufacturing Scaffolds for Tissue Engineering Applications. *Int. J. Eng. Appl.* **2,** 10–19 (2014).

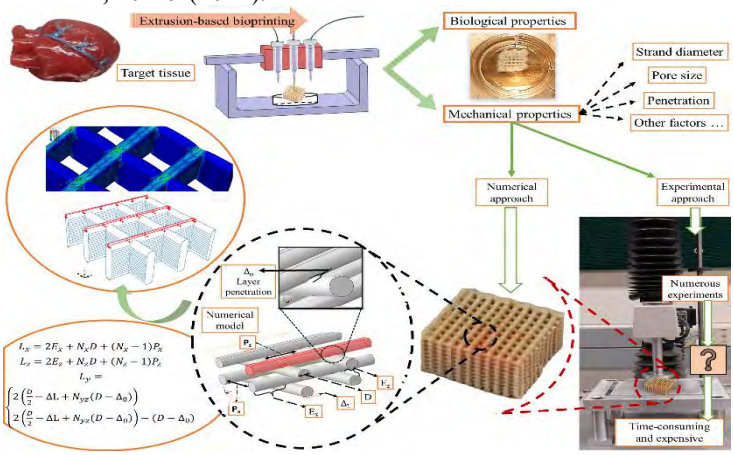

Pathological Mitochondrial Fission and its Role in IBD

Luke, Goudie[1], Nicole L. Mancini,[2] Arthur Wang,[2] Derek M. McKay,[2] & Jane Shearer[1,3].
[1]Department of Biomedical Engineering, Schulich School of Engineering; [2]Department of Physiology and Pharmacology, Cumming School of Medicine; [3]Faculty of Kinesiology
University of Calgary, 2500 University Drive NW. Calgary, AB. T2N 1N4

Introduction: Inflammatory bowel disease (IBD) encompasses a group of disorders that involve an exaggerated immune response to intestinal microbes. The permeability and barrier function of epithelial cells to intestinal microbes, is closely tied to proper mitochondrial respiration, shown by studies examining intestinal permeability after mitochondrial dysfunction induced by dinitrophenol[1]. In the presence of stressors like microbes or dinitrophenol, mitochondria may undergo excessive fission and exhibit reduced respiratory capacity, leading to defects in intestinal mitigation of intestinal microbes. This excessive fission, mediated by DRP1 and Fis1, promotes a remodeling of mitochondrial networks into more punctate mitochondria that also generates more reactive oxygen species and affects cell death pathways[2,3]. Recently we, and others, have assessed the possibility that excessive mitochondrial fission affects epithelial-microbial interactions, decreases epithelial barrier function and contributes to enteric inflammation.

Methods: Hypothesising that elevated mitochondrial fission would occur in enteric inflammation, male Balb/c mice were given dextran sulfate sodium (DSS) (5% (w./v.) 5 days, 3 days water) or dinitrobenzene sulfonic acid (DNBS) (3 mg, intrarectally.) ± an inhibitor of DRP1 and Fis1, P110 (3 mg/kg, intraperitoneally.) daily.

Results: On necropsy DSS and DNBS displayed the characteristic signs of colitis associated with these models. Disease was substantially less in P110-treated mice as gauged by (i) weight loss (ii) macroscopic disease scores, (iii) shortening of the colon and (iv) colon motility (n=8-12). Analysis of histopathology on H&E stained sections of mid-colon revealed some improvement in P110 treated mice, but this was not a statistically significant result.

Conclusions: Systemic administration of a selective inhibitor of mitochondrial fission reduced the severity of disease in two different, commonly used murine models of colitis. Studies are required to define the mechanism of this effect in terms of the target cell (e.g. epithelium vs. macrophage) and systemic vs. local effects of the P110. We conclude that inhibition of DRP1 and Fis1 interaction provides a novel approach to mitigating IBD.

References:
1.Lewis, K., and McKay, D.M. Ann. N.Y. Acad. Sci. 1165, 327–337 (2009).
2. Qi, X., Qvit, N., Su, Y. C. & Mochly-Rosen, D. Journal of Cell Science. 126,789–802 (2013).
3. Guo, X. et al. Journal of Clinical Investigation. 123, 5371–5388 (2013).
4. Kornfield, O. S. et al. Circulatory Research. 116, 1783–1799 (2015).

Figures:

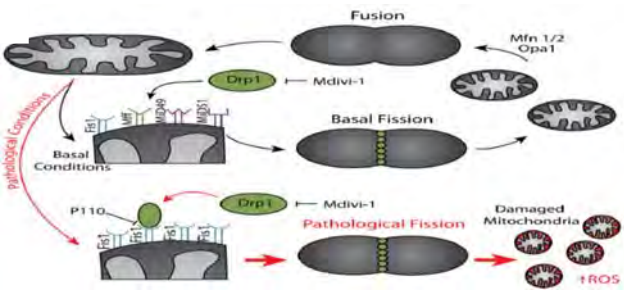

1A) Representation of P110 and its role in mitochondrial fission[4]

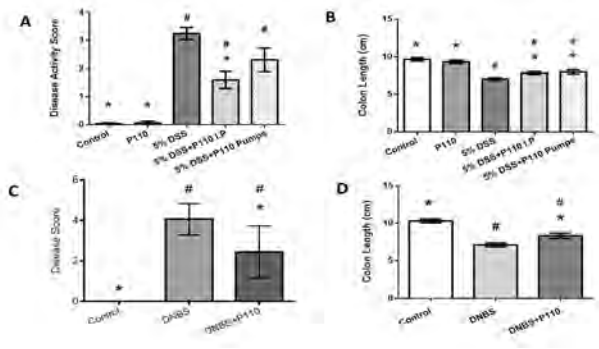

2A-2B) Colon length and macroscopic disease score results for DSS±P110
2C-2D) Colon length and macroscopic disease score results for DNBS±P110

Effects of Adding Adipose Derived Mesenchymal Stem Cell Secretome on the MIN6 Pancreatic Beta Cell Line in Culture

Jane Maynard[1], Jolene Phelps[1], Mark Ungrin[2], Arindom Sen[1]
[1]Pharmaceutical Production Research Facility, University of Calgary, [2]Department of Veterinary Medicine, University of Calgary

Introduction

Mesenchymal stem cells (MSCs) are found in many adult human tissues, and are self-renewing and capable of differentiating into cartilage, bone, and fat-like cells. When isolated from different tissues MSCs display a similar phenotype but possess distinctive functions related to their origin. MSCs are thought to have two repair mechanisms; by differentiation into target cells and by utilization of secreted factors [1], known collectively as the secretome. The secretome contains growth factors, cytokines, and extracellular vesicles (EVs). EVs are phospholipid bilayer enclosed membranes that contain proteins and RNAs. MSCs use paracrine signaling through the secretome as a pathway for immunomodulation and cell-to-cell communication [1].

The purpose of this study was to evaluate the possibility of increasing proliferation and survival of the mouse derived MIN6 pancreatic beta cell line using the secretome from ethically obtained human adipose derived MSCs. This was analyzed by looking at MIN6 cell survival in the presence of the secretome.

Methods

MIN6 cells were grown in healthy and diabetic streptozocin (STZ)-induced conditions in MIN6 medium. Both healthy and diabetic cells were treated with the MSC secretome supplemented medium (SSM) and MSC EVs. MSCs were grown in serum-free PPRF-msc6 medium [2]. SSM and EVs were isolated from day 3 of MSC growth. SSM was obtained by centrifuging the MSC expended medium in 3kDa spin filters. EVs were isolated by ultracentrifugation at 100,000 x g. SSM and EVs were re-suspended in MIN6 medium (healthy) or a 10 mM concentration of STZ in MIN6 medium (diabetic). A growth curve was performed over 3 days to analyze proliferation and cell survival.

Results

In comparison to the control (Figure 1a) and EV treated condition (Figure 1b), healthy MIN6 cells treated with SSM (Figure 1c) appeared to have greater cell density and aggregate formation under a light microscope. From Figure 1d, the SSM had the greatest effect on proliferation. STZ-induced diabetic MIN6 cells appeared to have similar aggregate formation and cell density in the MSC EV case and control. In the STZ condition, survival was highest in the presence of the EV fraction.

Conclusions

Adipose derived MSC SSM may have a proliferative effect on healthy MIN6 cells. There is an increase in aggregation and growth for healthy MIN6 cells in SSM. The SSM may contain cell signaling factors that encourage MIN6 cell growth. EVs may help decrease STZ-related death on MIN6 cells. EV supplied medium appeared to have the highest survival rate in the presence of STZ. MSC EVs potentially contain cargo that aids MIN6 cell survival in an induced diabetic cell model.

References

[1] Sarvar et al. *Adv Pharm Bull.* 6(3):293-299, 2016.
[2] Jung et al. *J Tissue Eng Regen Med.* 6:391-403, 2012.

Figures

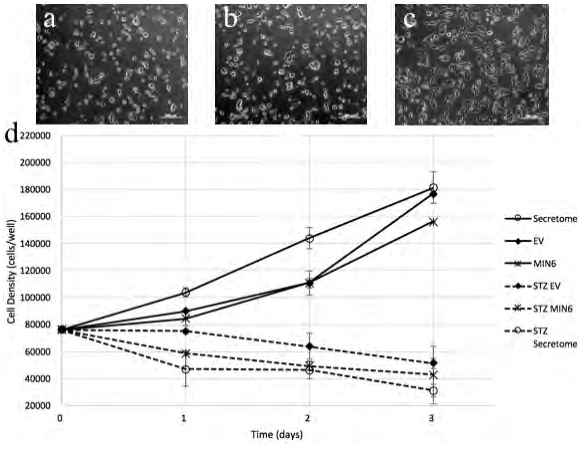

Effect of partial volume correction on QCT-FE predictions of subchondral stiffness

M. Hosseini Kalajahi[1], David R. Wilson[2], James D. Johnston[1]
1. Department of Mechanical Engineering, University of Saskatchewan, Saskatoon, Canada
2. Department of Orthopaedics and Centre for Hip Health and Mobility, University of British Columbia, Vancouver, BC, Canada

Introduction: Mechanical properties of both cartilage and subchondral bone are associated with initiation and progression of degenerative joint disease such as osteoarthritis (OA) [1]. Quantitative computed tomography (QCT) based finite element (FE) modeling has potential to improve our understanding of OA. Nevertheless, validation of QCT-FE models of subchondral bone have indicated moderate predictive accuracy [2]. This might be due to partial volume artifacts (PV) at the bone-cartilage interface, which results in blurring with CT images. Averaging the elastic modulus (E) for elements at the PV layer will result in an E which is equivalent to soft-tissue or low-density trabecular bone. It has been suggested that the intensity information at the PV layer could be restored based on characteristics of adjacent voxels unaffected by PV effects [3]. The objective of this study was to evaluate QCT-FE predictions of stiffness acquired from PV-corrected and original (uncorrected) images in relation to experimentally derived stiffness.

Methods:

Samples: Thirteen proximal tibia compartments were employed in this study (age±SD: 76.2±9.2 years). They were previously imaged using QCT and tested experimentally to determine local subchondral bone stiffness at 47 surface sites [4].

Image Analysis: Initially, CT slices were segmented using the half maximum height (HMH) method [5]. Binary morphological operations were then performed (i.e. image erosion, Boolean subtraction) to create new binary masks for the PV layer and underlying bone. Bone mineral density (BMD) of the PV layer was calculated based on values of inner voxels which were presumably far enough from the corrupted PV layer. The K-nearest neighbors (KNN) algorithm [6] was adopted to find N closest neighbors to each voxel in the PV layer, and their BMD and distance were stored in separate matrices. The inverse distance weighing approach [7] was then used to restore the PV layer by assigning a new BMD to each voxel. The procedure progressed layer-by-layer starting from the inner part of the removed PV layer.

Statistics: Linear regression was used to assess FE predictions in predicting variance (coefficient of determination, R^2) in experimentally derived stiffness. Root mean square error, normalized in relation to maximum experimental stiffness (RMSE%), was used to assess model accuracy.

Results: The PV-corrected FE model explained 80% of the variance in experimental stiffness whereas the original reference model explained 77% variance (Fig. 1). RMSE% was 12% for both the PV-corrected and the original reference model.

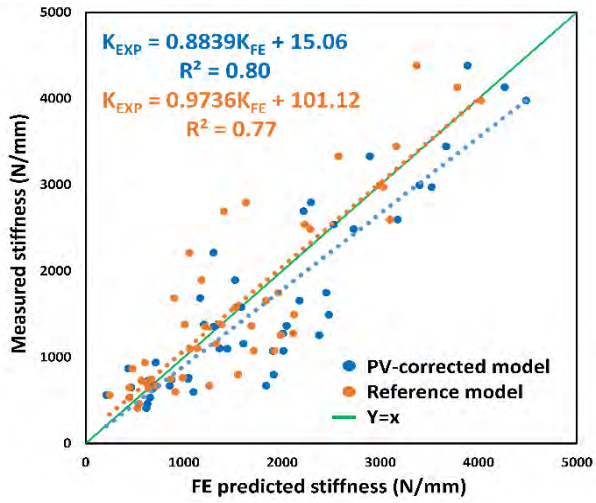

Figure 1. Linear regression between the FE predicted and measured local stiffness. Cortical and trabecular bone modeled with Snyder and Schneider [8] and Goulet [9] E-BMD relationships respectively.

Discussion: Our results indicate that PV-corrected images offered improved predictions of subchondral bone stiffness, though improvements are modest. Further enhancement might be achieved using subchondral-specific trabecular equations or by combining the proposed method with more complex image deblurring algorithm [10]. Nevertheless, these findings indicate that this PV-correction method has potential use for improved QCT-FE modeling of the subchondral bone region.

References [1] Radin et al. 1986, [2] Nazemi et al. 2015, [3] Pakdel et al. 2016, [4] Johnston et al. 2011, [5] Kontulainen et al. 2007, [6] Friedman et al. 1979 [7] Shepard, 1968, [8] Snyder and Schneider, 1991, [9] Goulet et al. 1994, [10] Pakdel et al. 2014

Accounting for Young's modulus variability "inside" elements for subject-specific FE modeling

Nima Ashjaee, Mehrdad Hosseini Kalajahi, James D. Johnston
Department of Mechanical Engineering, University of Saskatchewan, Saskatoon, Canada

Introduction: Subject-specific finite element (FE) modeling has been commonly used for numerical simulation of the biomechanical behavior of bone. With subject-specific FE models, geometry and material properties can be derived from quantitative computed tomography (QCT). Generation of FE model geometries can be achieved using a number of commercially available software packages, as reported in [1]. On the other hand, assigning material properties into FE models usually requires custom, in-house code [2]. To date, most research groups have used an approach which assigns a constant Young's modulus to the entire element of the mesh. With this approach, continuity of material distribution is not considered between elements, and this adversely influences the accuracy of the model [2]. In addition, in this approach, Young's modulus needs to be averaged over certain ranges (known as material binning) which leads to partial volume averaging. An alternative approach is to account for variation of Young's modulus inside an element. This approach improves automation by eliminating the need for material binning and improves the level of accuracy of material properties assignment [2, 3]. This approach should also permit usage of a larger element, and thus lead to a faster processing time, but to date no studies have directly compared the different mapping strategies. The objective of this study was to apply different mapping strategies to FE models to identify which strategy leads to fastest mesh convergence.

Methods: Four tibial samples were used in this study. Macro-indentation tests were previously performed on different indentation sites and local structural stiffness was calculated at each indentation site. A total of 16 tests were used in this study. Prior to testing, samples were imaged with QCT. The bony region of each sample was segmented from the surrounding materials. A smoothed volume was generated and imported into ABAQUS. FE models of tibial compartments were constructed using different element edge length (ranging from 4.0 mm to 0.9 mm). Three different material mapping strategies were used to import material properties from QCT images into FE models: (1) *Element-based:* In this approach material properties were directly assigned to each integration point from the CT images. As the number of integration points inside an element was more than one, spatial variation of Young's modulus was accounted for. (2) *Node-based:* Here, material properties were first assigned to the nodes, and then interpolated at integration points. (3) *Constant-E approach*: Same as node-based, material properties were first assigned to the nodes, then Young's modulus was integrated over the entire volume of element and a constant Young's modulus was assigned to each element. To assess mesh convergence for each mapping approach, normalized root mean squared error (RMSE%) values between two consecutive iterations (more details in [4]) were calculated for each element size and mapping approach.

Results: Figure 1 shows RMSE% values of different mapping strategies with respect to element size. Based on Figure 1, element-based and node-based approaches converged at 2.5 mm, while the constant-E approach converged at 1 mm (similar results previously reported for constant-E approach in our group in [4]). Converged FE models with element-based and node-based approaches ran approximately 60% faster than the constant-E approach. All converged models had similar correlation between experimental and FE results (R^2 ranged from 89-90%).

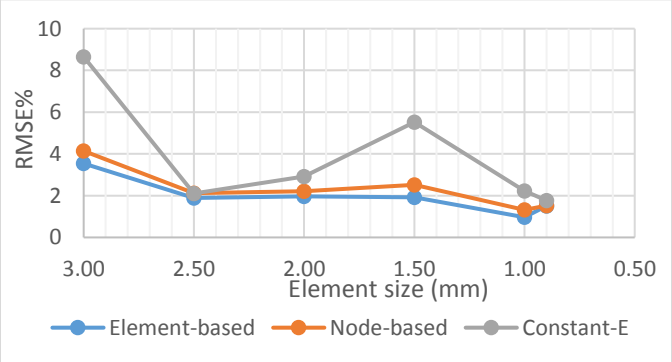

Figure 1. Variation of RMSE for different element sizes and mapping approaches.

Conclusion:

This research indicates strong potential for accounting for variation of elasticity inside elements with subject-specific FE modeling. Since models converge with bigger elements, it markedly reduces the run time.

References

[1] Messmer et al., 2007 [2] Chen et al., 2015 [3] Taddei et al., 2007 [4] Nazemi et al, 2015.

Multiple Sclerosis Lesion Segmentation: Comparison of a Connected-Component Labeling Method with an Open Source Software

Zahra Hosseinpour, Olayinka, Oladosu, Yunyan Zhang
Biomedical Engineering Program, Schulich School of Engineering, Departments of Radiology and Clinical Neurosciences, Hotchkiss Brain Institute, University of Calgary

Introduction

Multiple sclerosis (MS) is a demyelinating and neurodegenerative disease of the central nervous system (CNS) characterized by multi-focal lesions (1). Magnetic resonance imaging (MRI) is very sensitive for identifying lesion pathology but quantitative evaluation of lesion burden is difficult, mainly due to the lack of methods to reliably segment the lesions. In this regard, we are developing a technique based on connected-component labeling (2) and also assessing the utility of an open-source software, Lesion Segmentation Tool (LST), built into an image processing package (SPM8) (3). Results were tested in 4 MS patients recruited into an ongoing clinical trial by comparing with expert labeling, with a focus on FLAIR 3D images and FLAIR and T1-weighted MRI (LST).

Materials and Methods

Method included the following steps:

- Skull Removal: Non-brain tissues were stripped using a different image analysis package, FSL (Oxford, UK), to enhance image quality.
- Image Normalization: MRI field non-uniformity causes variations in image intensity. Consequently, signal intensity normalization was applied to the images (ranging 0-255) with an in-house Python program.
- MS Lesion Segmentation: Image segmentation was done with in-house MATLAB code. First, intensity thresholding was done to remove the brain areas that appeared totally different in signal intensity from that of MS lesions and further processing was done on the resulting binary image. Connected-component labeling was the next step in which connected-components from the binary images were found and the resulting connected groups were separated based on measures of morphological features. Eccentricity, Solidity, Extent and Area were the features used in this step. After this processing, lesions were segmented but some small undesired regions, especially in some gray matter areas, were detected. To spare these regions for a pilot analysis, MATLAB function 'imfreehand' was used interactively. The performance of our own program was compared with results of the LST that uses a lesion growing algorithm, and with the ground truth, which only provided the location of the lesions, not lesion territory, therefore it can be considered a relative reference.

Results

Both methods served well for identifying relatively large lesions, and for lesions with distinct signal intensity. Small gray matter lesions and faint diffuse lesions proved difficulty to segment. For our connected-component labeling method, the mean Sensitivity over the 4 patients was 65% respectively It was 45% for the LST.

Conclusion

This preliminary study showed that our custom-implemented method had better outcome than the LST. However, there are few limitations in our method such as human interaction using 'imfreehand' function. LST was a one-step process and so easy to use. The reason that LST performed poorer even with use of two imaging contrasts (T1 and FLAIR) deserves further interpretation. Although both methods were not so powerful to detect very small lesions. We seek to test the same algorithm in Python as an open source in the future and try to enhance results.

References

1. Lladó X, (2012). I. of Information Sciences. 186(1):164-85.
2. https://en.wikipedia.org/wiki/Connected-component_labeling
3. http://www.statistical-modelling.de/lst.html

Maintenance of Stem Cell Aggregate Sizes throughout Scale-up in Stirred Suspension Bioreactors Enabled by Computational Fluid Dynamic Modeling

Breanna S. Borys[1,3], Erin L. Roberts[1,3], An Le[1,3], Michael S. Kallos[1,2,3]
[1]Pharmaceutical Production Research Facility, [2]Department of Chemical and Petroleum Engineering, [3]Biomedical Engineering Graduate Program, University of Calgary, 2500 University Dr. NW, Calgary, AB, T2N 1N4

Introduction

Stirred suspension bioreactors offer several advantages over planar static culture, making them an increasingly popular platform for stem cell expansion and scale-up. A change in bioreactor scale, however, results in altered hydrodynamic properties that affect cell products - particularly if grown as aggregates. Shear from the local fluid velocity gradient and cell interaction with turbulent eddies influence aggregate sizes, which in turn impact cell pluripotency, differentiation, and proliferation potential [1]. Current scale-up methods maintain single quantity variables that do not capture the variation and complexity of the bioreactor environment. As a result, predicted scale-up agitation rates are often ineffective and damage the cells. This study investigates the use of computational fluid dynamic (CFD) modeling for predicting bioreactor agitation rates that maintain stem cell aggregate size and size distributions throughout scale-up.

Methods

COMSOL Multiphysics was used to model 10-mL and 100-mL stirred suspension bioreactors at various agitation rates (40-140rpm). The simulated steady-state variable trendlines were then linked to predict scale-up agitation rates based on the maintenance of volume average hydrodynamic variables (velocity, shear-rate, and energy dissipation rate). Mouse embryonic stem cells (mESCs) were cultured using these predicted agitation rates that maintain CFD calculated volume average hydrodynamic variables. Resulting aggregate were sized and compared to mESC aggregates cultured using predicted agitation rates from gold standard scale-up methods that maintain: impeller tip shear, tip speed, power consumption or Reynolds number.

Results

Depending on which criteria was used for scale-up, the predicted agitation rate changed greatly, resulting in significant differences in cell growth and aggregate sizes. In addition, small changes to the bioreactor geometry, which could only be accounted for in the CFD simulated models, had significant effects on cell growth and aggregate sizes. It was determined that if the volume average energy dissipation rate or maximum shear stress were kept constant, aggregate sizes could be maintained throughout scale-up.

Conclusions

Unlike traditional equations, CFD modeling accurately accounts for differences in the hydrodynamic environment that result from changes in reactor shape or size. Thus, it is suggested that maintaining the CFD derived volume average energy dissipation rate is the best method for scale-up of stem cell aggregate culture.

References

1. C. Bauwens, et al, "Control of human embryonic stem cell colony and aggregate heterogeneity influences differentiation trajectories," *Stem Cells*, vol. 26, no. 9, pp. 2300-2310, 2008.

Figure

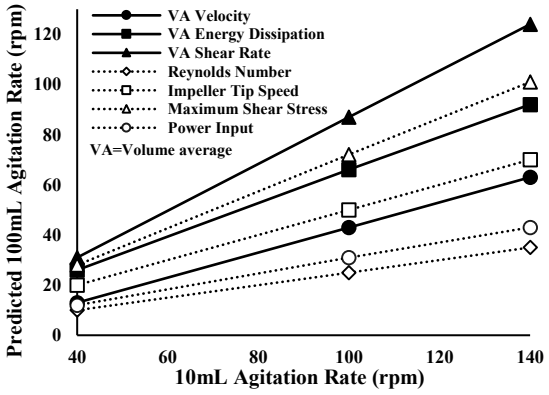

Corresponding 10-mL to 100-mL predicted bioreactor agitation rates that result from using various scale-up methods

Normative: A Research Translation Portal for Generating, Disseminating and Sharing HR-pQCT data

Syed M. Jafri, Bryce A. Besler, Lauren A. Burt, Steven K. Boyd
University of Calgary, Calgary, Alberta

Introduction

Dual-energy x-ray absorptiometry (DXA) is the clinical standard for assessing bone health. DXA typically measures areal bone mineral density (aBMD) at the lumbar spine and femoral neck as a correlate to fracture risk. To provide meaning to aBMD measurements, a T-score is computed comparing a subject's aBMD to an age- and sex-matched healthy, young individual. However, DXA has fundamental systematic limitations restricting the diagnostic accuracy of aBMD [1].

High-resolution peripheral quantitative computed tomography (HR-pQCT) captures the three-dimensional distribution of osseous tissue at peripheral skeletal sites allowing more accurate assessment of fracture risk [2]. However, standard HR-pQCT assessment produces 12 variables that are challenging to interpret, even by a trained researcher. Recently, a large-scale study involving 866 patients from the Canadian Multicentre Osteoporosis Study (CaMos) was used to generate normative HR-pQCT data [3]. Here, we introduce Normative, a web-based portal that provides researchers and clinicians centile information about HR-pQCT variables, similar in interpretability to the T-scores of DXA (https://normative.ca).

Methods

A file containing the 12 HR-pQCT variables for any number of subjects is dropped into the Normative online tool. Researchers and clinicians are provided with data outputted in percentiles and plotted on standardized graphs generated from the original publication [3]. Automatically, a secure and unique credential is provided for each patient to access their data through a user-friendly patient report (Figure 1). All data processed, used and stored in Normative is unidentifiable patient data.

Results

The portal fulfills an objective for each stakeholder in a scientific study:

1. Provide researchers with the reference data to compare individuals and special cohorts to an age, sex and site matched database.
2. Improve a clinician's ability to assess bone health by providing a standardization of clinically relevant HR-pQCT measurements.
3. Increase patient engagement and ownership of health through the transparent accessibility of data in a precise and easy to understand format.

Conclusion

Normative has the potential to become an international tool designed to combine HR-pQCT datasets. We have already demonstrated the foundational knowledge necessary to add new special populations to Normative for specialized uses such as pediatric or geriatric populations in the future. In the near future, we hope to add European and Asian cohorts to the Normative database for researchers across the globe to compare and contrast populations of interest at an international level.

References

[1] Bolotin. Bone. 2007
[2] Nishiyama *et al*. Osteoporos Int. 2012
[3] Burt, *et al.* JBMR. 2016

Figures

Figure 1. Sample Patient Report displaying 12 common HR-pQCT variables in percentile form as generated by Normative. A production server is set up at https://normative.ca.

Effects of Cracks on Local Strain Distributions in Articular Cartilage

Saad Luqman, Amin Komeili, Ziad Abusara, Walter Herzog
University of Calgary, Calgary, AB, Canada

Introduction

Cracks and lesions on the surface of articular cartilage are a hallmark of osteoarthritis (OA). However, the mechanisms by which cracks affect the functions of cartilage are not fully understood. Therefore, the objective of this study was to measure the axial strain near the crack edges, and compare it with the local tissue strain in the intact regions at the same cartilage depth under static and dynamic loads. We expected to see excessive deformations near the crack edges in both transient and steady states. The results of this study may help in understanding the mechanisms that lead to the high cell death rate around a crack, and damage propagation in a fractured or cracked cartilage, in the early and late stages of OA.

Methods

Cartilage samples were extracted from pig-knee joints, and fixed in our custom compression testing device for experiments. Two cuts were created in each sample, one in the middle zone (MZ) and one in the superficial zone (SZ). To measure local strains near the cut, three squares, 15 x 15µm, were burned within 5µm of the cut edges using a 110mw laser. Three corresponding squares were burnt at the same depth, 300µm away from the cut, representing the intact area (Figure 1-a). The samples were then imaged continuously during the 10% and 15% ramp compression, for the SZ and the MZ cuts respectively, followed by 5 minutes of stress relaxation (S.R.). The local strains were calculated by measuring the change in the length of the fiducial squares during the compressions. The axial strains of the squares were compared using the Wilcoxon Signed-Rank test.

Results

The compressive strains near the cut edges, i.e. Marker 1 and 2, were not statistically different (Figure 1-b and c). Similarly, no difference was detected in the axial strains of markers 1* and 2* in the intact regions (Figure 1-b and c). Also, no difference was obtained between the local axial strains of marker 3 at the cut tip and the corresponding marker 3* in the intact area (Figure 1-b and c). However, markers near the cut edges were compressed up to 100% more than those in the intact area at the same depth from the surface for nominal strains larger than 5% (Figure 1-b and c).

Conclusion

At nominal strains smaller than 5%, the average local axial strain in markers 1, 2 and 3 were larger than the corresponding strains observed at markers 1*, 2* and 3*. However, the difference in the means was not large enough to result in a significant difference. With further compression, the difference in the strains increased and was up to 100% larger for the markers near the cut edges compared to the corresponding strains obtained in the intact areas. The increased strains near the cartilage crack may be the cause for the increased cell death rate and damage propagation observed experimentally, which may affect the function of cartilage in the long term.

Figure

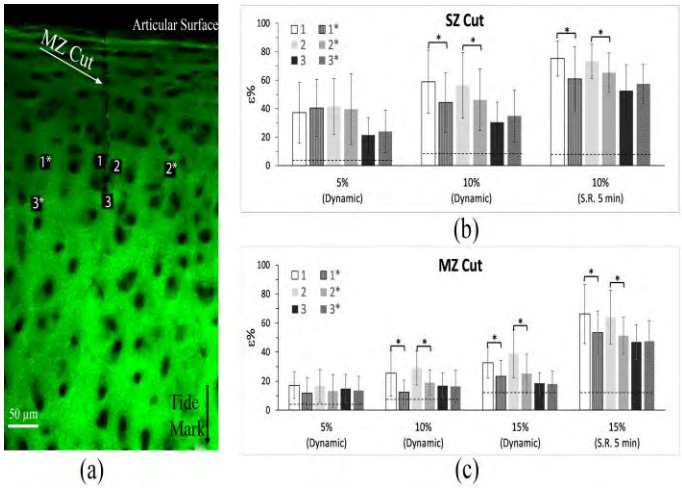

Figure 1 - (a) Three pairs of burned squares in a cartilage sample (MZ). (b,c) Axial strains of markers in samples with SZ and MZ.

Enhanced Cell-Substrate Impedance Sensing for Neuronal Differentiation Monitoring

Mohsen Janmaleki, Masoud Pahlevaninezhad, Amir Sanati-Nezhad
BioMEMS and Bioinspired Microfluidic Laboratory, Department of Mechanical and Manufacturing Engineering, University of Calgary,

Introduction

Non-invasive and real-time monitoring of differentiation procedure is highly demanded in tissue engineering and neuroscience research. Impedance spectroscopy is a high sensitive technique with convincing results in monitoring of different cellular behaviors such proliferation and differentiation. The technique is, however, highly dependent on number of cultured cells and coverage over electrodes. In this study, a new microelectrode array and image processing algorithm is employed to compensate the alterations in morphology and cell density for neuronal induction of rat bone marrow mesenchymal stem cells (rBMSCs).

Methods

The impedance measured from rBMSCs cultured over biosensor (interdigitated electrodes, IDEs) during differentiation to neural cells. The data was normalized by estimated covering surface area and cells population. Moreover, the effect of cells density and morphological changes were taken in account using an image processing algorithms. Expressions of specific neurotrophins (MAP2, GDNF, CNTF, BDNF, Dppa5a were assessed using real-time PCR to evaluate the induction and used to prove the capability of our novel approach for monitoring of neuronal differentiation with minimum influence from morphological alterations. The rBMSCs isolated from 6-8 week-old rat were cultured over IDEs and differentiated using neural induction medium containing 10 ng/ml basic fibroblast growth factor, butylated hydroxyanisole, forskolin, KCL, valproic acid, and human regular insulin [1].

Results

The direct measured impedance did not show significant alterations during differentiation. However, exposing to neural differentiation media caused the well-spread spindle shape rBMSCs to have shrunk body in the very early hours of treatment and then neurite formation started. The cells became fully differentiated after 20 hrs and the number of the viable cells decreased significantly. Taking these two critical factors in the measured impedance revealed this non invasive parameter is able to demonstrate differentiation in real time manner. In Fig.1 the schematic of the biosensor (a) with the applied electrical model containing cells elements (R_{cell} and C_{cell}) and sensor element (Z_{cpe}, C_p, R_p) and medium resistance (R_s) are shown. Differentiated cells (c) with measured impedance amplitude and phase in the differentiation time course (d) with normalized data with cell populations and covering area (e) are also shown.

Conclusions

This study demonstrated that through considering of morphological and density dynamics of cells, the differences in cell electrical properties can be utilized to monitor adult stem cell differentiation toward neuronal-like cells in real-time and label-free.

References

[1] D. Woodbury et al. Adult rat and human bone marrow stromal cells differentiate into neurons. J Neurosci Res 2000, 364–70

Figures

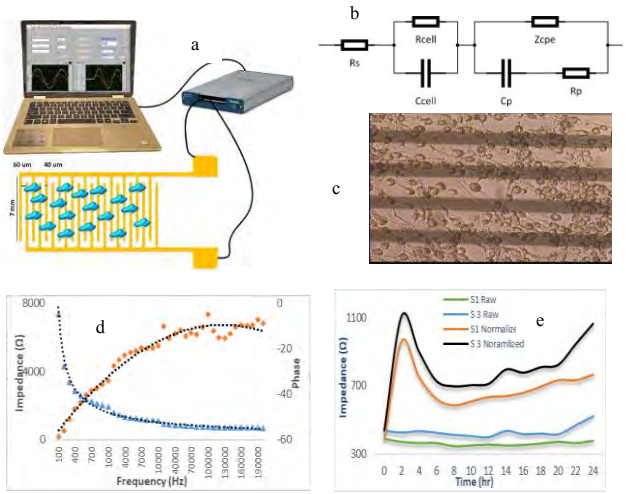

Is prebiotic fibre supplementation effective in preventing structural changes in vastus lateralis muscle in a rat model of obesity?

John Michaiel[1,2], Jaqueline Lourdes Rios[2,3,4], Ruth Seerattan[2], Walter Herzog[2,4]
[1]Cumming School of Medicine, University of Calgary, AB, Canada;
[2]Human Performance Laboratory, University of Calgary, AB, Canada; [3]CAPES Foundation, Brasíllia, DF, Brazil; [4]McCaig Institute for Bone and Joint Health, University of Calgary, AB, Canada.
john.michaiel@ucalgary.ca

Introduction

Obesity has been associated with a variety of co-morbidities and chronic diseases, including musculoskeletal disorders. Using a Sprague Dawley rat model, it has been shown that a high-fat/high-sucrose (HFS) diet leads to increased body fat, systemic inflammation, and intramuscular lipid deposition within 12 weeks (1). Dietary prebiotic fibre supplementation is thought to prevent muscle degeneration normally observed in these obese animals. It has been shown that prebiotics attenuate body weight/fat in murine and human models of obesity, and increase metabolic health (2). Therefore, the purpose of this study was to determine the effect of dietary prebiotic fibre supplementation on vastus lateralis integrity in rats exposed to a HFS diet.

Methods

Twenty Sprague Dawley rats were randomized into either a HFS diet (40% fat, 45% sucrose – HFS, n=10) or a HFS diet combined with a dietary prebiotic fibre supplementation (10% oligofructose – HFS+F, n=10) group. Body mass was tracked weekly, and the percentage of body fat was measured at the end of the 12-week intervention period. Following the intervention period, the vastus lateralis muscle was harvested, and histological muscle sections were stained with Oil Red O (ORO,) and Picrosirius Red, for quantifying muscle lipid and collagen content, respectively.

Results

Animals in the HFS+F group had a smaller increase in weight than animals in the HFS group across all time points ($p<0.05$) (figure 1). However, prebiotic fibre supplementation had no effect on the increase in body fat observed in the HFS group animals ($p=0.219$). Prebiotic fibre supplementation was also not effective in preventing lipid infiltration ($p=0.912$) or collagen deposition ($p=0.886$) in the rat vastus lateralis muscle.

Conclusions

Prebiotic fibre supplementation was not effective in preventing lipid infiltration and collagen-based fibrosis in the vastus lateralis muscle of animals exposed to a HFS diet. However, it prevented the excessive increase in body weight normally seen in animals fed the HFS diet. We speculate that fibre supplementation was not effective at improving metabolic health in the experimental animals and regulate hormone level in a way to prevent structural muscle damage typically associated with obesity.

References

1. Collins *et al.* J Orthop Res, 2069-2078, 2016
2. Cluny *et al.* Obesity, 769-778, *2015.*

Figure

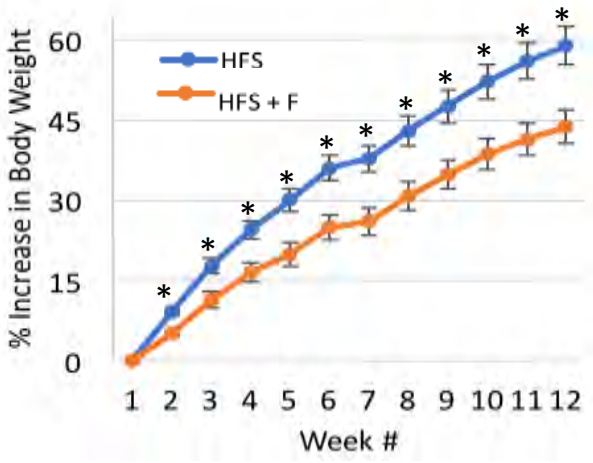

Figure 1: Increase in body weight, expressed as a percentage of the weight just prior to the diet intervention, in HFS and HFS + F groups animals. * indicates $p<0.05$.

Development and Usability Testing of a Surgical Guide for Autologous Breast Reconstruction

Jumana Joury[1], Heather Logan [1, 2], Gordon Wilkes [2], Jason Carey [1], Daniel Aalto [1, 2]
[1]University of Alberta, Edmonton, AB
[2] Institute for Reconstructive Science in Medicine, Misericordia Community Hospital, Edmonton, AB

Introduction

Breast cancer is the most common cancer in women with more than two thousand new cases diagnosed every year in Alberta[1]. Women endure both physical and psychological hardships from the disease and treatment[2]. Often, breast reconstruction surgery is considered apart of the treatment process to improve rehabilitation[3]. Despite the advancements in surgical technique, the current methods to pre-operatively plan for a symmetrical outcome are limited, and the final result is left to the subjective assessment of the surgeon intraoperatively[4]. This challenge is a result of the complexity of surgical manipulation, as well as the deformative nature of soft tissue[5]. The focus of this project is understanding how 3D modelling can be used as a tool to assist Plastic Surgeons in the planning of breast reconstruction surgery.

Methods

The experimental method included observing clinical work, specifically various breast reconstructive surgeries with several plastic surgeons. In parallel to clinical observations, conducting a detailed review of the literature to understand how design concepts have supported other clinical applications, for example, surgical design in planning of maxillofacial bone reconstruction.

Results

Three main concepts were identified which are key to bridging the gap between digital modeling tools, and the current clinical practice of breast reconstructive surgery. A summary of those include:

- Using engineering tools to establish a digital pathway (see figure 1)
- Understanding the surgical procedure
- Applying concepts of Human-Centered Design

Once the key concepts were identified, a workflow, as seen in figure 2, was developed. This demonstrates the process of designing, and prototyping a patient specific surgical guide for breast reconstruction.

Conclusions

This approach to designing a custom surgical guide is novel. We anticipate that the proposed workflow will inform the path of how modeling tools could support Plastic Surgeons in autologous reconstruction. Our future steps include testing this experimental design within the coming year.

References

1: Surveillance & Reporting: 2012 Report on Cancer Statistics in Alberta. Edmonton: CancerControl AB, Alberta Health Services, 2015
2: American Cancer Society, “Breast Cancer”, American Cancer Society, Atlanta, 2016.
3: B. R. A. Day. [Online]. Available: http://www.bra-day.com/breast-reconstruction/.
4: M. C. Ferreira, "Evaluation of Results in Aesthetic Plastic Surgery: Preliminary Observations on Mammaplasty," Cosmetic Special Topic, vol. 106, no. 7, p. 1630, 2000.
5: J. C. Grotting and P. C. Neligan, "Chapter 17: Free TRAM Breast Reconstruction," in Plastic Surgery: Volume 5 Breast, New York, Elsevier Health Science, 2012, p. Chapter 17: Free TRAM breast reconstruction.

Figures

Figure 1 Representation of a Digital Pathway

Figure 2 Research Workflow

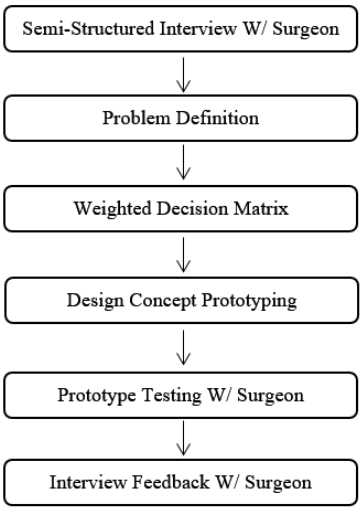

Influence of Intraarticular Contrast Agent on Measures of Bone Microarchitecture in the Knee using HR-pQCT

Geoffrey J Michalak[1,3], Richard Walker[3,4,5], Steven K Boyd[2,3,4]
[1]Biomedical Engineering Graduate Program, University of Calgary; [2]Schulich School of Engineering, University of Calgary; [3]McCaig Institute for Bone and Joint Health; [4]Department of Radiology, Cumming School of Medicine, University of Calgary; [5]Alberta Health Services

Introduction

Osteoarthritis (OA) is the most common articular disease, presenting as degradation of articular cartilage and underlying bone. While arthritic degradation affects both bone and cartilage, no single imaging modality concurrently captures these changes. The clinical gold standard of magnetic resonance imaging (MRI) is ideal for capturing alterations in soft tissues such as cartilage degradation, but lacks the ability to resolve elements of bone microarchitecture, components of the pathology are overlooked[1]. 3D bone imaging, with resolutions of 61µm, has recently been established through use of high resolution peripheral quantitative computed tomography (HR-pQCT) for the quantitative assessment of microarchitecture. Contrast enhanced HR-pQCT is being investigated as a tool to concurrently provide information on cartilage morphology as well as bone microarchitecture. However, use of high attenuation contrast agent increases the risk of beam hardening and photon starvation artifacts as well as other errors which may affect the ability to quantify microarchitecture accurately. The purpose of this study was to validate measures of bone microarchitecture captured by contrast enhanced HR-pQCT imaging. It was hypothesized that intra-articular contrast agent injection would have minimal effect on measured bone microarchitectural parameters.

Methods

Intact knees were harvested from fresh cadavers (n = 10). Knees were scanned using HR-pQCT without contrast agent, and following intra-articular injection of non-ionic contrast agent (iohexol, GE healthcare, Chicago, IL, USA). Weight bearing regions of interest were selected and bone microarchitecture evaluated within three bone volumes below the articular surface.

Results

Differences between bone microarchitectural parameters measured with HR-pQCT or with contrast enhanced HR-pQCT were found to be less than least significant change values reported in literature for all measured parameters[3]. Intraarticular contrast agent injection does not appear to influence bone microarchitectural parameters measured with HR-pQCT.

Conclusions

HR-pQCT is uniquely poised to allow for quantification of bone microarchitecture as well as cartilage morphology with the use of contrast agent. Validation of bone microarchitectural parameters ensures that accuracy is not sacrificed by the addition of cartilage data acquisition. Future work will focus on validation of cartilage measures. If the process by which whole joint changes occur can be better understood, disease mechanisms may be identified, highlighting therapeutic targets. Establishing a knowledge base for understanding whole joint alterations can support clinical treatment decisions and guide development of preventative measures.

References

[1]Lohmander, L.S. et al. (2007) Am. J. Sports Med.
[2]Barret, J. et al. (2004) RadioGraphics
[3]Manske, S. et al. (2017) J. Bone Miner Res

Figures

Fig1: Contrast agent induced beam hardening in thoracic CT[4]

Miniaturized biosensor for the diagnosis of Central nervous system (CNS) injuries.

Sultan Khetani, Chantel Debert, Patrick Whelan, Arindom Sen, Amir Sanati-Nezhad

Introduction

Injury of the Central nervous system (CNS) results in the release of biomarkers in the bodily fluids. These biomarkers have proven to be highly sensitive for the detection of the injury (1). Accurate detection and quantification of these injury biomarkers can expedite the process and reduce the cost of diagnosing (2). Therefore, we developed a biosensor for the detection of Glial fibrillary proteins (GFAP), a diagnostic marker of CNS injuries. This highly sensitive and selective biosensor is able to quantify GFAP concentration between 1 picogram (pg) /ml-10 nanogram (ng)/ml range.

Methods

Highly conductive three lead graphene electrode was modified for the biosensing of GFAP. For detecting GFAP, electrode surface was covered with branched Polyethyleneimine (PEI) then reduced with Glutaraldehyde resulting in the formation of 'imine' functional group. This allowed binding of monoclonal GFAP antibody. After the immobilization of the antibody, bovine serum albumin (BSA) was used for blocking unbounded sites. Biosensor thus created was characterized using Fourier Transform Infrared spectroscopy (FTIR), Impedance spectroscopy, and then GFAP samples prepared in phosphate buffered Silane, human serum, artificial cerebrospinal fluid, and spinal cord injury patient samples were tested.

Results

FTIR test found two distinct peaks between wavelengths of 1450 and 1600 confirming the presence of 'imine' functional group on the biosensor (Fig.1). Electrical characterization performed in presence of redox probe showed a distinct impedance responses for change in the conductivity of the surface. Detection of GFAP offered detection the limit between 1 picogram/ml – 10 nanogram/ml (Fig.2). Highly selective performance of the biosensor was observed when tested in presence of several neurotransmitters and proteins which are released after the injury. For validation of the performance, known and unknown GFAP concentrations were tested with the biosensor and Enzyme-linked immunosorbent assay (ELISA). Highly stable and correlated responses were observed between the two systems.

Conclusions

Quantitative, impressive limit of detection (1pg/ml-10ng/ml) and a highly selective and sensitive GFAP detection for the diagnosis of CNS injury is achieved. This miniaturized biosensor is simple to use and can find application as a bed-side testing and point of care diagnostic device.

References

1. World Health Organization, and International Spinal Cord Society. *International perspectives on spinal cord injury*. World Health Organization, 2013.

2. Khetani, Sultan, et al. "Immunosensing of S100β biomarker for diagnosis of spinal cord injuries (SCI)." *Sensors and Actuators B: Chemical* 247 (2017): 163-169.

Figures

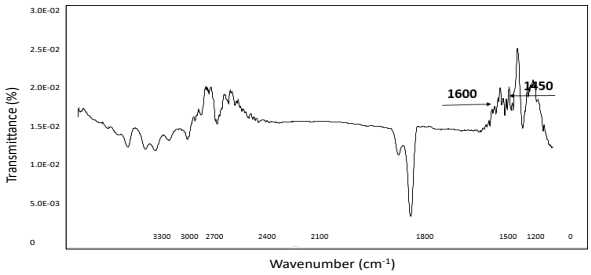

Fig 1: Characterization of the biosensor using FTIR

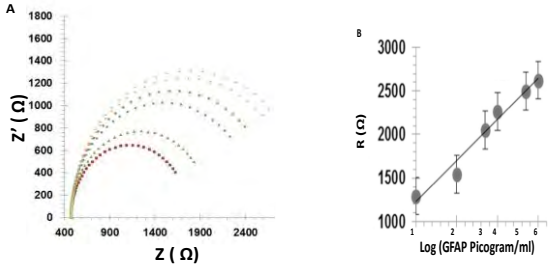

Fig 2: Impedance response to GFAP concentrations. (a)Nyquist plot (b) Normalized impedance

Novel metabolomics based microfluidic chip for ultra-rapid antibiotic susceptibility testing

Mehdi Mohammadi, Thomas Rydzak, Ryan Groves, Yasaman Samanian, Deirdre Church, Ian Lewis, Amir Sanati-Nezhad

Over the recent years, there is a growing need for lab-on-a-chip devices, particularly in clinical analysis and diagnostics. Using microfluidics platform can reduce the amount of patient sample and the turnaround time of bio procedure in multiple bioassay, i.e., rapid blood testing, Point of care testing.

The reducing time of blood analysis and antibiotic susceptibility testing is a vital step to survive patients who suffer from a bloodstream infection (BSI) and sepsis [1]. Currently, it takes 2-5 days to identify BSI pathogens and perform antibiotic susceptibility testing. Patients who receive the wrong antibiotic over this time are ten times more likely to die and even a single day receiving an ineffective antibiotic increases mortality by 8% [2]. Different microfluidic devices have been developed for antibiotic susceptibility testing (AST) [3], i.e. Sepsis diagnostics using bacteria separation [4] see review [5], [6]. However, the aforementioned methods utilized direct and indirect monitoring of bacteria for AST, which it is not precise enough to utilize as a clinical tool. Suggested microfluidic device in the current work is metabolomics based and could implement antibiotic susceptibility testing in less than 5 hours and could be utilized as clinical device.

Conventional photolithography and soft lithography methods utilized to fabricate considered device.

The considered microfluidic device is fabricated in three layers to automate antibiotic resistance testing. Antibiotic and media automatically mixed to generate three concentrations in the top layer. Then it aliquoted into middle porous membrane and finally directed to incubation chambers in microbial layer (bottom layer). After 4 hours incubation time, directed to mass spectrometry device for metabolic analysis. Type of bacteria and minimum inhibitory concentration (MIC) for AST, are detected successfully.

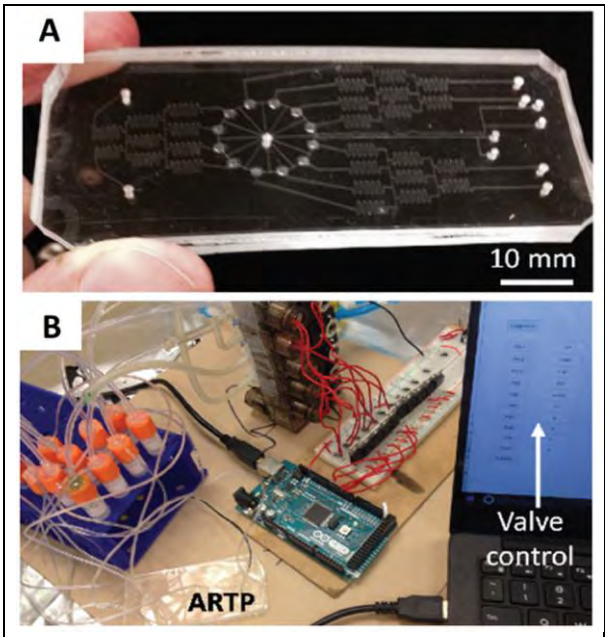

Fig 1. (a) Fabricated microfluidic chip (b) experimental setup.

Conclusions

A novel microfluidic platform for antibiotic resistance testing have developed and the AST completed in less than 5 hours.

[1] A. Kumar *et al.*, *Crit. Care Med.*, vol. 34, no. 6, pp. 1589–1596, 2006.

[2] M. A. Faridi *et al. J. Nanobiotechnology*, vol. 15–3, no. December, 2017.

[3] J. Campbell *et al* ." *Biomed. Microdevices*, vol. 18, no. 6, pp. 1–11, 2016.

[4] S. Zelenin *et al. Biotechnol. Lett.*, vol. 37, no. 4, pp. 825–830, 2015.

[5] J. Dai *et al. Bioengineering*, vol. 3, no. 4, p. 25, 2016.

[6] A. Tay *et al. Biotechnol. Adv.*, vol. 34, no. 4, pp. 404–421, 2016.

Tuning the Elastic Modulus of Bio-Compatible Hydrogels

Emily Kuervers[1], Mohsen Janmaleki[1], Mahdi Moezzi[1], and Amir Senati-Nezhad[1]
[1]BioMEMS and Bioinspired Microfluidic Laboratory, Biomedical Engineering Program, Department of Mechanical and Manufacturing Engineering, University of Calgary, Canada

Introduction

"Organ-on-a-chip" devices are micro-scale models of different organs that can be used to replace animal testing. To properly model a human skin layer on such a device, the dermal and epidermal skin layers must be present along with a porous layer. The proliferation of the epidermal cells is dependent on the mechanical properties of the surface that the epidermal cells are being cultured on. [1] GelMA is a photocrosslinkable, biocompatible, and biodegradable hydrogel which has tuneable mechanical properties and therefore facilitates the modelling and replication of different cell matrices. Changing either the gelatin concentration in the GelMA or the UV exposure can control the hydrogel's behaviour. The purpose of this project was to test and observe the different effects these two variables on the Elastic modulus of GelMA to optimize it for the epidermal layer.

Methods

The Elastic modulus of the GelMA was measured using atomic force microscopy (AFM). This method allows the user to test thin membranes without disturbing the sample. The AFM reflects a laser off of a cantilever and measures the changes in deflection. The spring constant and the conversion factor of the cantilever are first calculated by performing a frequency response test and a force-distance curve on a hard surface. Next, the different samples are tested by performing a force-distance test on the surface. The tests were performed on 5%, 10%, 15%, and 20% concentrations of gelatin with varying curing times of 5s, 10s, 20s, and 30s. The data was then normalized and fit to the Hertz model equation for a parabolic cantilever tip using custom Matlab code. Compression tests of GelMA were also performed on bulk samples and fit into stress-strain curves to compare the calculated Elastic modulus.

Results

There was a clear increase of the elastic modulus as the concentration in the GelMA increased. No direct correlations were found between the elastic modulus and the curation time. On average, the bulk samples of GelMA had an elastic modulus of 2.04 kPa for 5%, 3.70 kPa for 10%, 9.02 kPa for 15%, and 45.33 kPa for 20%. The AFM methodology to obtain the Elastic modulus was successfully confirmed by using polydimethylsiloxane (PDMS) and comparing the calculated values with the literature values. However, the AFM was unable to obtain results for the GelMA as the cantilever tip perforated the surface of the sample due to strong attraction forces.

Conclusion

In vivo, the epidermal layer of skin has an Elastic modulus of approximately 25kPa. [2] Controlling the concentration of the gelatin in the GelMA was found to be the most consistent way to control the Elastic modulus of the sample. Therefore, a concentration value between 15 and 20 % would be ideal for the epidermal culturing if 25 kPa is to be achieved. A cantilever with a microbeaded tip will be used to perform further tests of the thin films using the AFM.

References

[1]G. Ebersole, P. Anderson and H. Powell, "Epidermal differentiation governs engineered skin biomechanics", Journal of Biomechanics, 2010.

[2] X. Liang and S. Boppart, "Biomechanical Properties of In Vivo Human Skin From Dynamic Optical Coherence Elastography," IEEE Transactions on Biomedical Engineering, 2010.

Adaptive global signal extraction based on spatiotemporal decomposition of fMRI Images

Narges Moradi, Mehdy Dousty, Roberto C. Sotero

Biomedical Engineering Graduate Program, University of Calgary, Calgary, Canada

Introduction

In this paper, the large-scale spatio-temporal dynamics of functional connectivity in resting-state and task-related fMRI is investigated [1]. In order to decompose fMRI images into Spatial and Temporal Intrinsic Mode Functions (SIMF and TIMF respectively), Empirical Mode Decomposition (EMD) [2] based methods, Fast and Adaptive Tridimensional EMD (FATEMD) [3] and Improved Ensemble EMD with Adaptive Noise (ICEEMDAN) [4] are utilized. While Fourier based transform is based on linearity assumptions, EMD is an adaptive data-driven method which is widely used to analyze nonlinear and nonstationary phenomena. It decomposes any signal into its fundamental nonlinear functions, or IMFs, by means of a sifting process [1].

Methods

We applied FATEMD to decompose motor task and resting-state fMRI data from 10 subjects into SIMFs. Subsequently, ICEEMDAN method was used to decompose each SIMF into its corresponding TIMFs. TIMFs and SIMFs were examined to explore the spectral information of fMRI signals. Since there are no particular textures and oscillations available after 5th spatial and 3rd temporal IMFs, those values were set as an optimum decomposition number for SIMF and TIMF, respectively. Connectivity matrices were constructed by computing correlation coefficients between all possible pairs of STIMFs and TIMFs for all brain regions comprised in the AAL 116 atlas [5]. Thus, instead of the classical functional connectivity matrix, the decomposition presented here produces 5*3 = 15 connectivity matrices encompassing the rich spatiotemporal dynamics of brain activity. To assay global and local connectivity patterns at multiple time-frequency scales,, topological measures such as transitivity and efficiency were computed.

Results

We found high levels of segregation and integration, for both task-related and resting state activity, in 3th, 4th, and 5th SIMFs (mean 0.8736 ± 0.0604). On the other hand, first and second SIMFs showed low variation (mean 0.1840 ± 0.0364). Moreover, integration was greater than segregation especially for the first and second SIMFs (integration: 0.1533 ± 0.0172, segregation: 0.2147 ± 0.0165), whereas 3th, 4th, and 5th SIMFs did not show significant differences (integration: 0.8728 ± 0.0633 , segregation 0.8743 ± 0.0637).

Discussion

The current methodology for the analysis of fMRI signals relies on subtracting the global signal (GS) (i.e average of the activities from all voxels). However, the efficiency of this approach is highly controversial due to producing spurious results [6]. Given the extremely high level of integration and segregation in the low spatial domain, namely 3th, 4th, and 5th SIMFs, our results suggest they could be considered as a global signal masks. Thus, this study introduces a novel adaptive nonlinear method to identify GS.

References

[1] Al-Baddai, s. et al., Biomedical Signal Processing and Control, 13, 218–236, 2014.

[2] Huang, N. E. et al., *Proc. R. Soc. Lond.* A454, 903–995, 1998.

[3] Riffi, J. et al., Multidim Syst Signal Process, 1–12, 2014.

[4] Colominas, M. A. et al., Biomed. Signal Process. Control, vol. 14, pp. 19–29, 2014.

[5] Tzourio-Mazoyer, N. et al., NeuroImage, vol. 15, 273-289, 2002.

[6] T. Liu, T. et al., NeuroImage, 150, 213–229, 2017.

Chondrogenic Differentiation of Synovial Fluid Mesenchymal Stem Cells on Human Meniscus-Derived Decellularized Matrix Requires Exogenous Growth Factors

Yan Liang, Enaam Idrees, Alexander Szojka, Stephen Andrews, Melanie Kunze, Aillette Mulet-Sierra, Nadr M. Jomha, Adetola B. Adesida
Department of Surgery, University of Alberta, Edmonton, AB

Introduction: The functional properties of menisci are provided by the meniscus fibrochondrocytes (MFCs)-derived extra-cellular matrix (ECM). Previous study showed that cartilage-derived decellularized matrix (DCM) induced chondrogenesis of mesenchymal stem cells (MSCs) without growth factors[1]. Likewise, TGFβ and IGF1 signaling have been identified as regulators during embryonic meniscus morphogenesis[2]. Also, our previous study showed that hypoxia (HYP) enhanced chondrogenic capacity of bone marrow-derived MSCs[3]. Inspired by these results, our objective was to test if meniscus-derived DCM can induce differentiation of synovial fluid-derived MSCs (SF-MSCs) towards an MFC-like phenotype under HYP and whether these effects can be enhanced by TGFβ3/IGF-1.

Methods: Human SF-MSCs were isolated from knee joint synovial fluid (n=5, male, 18-57 years old) and expanded until passage 2 (P2) under HYP (3% O_2). Normal human meniscus tissue from a cadaver (male, 46 years old) was homogenized into a slurry. After freeze-drying, porous DCM scaffolds 6 mm in diameter were cut and sterilized using ethylene oxide. SF-MSCs (5×10^5) were seeded per scaffold and then cultured in serum-free medium with (+) or without (-) TGFβ3/IGF1 under HYP for 21 days. A cell pellet culture was used with either +TGFβ3, +IGF1, or both +TGFβ3/IGF1 for comparison to the DCM scaffolds and to test the effects of individual growth factors. These bioengineered tissues were assessed biochemically for glycosaminoglycan (GAG) production, histochemically for proteoglycan deposition, by scanning electron microscopy (SEM) for cell and DCM morphology, and by qRT-PCR for ECM gene expression.

Results: The total GAG content in DCM+TGFβ3/IGF1 was significantly higher compared to DCM-TGFβ3/IGF1, which was correlated with the safranin O staining. Safranin O positive proteoglycan ECM was observed throughout DCM+TGFβ3/IGF1. Although deposition of ECM was noted in DCM-TGFβ3/IGF1, no safranin O staining was observed. TGFβ3 only and the combination of TGFβ3/IGF1 tended to stimulate more GAG content in pellets compared to IGF1 only. Safranin O positive staining occurred in pellet+TGFβ3 and pellet+TGFβ3/IGF1 while pellet+IGF1 stained negative. SEM analysis of DCM revealed the porous structure of the empty DCM. The structure of DCM-TGFβ3/IGF1 was modified by flat-shaped fibroblastic-looking SF-MSCs while round chondrocyte-like SF-MSCs appearing to form collagen-looking fibers were observed on the DCM+TGFβ3/IGF1 surface. Significantly higher ECM gene expression of *ACAN*, *COL1A2*, *COL2A1*, and *SOX9* were found in +TGFβ3 and +TGFβ3/IGF1 compared to IGF1 only while no differences were observed between +TGFβ3 and +TGFβ3/IGF1 in pellets. In DCM scaffolds, the addition of TGFβ3/IGF1 induced higher ECM gene expression compared to pure DCM without growth factor supplementation, but the statistical significant differences were only found in *COL1A2* and *SOX9*.

Conclusions: The meniscus-derived DCM requires exogenous growth factor supplementation to differentiate SF-MSCs. The stimulatory effect of TGFβ3 and IGF1 on SF-MSCs within the DCM can promote an MFC-like phenotype with GAG-rich matrix formation *in vitro*, which could lead to a cell-based implant to repair non-healing meniscal lesions.

References:
(1)Cheng, *et al*.,Tissue Eng Part A,2009. (2)Pazin, *et al*., J Orthop Res, 2014. (3)Adesida, *et al*., Stem Cells Res Ther, 2012.

Non-invasive microfluidic-microwave sensor for contactless pH analysis of E. Coli

Rakesh Narang, Mohammad Hossein Zarifi, Mojgan Daneshmand, Amir Sanati-Nezhad
2500 University Dr NW, Calgary, AB T2N 1N4

Introduction

Currently, there has been a huge push in industry to develop bacterial sensors, as food safety and infection prevention have been emphasized by health regulatory bodies [1]. Though there are reports of sensor detecting bacteria, there is no commercially available sensor that offers combined bacteria and pH measurements. This project explores the detection of E. Coli (MG1655) within a microfluidic channel integrated with microwave based sensor. This integrated device offers non-invasive and contactless sensing of both pH and E. Coli in real-time.

Methods

The microfluidic chip and 25µm-thick thin films were fabricated with mechanical consistency using soft lithography technique. They were bonded together using O_2 plasma treatment creating channels inside the chip. This offers an interface between the microwave and microfluidics. The thin film and the microfluidic chip were fabricated from Polydimethylsiloxane (PDMS) with enclosed channels of 2 mm wide and 140 µm high.

This microfluidic chip was mounted on a microwave sensor as shown in Figure 1. The presence of E. Coli and the pH is detected via changes in resonant frequency responses of the microwave system using the formula:

$$X_c = \frac{1}{2\pi f C} \qquad \text{(A)}$$

where X_c is the electrical reactance, f is the resonant frequency and C is the capacitance.

The E. Coli samples of different pH and metabolites concentration were injected into the chip for testing change in pH throughout varying samples. The changes throughout these samples were compared to pH buffer solutions also run through the microwave sensor using the same setup for comparison.

Results

Characterization of the microfluidic-microwave system was performed with DI water, ethanol, and Mueller-Hinton (MH) broth. This system provided a highly stable and unique change in signal for each material immediately in tests ranging from 20 minutes to 8 hours. This implies that not only does the microwave sensor offer highly sensitive capacitive sensing, which is observed as the change in resonant frequency (A), the system showed stable long-term and short-term feedback.

Conclusions

These promising initial results offers a new paradigm for non-invasive, contactless and real-time measurement of E. Coli infection along with the change in pH of the samples over time. This also addresses safe measurements as food safety regulations increase. Microwave based testing described, will prove to be integral in providing sensitive data for bacterial detection.

References

[1] "Safe Food for Canadians Regulations - About the Canadian Food Inspection Agency – Canadian Food Inspection Agency", *Inspection.gc.ca*, 2017. [Online]. Available: http://www.inspection.gc.ca/about-the-cfia/acts-and-regulations/forward-regulatory-plan/2017-2019/sfcr/eng/1489788732771/1489788733189. [Accessed: 22- Sep- 2017].

Figures

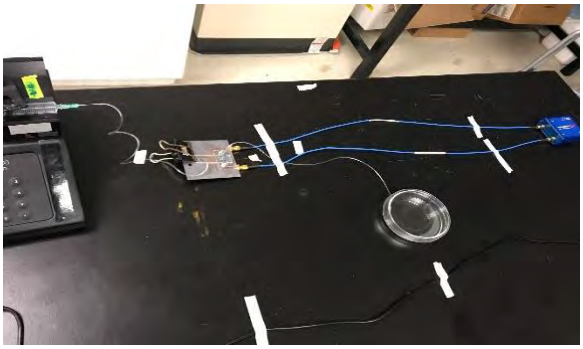

Figure 1: Experimental setup of microwave technology

Hydration Monitoring with Microwaves: A Feasibility Study

Sarah Thorson (sgthorso@ucalgary.ca), David C. Garrett, Elise C. Fear
Dept. of Electrical and Computer Engineering, Schulich School of Engineering, University of Calgary, Canada

Introduction

Monitoring and managing hydration is of interest in populations such as athletes and older adults. However, current methods of hydration assessment are invasive or unreliable [1]. We are developing a new approach to monitoring hydration using microwaves. Since the electromagnetic properties of tissue depend on water and ionic content [2], we hypothesize that microwave measurements at extremities such as the forearm are sensitive to hydration status. We previously performed a feasibility study assessing wrestlers before and after exercise[†]. However, our system suffered from non-repeatable sensor positioning which may have dominated changes due to hydration. This study aims to evaluate improvements that have been made to the system to provide repeatable positioning of the subject's arm.

Methods

The microwave measurement system consists of two antennas which are mounted such that they can be placed in contact with either side of the forearm. Reflected and transmitted microwave signals for each antenna are collected using a vector network analyzer. To improve repeatability, we mounted the antennas on a sliding track to control X and Y positioning, added a handle for the subject to grip during measurement, and added a set of wooden wedges to position the elbow in alignment with the wrist (Figure 1).

There is natural variation in the signals between different volunteers due to differences in tissue composition and arm size. However, we expect that successive measurements in the same volunteer would be similar, with differences relating to hydration status. To assess the system's ability to collect signals with repeatable positioning of the arm, we performed six measurements per day on three volunteers over two days on the same arm[‡].

[†] Approved by CHREB (ID: REB16-1283)
[‡] Approved by CHREB (ID: REB17-0245)

Results

As a measure of signal similarity, we calculated the correlation coefficient (R) for each volunteer's signals. Without improvements in the system, R_{avg} of reflected signals for a volunteer is only 0.8215. With our improved system, this results in R_{avg} of 0.9727 and 0.9992 for the reflected and transmitted signals, respectively. This informs us of the expected variation due to repositioning given little changes between successive measurements, such that we can better isolate changes due to hydration.

Conclusions

We observed a considerable improvement in the repeatability of both the reflected and transmitted signals compared with the signals collected in an earlier study. Measurements can now be more confidently compared at the same location on different days or before and after hydration changes. With this improved system, we are now performing another study with wrestlers to assess the feasibility of hydration monitoring with microwaves.

References

[1] Armstrong, *Journ. Am. Coll. Nutr.*, **26**:575S-584S, 2007.
[2] Gabriel et al. *Phys. Med. Biol.* **41:**2251-69, 1996.

Figures

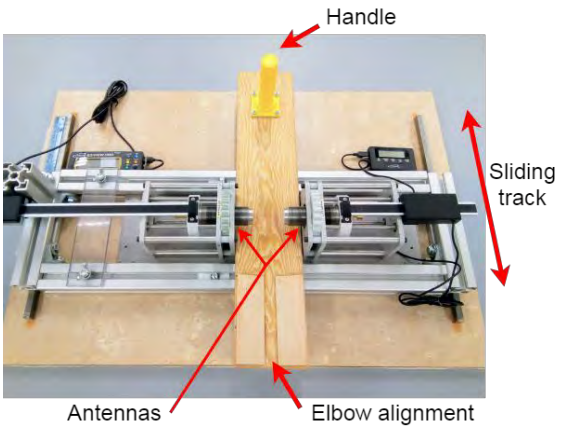

Figure 1. Microwave measurement system with modifications for improved repeatability

Evaluating Strategies of Extracting Prior Information from Acoustic Signals for Microwave based Breast Imaging Techniques

Muhammad Omer [(1)*], Pedram Mojabi [(2)], Douglas Kurrant [(1)], Joe LoVetri [(2)] and Elise Fear [(1)]
(1) Dept. of Electrical and Computer Eng., Schulich School of Eng., University of Calgary, Calgary, CA
(2) Electrical and Computer Engineering, Faculty of Engineering, University of Manitoba, Winnipeg, CA

Introduction

Microwave imaging has been proposed for monitoring breast health, however improvements in image quality are needed for clinical application. The integration of prior structural information has benefited microwave-based breast imaging techniques, including microwave tomography and microwave radar based approaches [1, 2]. These benefits include improvements in imaging resolution and localization accuracy for microwave radar, as well as enhanced accuracy of estimated tissue properties for tomography-based techniques. In addition, the structural prior also provides contextual information for the detected target, which can greatly assist in the interpretation of the imaging results. The sources of this structural prior explored in the literature include alternate imaging modalities such as Computed Tomography (CT) or Magnetic Resonance Imaging (MRI) [1]. However, we have explored the possibility of extracting prior information from acoustic signals due to the high resolution and ease of integration into the existing microwave imaging prototype systems [3].

In this paper, we aim to explore different strategies of obtaining prior information from acoustic signals, specifically using various combinations of reflected and transmitted signals. These approaches are evaluated using metrics defined for image resolution and accuracy of structural information.

Methods

The prior structural information will be extracted from scattered signals obtained by exciting realistic breast models with acoustic signals. These signals will be used to form an acoustic image using a delay-and-sum (DAS) method [2]. We consider different numbers of transmit/receive antennas, reconstructing images from reflection and transmission signals and quantifying quality of image reconstruction for each case. This will be followed by determining a weighting scheme that makes use of both reflected and transmitted signals such that high quality and accurate prior structural information is extracted from the acoustic signals. Based on this analysis, we identify effective strategies for combining acoustic signals to form prior structural information that is then integrated into the microwave-based imaging techniques.

Results

Our preliminary simulations involve exciting a 2D breast model with 64 acoustic transducers. We used 31 receivers for each transmitted signal to form a DAS image. From this configuration, we obtained good resolution and accuracy of breast regions. We then vary the number of transmit/receive pairs and quantifying the improvements in the reconstructed images.

Conclusions

In this paper, we explore the extraction structural information of the breast from acoustic signals, as this prior information improves microwave imaging techniques. Our preliminary results suggest that we can extract high quality prior information from acoustic signals. However, we aim to develop a framework of evaluating various combination strategies to identify effective configurations prior to implementation of experimental systems.

References

1. A. H. Golnabi, P.M. Meaney and K.D. Paulsen, “3D microwave tomography of the breast using prior anatomical information,” Medical Physics, 43, 2016, pp. 1933–1944.
2. B.R. Lavoie, M. Okoniewski and E.C. Fear, “Estimating the Effective Permittivity for Reconstructing Accurate Microwave-Radar Images,” PLoS ONE 11(9): e0160849. 2016.
3. M. Omer, P. Mojabi, D. Kurrant, A. Baran, J. LoVetri, and E. Fear, "Strategies for integrating ultrasound and microwave data for improved breast imaging", Int. Union of Radio Science, Aug. 2017.

Synthesis of Silicate-based Magnetic Nanoparticles for the Removal of Pharmaceutically Active Compounds from Water

Maysam Alnajjar, Nashaat N. Nassar*, Gerardo Vitale

Department of Chemical and Petroleum Engineering, University of Calgary, Calgary, AB T2N 1N4 Canada

*Corresponding Author: nassar@ucalgary.ca

Introduction

As most effluent streams come with diverse synthetic and natural chemicals, it comes as no surprise that chemical pollution of natural water resources has led to a variety of environmental and health aggravations [1]. Among these aggravations, for instance, the exposure to organic pollutants in natural waters. Pharmaceutically active compounds (PhACs) are considered as the most concentrated and frequently observed micropollutants among those organic pollutants [2]. One of the most critical compounds studied in this research is Penicillin. Although this group of antibiotics is widely used, it has been reported to cause allergies in 10% of the population of the USA [3], giving this research the greatest value of providing allergenic people with safe drinking water. Magnetic silicate-based core-shell structured nanoparticles are synthesized in-house for the competitive adsorption of different types of PhACs in water effluents. Different types of analgesic pharmaceuticals including Paracetamol and Ibuprofen will be used besides Penicillin as model drugs to test the selectivity and competitivity of the adsorption.

Methods

First, the nanoparticles are synthesized from a magnetic material coated with another silicate-based material. The nanoparticles are then applied into synthetic water sample to study the adsorption. A magnetic field is then applied after the adsorption to recover the nanoparticles. The adsorption kinetics and isotherms are depicted by applying the external mass transfer diffusion and the Sips models, respectively.

Results

The nanoparticles were prepared and analyzed using XRD and SEM analysis as shown in Figs. 1a-b. The synthesized nanoparticles have shown the ability to adsorb PhACs.

Conclusions

Silicate-based magnetic nanoparticles were synthesized as confirmed by the XRD and SEM analysis. Adsorption studies for different PhACs have shown the ability of the nanoparticles to adsorb them successfully.

References

[1] R.P. Schwarzenbach, T. Egli, T.B. Hofstetter, U. von Gunten, B. Wehrli, Global Water Pollution and Human Health, Annu. Rev. Environ. Resour. 35 (2010) 109–136. doi:10.1146/annurev-environ-100809-125342.

[2] a L.M. T. Thiebault, M. Boussafir, L. Le Forestier,a C. Le Milbeau, and R. Gu´egana, Competitive adsorption of a pool of pharmaceuticals onto a raw clay mineral†, RSC Adv. 6 (2016) 65257–65265.

[3] R. Solensky, Related editorial Penicillin allergy as a public health measure, J. Allergy Clin. Immunol. 133 (2017) 797–798. doi:10.1016/j.jaci.2013.10.032.

Figures

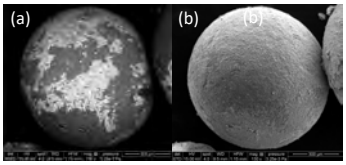

Fig. 1. SEM images for (a) optimized silicate-based magnetic core-shell structure, (b) growth of the shell on the surface of the core beyond optimum conditions.

Process Development for the Expansion of Equine Cord Blood Derived Mesenchymal Stem Cells in Bioreactors

Erin L. Roberts[1,3], Tylor Walsh[1,3], Thomas G. Koch[4], Michael S. Kallos[1,2,3]
[1]Pharmaceutical Production Research Facility, [2]Department of Chemical and Petroleum Engineering, [3]Biomedical Engineering Graduate Program, University of Calgary, 2500 University Dr. NW, Calgary, AB, T2N 1N4
[4]Department of Biomedical Sciences, Ontario Veterinary College, University of Guelph, Gordon St., Guelph, ON

Introduction

Musculoskeletal injuries are the leading cause of lameness in horses. Conventional treatments are often palliative in nature and associated with short-term efficacy only. Mesenchymal stem cells (MSCs) have shown to be a promising treatment alternative due to their proliferation potential, ability to differentiate towards a chondrogenic lineage, and immune-modulating properties[1]. *In vitro* MSC expansion is limited by current static monolayer culturing system. Expansion of equine cord-blood derived MSCs (eCB-MSCs), in stirred suspension bioreactors using microcarriers has the potential to generate a large number of cells under highly controlled conditions while decreasing space, labour and monetary requirements. The objective of this study was to investigate the effect of microcarrier density and agitation rate on the expansion of eCB-MSC.

Methods

Two factors were investigated for their effect on eCB-MSC expansion in bioreactors, 1) Cell to microcarrier (MC) ratio, and 2) Agitation rate. The experiments were carried out in 100mL bioreactors at 5% CO_2 using eCB-MSC expansion medium. Counts were performed daily using nuclei release method.

1) eCB-MSCs and microcarriers were inoculated into 100mL bioreactors at three different ratios, 2 cells/MC, 4 cells/MC, and 8 cells/MC. The bioreactors were run at 40rpm.

2) eCB-MSCs and microcarriers were inoculated into 100mL bioreactors at 4 cells/MC. The bioreactors were run at 40rpm, 60rpm and 80rpm.

Results

1)The bioreactors inoculated at 2 cells/MC achieved the greatest fold increase of 20, with a doubling time of 0.97d, while the attached cell density was greatest in the 8 cells/MC bioreactor, reaching 63,000 cells/cm^2, and had a doubling time of 1.10d (Fig1).

2) Both the 40rpm and 60rpm bioreactors achieved similar maximum cell densities close to 60,000 cells/cm^2. The 80rpm bioreactor achieved a significantly lower maximum attached cell density of 47,000 cells/cm^2 (Fig2). The doubling time for all three agitation rates was 1.1d.

Conclusions

These studies lay the groundwork for the development of a bioprocess for eCB-MCS expansion in bioreactor. Inoculation density and agitation rate had a strong effect on final cell numbers and can be used to generate large numbers of cells.

Figures

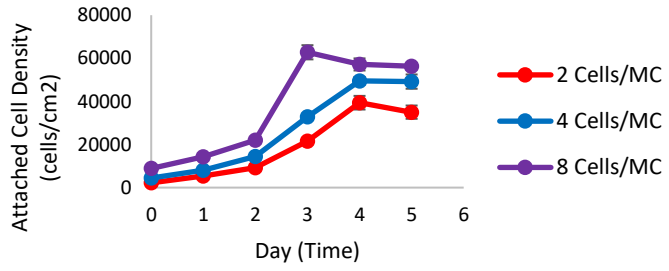

Figure 1: Attached cell density over 5 days of bioreactors inoculated at 2, 4 and 8 cells/MC.

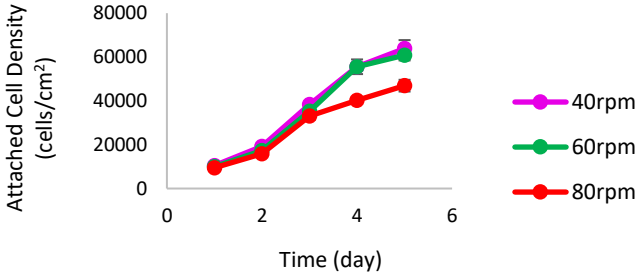

Figure 2: Attached cell density over 5 days of bioreactors run at 40, 60, 80rpm.

References

1. Carrade, D. D., et al. (2012). *Cell Med.* 4(1):1-11.

Rapid Semi-Automatic Semantic Segmentation of Full Femur and Pelvis in Computed Tomography

Bryce A. Besler, Andrew S. Michalski, Nils D. Forkert, Steven K. Boyd
University of Calgary, Calgary, Alberta

Introduction

Osteoporosis is an asymptomatic disease, often discovered after a fracture occurs. The clinical standard for diagnosing osteoporosis is dual energy x-ray absorptiometry (DXA). DXA scans are requisitioned based on osteoporosis risk factors such as sex, age, and medical history. However, thousands of computed tomography (CT) scans, containing bone density and shape information, occur every day. Opportunistic screening aims to repurpose routine CT scans to generate subject specific finite element models as a complementary tool to DXA.

The International Society of Clinical Densitometry has stated that the creation of a normative dataset of finite element derived failure load is a crucial step towards opportunistic screening [1]. A major problem in finite element model generation is the segmentation of pathological femurs and pelvises from CT datasets. We hypothesize that a user can accurately and rapidly segment pathological femur and pelvis data from CT using advanced image processing.

Methods

Ten fresh frozen cadaveric specimen were obtained through the Body Donation Program at the Gross Anatomy Laboratory in the University of Calgary. Cadavers ranged in age from 69 to 98. Bilateral hip CT scans were performed for each specimen using a GE Revolution CT scanner (GE Healthcare). The imaging volume started above the iliac crest of the pelvis and terminated in the proximal tibia. Reconstructed CT data contained 279 million voxels on average with an in-plane spacing of 0.684 mm and a slice thickness of 0.625 mm.

A two-stage algorithm was developed to segment the left and right pelvis and left and right femur in all 10 cadaveric data. First, an image enhancement is performed to increase the contrast between the cortical bone and neighboring soft tissue. The filter is a modification of the seminal multiscale vessel enhancement filter [2]. Second, a user manually identifies bone voxels in the axial, coronal, and sagittal slice for each bone of interest. The enhanced image and user labels are integrated with the graph cut framework to produce a segmentation [3]. Segmentations are cleaned using component labelling.

Results

Figure 1 shows an axial slice of the CT data before and after enhancement. Figure 2 shows a rending of the segmentation for one subject. For one subject, the semi-automatic segmentations were manually corrected to generate a ground truth. The worst-case Dice Similarity Coefficient was 0.995 (right pelvis). Segmentation of all 10 datasets was performed in one day. Previously, manual segmentation of one dataset took two days.

Conclusions

An accurate and fast method of semi-automatically segmenting clinical computed tomography was described. This technique will enable reproducible, accurate, and fast analysis of thousands of femurs needed to generate a normative dataset of failure load for opportunistic screening of osteoporosis.

References

[1] Engelke *et al.* J Clin Densitom (2015)
[2] Frangi *et al.* MICCAI (1998)
[3] Boykov and Funka-Lea. IJCV (2006)

Figures

Figure 1 (Left) – CT data (top), enhanced (bottom)
Figure 2 (Right) – Segmentation rendering

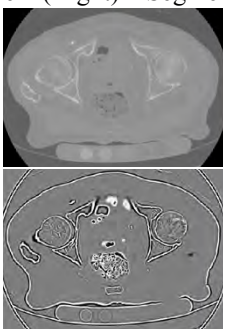

A Method to Measure 3D Micro-scale Deformation of Biological Tissue

Scott Sibole, Eng Kuan Moo, Walter Herzog
University of Calgary, Biomedical Engineering Graduate Program, Calgary Alberta.

Introduction

Illuminating the mechanical environment of cells residing in biological tissues is of critical importance to understanding health. This is due the strong regulatory role of mechanics in cellular physiology – a phenomenon referred to as mechanotransduction. The cellular maintenance of, in particular load-bearing tissues, is tightly coupled to mechanotransduction.[1] Empirical measurement of the mechanics that occur at the cellular scale in living tissue however, represents a substantial technological challenge. Fortunately, recent advancement in multiphoton laser microscopy allows for photobleaching of a high resolution grid onto tissue in 3D, which in turn can be used to measure 3D strain across the grid domain. This work demonstrates the feasibility of such a technique and presents a newly developed deformable image registration software framework for analysis of data acquired from experiments in articular cartilage.

Methods

Articular cartilage explants from porcine specimens were mounted in a custom light-transmissible indentation testing system in series with a laser scanning microscope.[2] A 3D grid was then photobleached onto the tissue with $20 \times 20 \times 11$ grid lines in x, y, and z directions, respectively, spaced every $10\mu m$. The indentation system was then used to apply 10, 20, and 30% tissue thickness strains. 3D images of the sample were acquired in the undeformed and deformed configurations.

A software framework was developed to analyze the experimental images. In brief terms, this framework allows for easy application of image registration optimization routines capable of finding the optimal mapping between images in different configurations. Upon the determination of this mapping, any kinematic field variable can be calculated in the domain of the grid. The software automatically returns the Green-Lagrange (GL), principal GL, maximum GL shear, and volumetric strains.

Results

The experimental procedure proved to be both robust and feasible. Likewise, the subsequent analysis of the 3D images demonstrated that the developed software allowed for high fidelity tracking of the grid. The rich datasets returned by the analysis can be qualitatively investigated with advanced 3D visualization (Figure 1) or quantitatively with additional numerical and/or statistical analyses. Such data can, likewise, inform future studies.

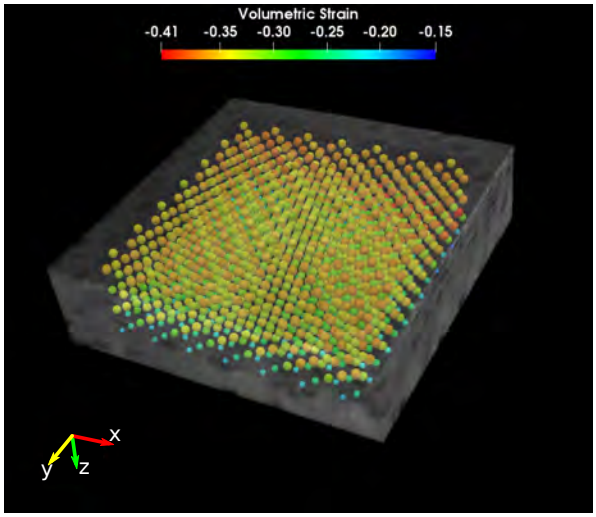

Figure 1: The volumetric strain calculated at grid points and overlaid on the 3D image of the cartilage under 30% compressive strain.

Conclusion

This work represents a major step in empirical measurement of the cellular mechanical environment in intact living biological tissue that results from loading at higher spatial scales *e.g.* the tissue surface. The method's scope of application is broad including direction or validation of modelling studies, mechanobiological investigations, and characterization of tissue engineered constructs. The software will be made open source under a BSD license with hopes that it will enable researchers of minimal technical background to use this technique in their investigations.

References

1. (2014) Humphrey J, Nat Rev Mol Cell Bio.
2. (2012) Han SK, J Biomech.

Reproducibility of a Region-based Method to Assess Knee Joint Mechanics and Meniscus and Cartilage Health under Load in ACL-injured Individuals

Ibukunoluwa O Elebute, Emily J McWalter
Department of Mechanical Engineering, University of Saskatchewan, Saskatoon, SK, Canada

Introduction

Individuals who have experienced anterior cruciate ligament (ACL) injury are disproportionately affected by osteoarthritis, with approximately 50% developing the disease 10-20 years after injury[1]. ACL-injury affects both tissue health[2] and joint mechanics[3]. Quantitative magnetic resonance imaging (qMRI) and gait analysis can be used to study these quantities *in vivo; h*owever, the relationship between them is not clear in ACL-injured individuals. We aim to develop a method to reproducibly assess tissue health and joint mechanics *in vivo* in the loaded knee.

Methods

Loading Rig Design/Construction: An MRI-safe loading rig will be built to simulate 30% body weight in the knee joint. Participants, in a supine position within the scanner, will press on a pedal, thereby applying the load. The applied load will be controlled using a series of bungee cords of known stiffness.

qMRI Acquisition and Processing: Images of five ACL-injured individuals and five healthy volunteers will be acquired on a 3T MRI scanner (Magnetom Skyra, Siemens, Erlangen, Germany). The imaging protocol includes sequences for T_2 and $T_{1\rho}$ relaxation time mapping of articular cartilage and meniscus. All scans will be carried out under unloaded and loaded conditions. A cluster analysis method, developed previously by our group[3], will be used to identify focal changes in the qMRI data with load.

Biomechanics: Additional MR images will be acquired to assess three-dimensional pose and contact area under loading at discrete angles of knee flexion[4]. We have termed this parameter 'mechMR'. Standard three-dimensional kinematic and kinetic gait analysis will be carried out using a motion capture system (Vicon Nexus, Vicon Motion Systems, Oxford, UK).

Data Integration and Analysis: Data integration will be facilitated with custom-made MRI-lucent gait markers in order to directly compare qMRI, mechMR and gait data in a common anatomically-based coordinate system. The markers must be suitable for gait analysis and provide a signal intensity in the range of articular cartilage on MRI so as not to disrupt the dynamic range of the images. Data superposition and spatial correlograms will be used to identify regional relationships between parameters.

Reproducibility Analysis: The data collection protocol will be repeated on three consecutive days. Root mean-square percent coefficient of variation (RMSCV %) will be used to assess reproducibility. Effect size will also be determined.

Results

To date, the MRI-safe loading rig has been designed (see Figure 1 below) and the MRI-lucent gait markers are under development. Work is ongoing for this project.

Anticipated Conclusions

Upon completion of this project, we will have developed a repeatable protocol that can be used to identify regional relationships between tissue health and joint mechanics in the ACL-injured population.

References

1) Lohmander et al, Am J Sports Med, 2007; 2) Tiderius et al, Arth & Rheum, 2005 3) Ismail et al, Clin Biomech, 2016; 4) Monu et al, OA&C, 2017; 4) McWalter et al, JMRI, 2014

Figures

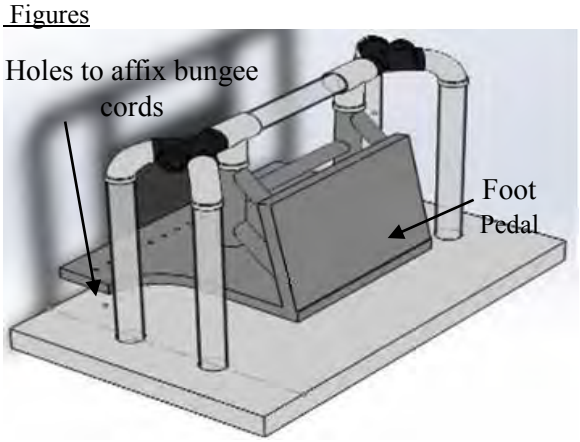

Figure 1: MRI-safe loading rig.

Addressing challenges in Measuring Stresses on Knee Cartilage using Fiber-optic Sensors

Paris Vakiel[1, 2], Christopher R. Dennison[3], Nigel G. Shrive[1,2]
[1]University of Calgary, Calgary, AB, [2] McCaig Institute for Bone and Joint Health, Calgary AB,
[3]University of Alberta, Edmonton AB

Introduction

Knowledge of in-vivo stresses in the knee joint and how they change after an injury is of great value to clinicians, researchers and prosthetic designers. Understanding these stresses is vital to understanding the etiology and progression of degenerative joint diseases such as osteoarthritis, as well as understanding the effects of clinical interventions that are meant to slow or halt the progression of these ailments. Currently, the most widely used method for measuring contact stresses are stress-sensitive films. These methods have substantial limitations. Insertion of the films into the joint alters the natural joint mechanics and lubrication. It also requires a significant amount of dissection and removal of biomechanically relevant structures thus altering factors such as synovial fluid pressurization and lubrication. Moreover there are significant errors associated with the thickness and curvature of these films. Fiber optic sensors have the potential to address many of the limitations associated with stress sensitive films. Their small size (diameter of 125 μm and sensing length of 1 mm) allows them to be inserted into the joint space without the removal of biomechanically relevant structures. They are mechanically compliant and biocompatible allowing for much more accurate stress measurements. While these sensors address many of the limitations associated with stress sensitive films there are some challenges associated with their use. In this study we aim to address these challenges.

Methods

Although their modulus dependency is lower compared to stress sensitive films, it is still an important consideration in obtaining reliable stress readings. In an effort to optimize calibration and minimize the potential for error arising from the modulus dependency of the sensors; ovine knee cartilage was used as a contact material during the calibration process. Fresh ovine knees were obtained and dissected. The joint capsule was opened and the patella removed. The joint was then opened up allowing access to the medial and lateral femoral condyles. A 4mm diameter biopsy punch was then used to extract circular cartilage discs from the femoral head. During this process, the cartilage was continuously hydrated using PBS. The small size of the disc made for near uniform thickness. A small needle was then used to make a small hole through the disc, perpendicular to the cartilage disc column. A fiber was threaded through the hole such that the sensor sat within the cartilage disc. The disc was then placed in a loading machine. Two PBS soaked lab wipes were place above and below the disc to keep it hydrated. The disc was loaded to 70 N in 10 N increments and the readings from the sensors were recorded.

Results

Linear calibration curves with an R^2 value of more than 0.99 demonstrate the linear relationship between the changes in the readings and the changes in stress levels as well as the effectiveness of the presented calibration curve.

Conclusion

In this study, one of the main challenges in working with the FBG sensors for biomedical purposes namely calibration was addressed. The design of an effective and repeatable calibration methodology using articular cartilage has paved the way to perform reliable stress measurement within the knee with minimal disruption to normal load bearing and lubrication, filling a knowledge gap that currently exists regarding the biomechanical changes contributing to osteoarthritis initiation and progression

References

Dennison, C. R., Wild, P. M., Wilson, D. R., and Gilbart, M. K., 2010, "An in-fiber Bragg grating sensor for contact force and stress measurements in articular joints," Measurement Science and Technology, 21, p. 115803.

Huberti H H and Hayes W C 1988 Contact pressure in chondromalacia patellae and the effects of capsular reconstructive procedures J. Orthop. Res. 6 499–508

Komistek R D, Kane T R, Mahfouz M, Ochoa J A and Dennis D A 2005 Knee mechanics: a review of past and present techniques to determine in vivo loads J. Biomech.38 215–28.

Efficacy of CTA in Diagnosing Non-Traumatic Non-Variceal Gastrointestinal Bleeding Prior to Transarterial Embolization after Endoscopic Failure in Managing Acute Gastrointestinal Bleeding

Scott Brunet[1], Aman Wadhwani[1], Cody Pollock[1], Vamshi Kotha[1,2], Eric Herget[1,2],Paul Beck[3]

[1] Department of Radiology, University of Calgary, Foothills Medical Centre, Calgary, AB; [2]Division of Interventional Radiology, University of Calgary, Foothills Medical Centre, Calgary, AB;
[3] Division of Gastroenterology, Department of Medicine University of Calgary, Foothills Medical Centre, Calgary, AB

Introduction:

Non-variceal gastrointestinal bleeding (NVGIB) is associated with a high mortality and morbidity. 10-30% of these patients tend to fail endoscopy and receive transarterial embolization (TAE) as an alternative. Studies suggest that performing pre-angiography computed tomography angiography (CTA) increases the positive yield of visceral angiography. Our objective was to determine (1) the accuracy of CTA in diagnosing NVGIB following failed endoscopy and (2) the impact of CTA pre-TAE on the angiographic technique.

Methods:

Data was collected from 69 consecutive patients who presented to the emergency department with acute NVGIB and received TAE after endoscopy failed to manage their NVGIB. Of these 69 patients, 30 underwent pre-angiography CTA. These CTA examinations were retrospectively reviewed by 2 radiology residents and 2 staff radiologists. These findings were compared to angiography, or/and surgery. Inter-reader reliability was evaluated with kappa coefficient (κ).

Results:

Sensitivity, specificity, positive predictive value (PPV), negative predictive value (NPV), and accuracy of CTA in diagnosing active NVGIB was 63%, 100%, 100%, 23%, and 93%, respectively. CTA was able to accurately diagnose the cause and source of NVGIB in 85% of the patients respectively. The inter-reader reliability coefficient for identifying the cause and source of NVGIB was κ=0.72. In 20 cases, in whom CTA localized NVGIB, no diagnostic catheter angiogram was required. When comparing patients that received CTA prior to their therapeutic embolization for NVGIB to the patients that did not receive a pre-embolization CTA, there was an overall reduction of 19 minutes of procedural time.

Conclusions:

CTA is an accurate diagnostic modality in detecting NVGIB. Performing abdomen and pelvis CTA before TAE improves the localization of gastrointestinal bleeding and facilitates embolization by reducing the overall procedural time. Impact of pre-angiography CTA on reducing the overall number of imaging studies, amount of contrast administered, and overall mortality and morbidity needs to be further investigated.

References:

1.D.J. Bjorkman, et al. Urgent vs. elective endoscopy for acute non-variceal upper-GI bleeding: An effectiveness study, Gastrointest. Endosc. 60 (2004) 1–8.
2.L.E. Targownik, A. Nabalamba, Trends in management and outcomes of acute nonvariceal upper gastrointestinal bleeding: 1993-2003., Clin. Gastroenterol. Hepatol. 4 (2006) 1459–1466.
3.C.J. Laing, et al. Acute gastrointestinal bleeding: Emerging role of multidetector CT angiography and review of current imaging techniques, Radiographics. 27 (2007) 1055–70.
4.Y. Geffroy, et al., Multidetector CT angiography in acute gastrointestinal bleeding: why, when, and how., Radiographics. 31 (2011) E35-46.